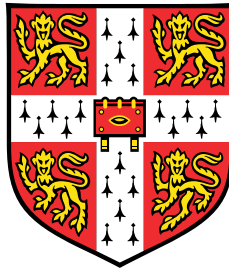


# Quantum transport in gapped graphene



**Yang Li**

Department of Materials Science & Metallurgy  
University of Cambridge

This thesis is submitted for the degree of  
*Doctor of Philosophy*

Robinson College

September 2019



## **Declaration**

I hereby declare that this thesis, submitted for the degree of Doctor of Philosophy at the University of Cambridge, is a result of my own work as a PhD candidate in the Cambridge Graphene Centre and Department of Materials Science & Metallurgy, University of Cambridge, under the supervision of Dr Jason Robinson since October 2015. This thesis includes nothing which is the outcome of work done in collaboration except as declared in the Preface and specified in the text.

It is not substantially the same as any that I have submitted, or, is being concurrently submitted for a degree or diploma or other qualification at the University of Cambridge or any other University or similar institution except as declared in the Preface and specified in the text. I further state that no substantial part of my dissertation has already been submitted, or, is being concurrently submitted for any such degree, diploma or other qualification at the University of Cambridge or any other University or similar institution except as declared in the Preface and specified in the text.

This thesis does not exceed 60,000 words including abstract, tables, footnotes and appendices.

Yang Li  
September 2019



## Abstract

This thesis focuses on investigating local and nonlocal transport properties in hexagonal boron nitride (hBN)/graphene superlattice Hall bars and graphene Hall bars proximity-coupled to the ferrimagnetic insulator yttrium iron garnet ( $\text{Y}_3\text{Fe}_5\text{O}_{12}$  or YIG).

The first part describes in detail the pulse laser deposition of atomically flat YIG thin films onto single crystal gadolinium gallium garnet with a magnetization of  $144 \text{ emu cm}^{-3}$ . This part also outlines device fabrication procedures including graphene exfoliation and dry transfer, electron beam lithography and metallization of side-contacts, and finally the electrical setup for measuring local and nonlocal transport in graphene.

The second part investigates transport properties in hBN/graphene/hBN superlattice Hall bars with a field-effect mobility of up to  $220,000 \text{ cm}^2 \text{ V}^{-1} \text{ s}^{-1}$  at 9 K with low charge impurities. By aligning hBN and graphene, a  $\sim 33.7 \text{ meV}$  band gap at 9 K is demonstrated at the primary Dirac point in zero magnetic field. Furthermore, the nonlocal resistances approach  $h/2e^2$ , where  $h$  is Planck's constant and  $e$  is the electron charge. Nonlocal measurements demonstrate that, below 60 K a spin-degenerate ballistic counter-propagating edge state forms and dominates with a possible secondary contribution from a network of one-dimensional conducting channels with soliton-like domain walls. The spin-degenerate ballistic edge states offer possibilities for electronic applications beyond quantum spin and anomalous Hall effects since a quantized resistance is observed through valley coupling.

The third part reports a proximity-induced magnetic exchange field in graphene of the order 60 T by placing graphene on the ferrimagnetic insulator YIG. From electrical transport measurements, the magnetic order and energy gap of the edge modes in graphene are tunable, and a transition between the canted antiferromagnetic and spin-polarized ferromagnetic  $\nu = 0$  quantum Hall states can be achieved with relatively low magnetic fields ( $> 6 \text{ T}$ ) at 2.7 K.

The fourth part summarizes the key results of the thesis.



*To my family and friends for supporting and encouraging me with affections and love.*



## Acknowledgements

First and foremost I would like to thank my supervisor Dr Jason Robinson for the opportunity of being part of the his research group as a PhD student. Jason has been an invaluable guide and support me through stimulating questions and constructive criticism.

I would like to acknowledge my advisor Dr Mario Amado for his valuable advice and support during the entire period of my PhD research. Mario is also one of the important collaborators for providing high quality magnetic samples and helping me design the low-temperature transport measurement systems.

I am very grateful to all the collaborators I had the honor and privilege to work with, and who significantly contributed to the results presented here. In particular, I am thankful for Dr Timo Hyart, who designed the theoretical calculation models of transmission probabilities in edge state transport presented in Chapter 9 and magnetic exchange field induced by magnetic substrate presented in Chapter 10. I am indebted with Dr Grzegorz Mazur for the useful discussions about low-temperature transport measurement setup. I would like to thank Mr Thomas Wagner, who helped me perform the 2.7 K low-temperature transport measurement in Hitachi Lab presented in Chapter 10.

I would like to acknowledge all the colleagues that I have worked with in the Cambridge Graphene Centre. In particular, I am grateful to Dr Antonio Lombardo and Dr Jingbo Wu, who taught me a lot of experimental techniques at the beginning of research. I would like to thank all the technicians who helped me solve the equipment issues.

I acknowledge funding from Cambridge Trust and China Scholarship Committee to support me for the PhD study.

I would like to acknowledge all the wonderful friends in the college and department. We shared the research experience and exchanged ideas between different fields. They helped me overcome the most difficult time during the PhD.

Finally I would like to thank my family for their continuous support and motivation. They gave me the important lessons in my life and cheered me up whenever I felt down.



# Table of contents

<b>List of acronyms</b>	<b>xv</b>
<b>1 Introduction</b>	<b>1</b>
1.1 Motivation . . . . .	1
1.2 Thesis outline . . . . .	3
<b>2 Two-dimensional materials</b>	<b>5</b>
2.1 Graphene . . . . .	5
2.1.1 Crystal and band structures . . . . .	5
2.1.2 Electrical properties . . . . .	7
2.1.3 Raman spectroscopy . . . . .	8
2.2 Hexagonal boron nitride . . . . .	11
2.3 Summary . . . . .	12
<b>3 Localized magnetism</b>	<b>13</b>
3.1 Magnetism in magnetic insulators . . . . .	13
3.2 Magnetocrystalline anisotropy . . . . .	14
3.3 Magnetic hysteresis . . . . .	14
3.4 Magnetic properties of materials . . . . .	15
3.4.1 Diamagnetism . . . . .	16
3.4.2 Paramagnetism . . . . .	16
3.4.3 Ferrimagnetism . . . . .	16
3.5 Yttrium iron garnet . . . . .	17
3.6 Summary . . . . .	19
<b>4 Hybrid two-dimensional materials</b>	<b>21</b>
4.1 Increased mobility in graphene . . . . .	21
4.2 Band gap opening in graphene . . . . .	22
4.3 Magnetic proximity effect in graphene . . . . .	24

4.4	Summary . . . . .	26
<b>5</b>	<b>Quantum effects in graphene</b>	<b>27</b>
5.1	Landau level . . . . .	27
5.2	Quantum Hall effect . . . . .	29
5.3	Quantum spin Hall effect . . . . .	31
5.4	$\nu = 0$ state . . . . .	32
5.5	Quantum anomalous Hall effect . . . . .	33
5.6	Summary . . . . .	35
<b>6</b>	<b>Experimental methods for device fabrication and measurements</b>	<b>37</b>
6.1	Raman spectroscopy . . . . .	37
6.2	Atomic force microscopy . . . . .	39
6.3	Thin flake preparation . . . . .	40
6.4	Thin flake transfer technique . . . . .	41
6.4.1	Transfer procedures for hBN/graphene/hBN device . . . . .	41
6.4.2	Transfer procedures for graphene/YIG device . . . . .	42
6.5	Graphene-based Hall bar fabrication . . . . .	46
6.5.1	Charging effects on insulating substrate . . . . .	46
6.5.2	Hall bar etching . . . . .	47
6.5.3	Side-contact deposition . . . . .	47
6.5.4	Top-gate dielectric layer and contacts fabrication . . . . .	47
6.6	Measurement setup . . . . .	48
6.7	Summary . . . . .	49
<b>7</b>	<b>Fabrication of thin film YIG on GGG</b>	<b>51</b>
7.1	Substrate selection and preparation . . . . .	51
7.2	Pulsed laser deposition . . . . .	52
7.3	X-ray diffraction . . . . .	53
7.4	Vibrating sample magnetometer . . . . .	55
7.5	Structural characterization of YIG on GGG . . . . .	55
7.6	Magnetic properties . . . . .	56
7.7	Summary . . . . .	59
<b>8</b>	<b>Nonlocal transport in graphene</b>	<b>61</b>
8.1	Spin Hall and Zeeman spin Hall effects . . . . .	61
8.2	Valley Hall effect . . . . .	62

8.3	Edge state transport . . . . .	63
8.4	Ohmic contribution . . . . .	65
8.5	Thermal contribution . . . . .	65
8.6	Summary . . . . .	68
<b>9</b>	<b>Zeroth Landau level in graphene/hBN superlattice</b>	<b>71</b>
9.1	Introduction . . . . .	71
9.2	Device fabrication . . . . .	72
9.3	Device characterization . . . . .	74
9.3.1	Raman spectroscopy . . . . .	74
9.3.2	Field-effect mobility . . . . .	74
9.3.3	Secondary Dirac point . . . . .	76
9.3.4	Mean free path . . . . .	77
9.4	Local transport measurements . . . . .	78
9.4.1	$\nu = 0$ state in hBN/graphene/hBN . . . . .	78
9.4.2	Variable range hopping . . . . .	80
9.4.3	Quantum Hall effect evolution . . . . .	81
9.5	Nonlocal transport measurements . . . . .	81
9.5.1	Nonlocal transport in zero magnetic field . . . . .	81
9.5.2	Nonlocal transport under magnetic field . . . . .	83
9.5.3	Extrinsic origins of nonlocal resistance . . . . .	83
9.5.4	Intrinsic origins of nonlocal resistance . . . . .	84
9.6	Summary and future work . . . . .	88
<b>10</b>	<b>Zeroth Landau level in magnetic graphene</b>	<b>91</b>
10.1	Introduction . . . . .	91
10.2	Device fabrication . . . . .	94
10.3	Device characterization . . . . .	94
10.3.1	Raman spectroscopy . . . . .	94
10.3.2	Hall-effect and field-effect mobility . . . . .	96
10.4	Transport measurement . . . . .	97
10.4.1	Local and nonlocal transport in zero magnetic field . . . . .	97
10.4.2	Local and nonlocal transport under magnetic field . . . . .	98
10.4.3	$\nu = 0$ state in hBN/graphene Hall bar on YIG . . . . .	98
10.4.4	Nonlocal transports with rotating magnetic field . . . . .	103
10.5	Energy gap of the edge modes . . . . .	106
10.6	Summary and future work . . . . .	108

<b>11 Thesis summary</b>	<b>111</b>
<b>References</b>	<b>115</b>
<b>Appendix A Calculation of the transmission probability</b>	<b>133</b>
<b>Appendix B Calculation of transition between ferromagnetic and canted antiferromagnetic states</b>	<b>137</b>

# List of acronyms

$\alpha$	Angle between applied magnetic field and the device surface
$a$	Distance between nearest neighbor carbon atoms
$\beta$	Angle between the incident X-ray beam and the crystallographic plane
$B$	Applied magnetic field (induction)
$B_{\perp}$	Out-of-plane magnetic field
$B_{\parallel}$	In-plane magnetic field
$B_Z$	Zeeman field
$C$	Curie constant
$\delta$	Lattice mismatch between hBN and graphene
$d$	Distance between two adjacent crystallographic planes
$\Delta_i$	Hartree-Fock mean field potential
$DOS$	Density of states
$e$	Electron charge
$E_a$	Band gap energy
$E_{ex}$	Exchange energy
$E_N$	Landau level
$E_Z$	Zeeman energy

---

$\hbar$	Planck's constant divided by $2\pi$
$H$	Magnetic field strength
$h$	Planck's constant
$H_c$	Coercive field strength
$H_{\text{sat}}$	Magnetic field strength for achieving saturation magnetization
$I$	Inject current
$J$	Strength of the exchange interaction
$k_B$	Boltzmann's constant
$\lambda$	Moiré wavelength
$\lambda_x$	X-ray wavelength
$L$	Channel length
$L_{\text{mfp}}$	Mean free path
$l_B$	Magnetic length
$\mu_B$	Bohr magneton
$\mu$	Mobility
$M$	Magnetization
$M_r$	Remanent magnetization
$M_s$	Saturation magnetization
$m_{\vec{r}}$	Sublattice asymmetry
$m_e$	Electron mass
$M_{ex}$	Intrinsic magnetic exchange field
$M_{\text{sub}}$	Magnetization of magnetic substrate
$\vec{M}_T$	Total magnetic field equals the sum of the Zeeman field and magnetic exchange field
$N$	Landau level quantum number

---

$n_{2D}$	Carrier density
$\nu$	Filling factor
$\omega$	Angle between the incident X-ray beam and the sample surface
$\omega_c$	Angular frequency
$Q_E$	Heat flow
$R_{nl}$	Nonlocal resistance
$R_q$	Root mean squared roughness
$R_{xx}$	Longitudinal resistance
$R_{xy}$	Hall resistance
$\rho_{xx}$	Longitudinal resistivity
$\rho_{xy}$	Hall resistivity
$\vec{S}_i$	Spin operator on site $i$
$\sigma_i$	Pauli matrices operate on the spin degree of freedom
$\sigma_{xx}$	Longitudinal conductivity
$\sigma_{xy}$	Hall conductivity
$S_{yx}$	Transverse thermopower coefficient
$\tau$	Elastic scattering time
$\theta$	Angle between the spins and magnetic field
$T$	Temperature
$t$	Nearest-neighbor hopping energy
$t'$	Next nearest-neighbor hopping energy
$T_C$	Curie temperature
$T_N$	Néel temperature
$\tau_i$	Pauli matrices operate on the valley degree of freedom

$T_r$	Transmission probability
$\mu_0$	Permeability of free space
$\mu_r$	Relative permeability
$u$	Anisotropy energy
$\varepsilon_F$	Fermi level
$\varphi$	Relative rotation angle between hBN and graphene
$v_F$	Fermi velocity
$V_{TG}$	Gate voltage
$W$	Channel width
$\chi$	Susceptibility
$Z_2$	Topological invariant
2DEG	Two-dimensional electron gas
AF	Antiferromagnetic
AFM	Atomic force microscopy
AHE	Anomalous Hall effect
ALD	Atomic layer deposition
CAF	Canted antiferromagnetic
DI	Deionized
DP	Dirac point
EBL	Electron beam lithography
F	Ferromagnetic
FWHM	Full-width at half-maximum
GGG	Gadolinium gallium garnet

---

hBN	Hexagonal boron nitride
IPA	2-propanol
LIA	Lock-in amplifier
LL	Landau level
MPE	Magnetic proximity effect
PC	Polycarbonate
PDMS	Polydimethylsiloxane
PLD	Pulsed laser deposition
PMMA	Poly(methyl methacrylate)
QAHE	Quantum anomalous Hall effect
QHE	Quantum Hall effect
QSHE	Quantum spin Hall effect
RIE	Reactive ion etcher
SDP	Secondary Dirac point
SHE	Spin Hall effect
SOC	Spin-orbit coupling
TI	Topological insulators
TMD	Transition metal dichalcogenide
VHE	Valley Hall effect
VRH	Variable range hopping
VSM	Vibrating sample magnetometer
XRD	X-ray diffraction
XRR	X-ray reflectivity
YIG	Yttrium iron garnet
ZSHE	Zeeman spin Hall effect



# Chapter 1

## Introduction

### 1.1 Motivation

The fast growth of the Internet has a revolutionary impact on culture and commerce, and brings a lot of challenges for the semiconductor industry. For over 50 years, progress in the semiconductor industry has followed Moore's Law [1] by scaling transistors to smaller dimensions and doubling the density of transistors every two years. But the pace of increase in density of transistor is slowing down due to rapidly approaching scientific limits. And the increase of dynamic power consumption of integrated circuits leads to a sacrifice of operating frequency in order to keep high density of transistors. Memory products will reach two-dimensional limits first and related companies have started to utilize the vertical dimension [2]. State-of-the-art processors use three-dimensional silicon-based metal oxide semiconductor field-effect transistors with feature length of 7 nm [3]. Digital logic transistors require fast operation (high carrier mobility), effective switching ( $10^4 - 10^7$  on/off ratios) and low power consumption during operation (low off-state conductance) [4, 5], which motivates to search for new device concepts and materials.

Two-dimensional van der Waals semiconductor materials including graphene and transition metal dichalcogenides (TMDs) have enabled new scientific and technological breakthrough across a variety of disciplines in solid-state physics and applications. In particular, two-dimensional materials are promising for transistor channel materials in large-scale integrated circuits due to easy processability and weak short channel effects that are often encountered by silicon-based transistors [4]. In particular, graphene has attracted more attentions on electronics because it is atomically thin, chemically stable at room temperature, and with exceptionally high carrier mobility of  $180,000 \text{ cm}^2 \text{ V}^{-1} \text{ s}^{-1}$  at 300 K and  $1,800,000 \text{ cm}^2 \text{ V}^{-1} \text{ s}^{-1}$  at 9 K [6]. Moreover the carrier density of graphene can be modulated by gate voltage [7]. However, the lack of a band gap in graphene means that it cannot

achieve an off-current state, limiting its use in digital logic transistors. There is a need for opening a band gap in graphene or finding new two-dimensional materials with a sizable band gap to support high on/off ratios while maintaining high carrier mobilities and scalability. Several approaches have been proposed to open a band gap in graphene, such as applying an electric field perpendicular to A/B-stacked bilayer graphene [8–10], using a graphene nanoribbon [11–13]. However, all of these haven't met the requirements for the digital logic devices.

Logic devices use binary digits for information transfer and processing, which can be represented by charge, spin and valley degrees of freedom. The use of the spin degree of freedom in electronics started in the 1980s [14] and graphene is a promising spin channel material owing to its long intrinsic spin lifetime and spin diffusion length of several micrometer [15]. The valley degree of freedom is a property of charge carriers, and it refers to the confinement of electrons or holes in distinct conduction band minimum or valence band maximum at the same energy but different positions in momentum space, leading to potential valleytronic devices [16]. Graphene valleytronics was proposed a decade ago [17, 18], but the existence of inversion symmetry makes it challenging to use the valley degree of freedom.

In recent years, van der Waals heterostructures have gained interests due to their possibility of implementing new functionalities in devices by assembling two-dimensional materials layer-by-layer on demand. It has been shown that the gapless band structure of graphene can be engineered with new properties by placing it proximity to other materials, including the formation of band gap [19–22] and magnetism [23, 24]. Graphene-based heterostructures have great potentials to be used for digital logic devices.

In summary, the key aims of this thesis are:

(1) To develop transfer methods for exfoliated graphene onto hexagonal boron nitride (hBN) and the ferrimagnetic insulator thin film yttrium iron garnet ( $Y_3Fe_5O_{12}$  or YIG) with high mobility and low defects.

(2) To develop side-contacts fabrication for graphene-based van der Waals heterostructure Hall bars.

(3) To investigate the interface couplings in hBN/graphene/hBN and hBN/graphene/YIG Hall bars by local and nonlocal transport measurements with gate voltage dependence under different magnetic fields and temperatures.

(4) To probe the electronic and magnetic properties of edge states in hBN/graphene/YIG Hall bars by transport measurement.

## 1.2 Thesis outline

This dissertation presents and discusses the electrodynamic properties of edge states in graphene-based heterostructures. The interface couplings of graphene/hBN and graphene/YIG are systematically investigated by local and nonlocal transport measurements.

**Chapter 2** reviews structural, electronic and Raman properties of graphene and hBN.

**Chapter 3** introduces the basic properties related to localized magnetism, then reviews the magnetic properties of different magnetic materials, in particular, the ferrimagnetic insulator (YIG).

**Chapter 4** reviews the interface coupling between graphene and other materials, including increased carrier mobility, band gap opening and induced magnetism.

**Chapter 5** reviews the theory and experiment results of quantum effects in graphene.

**Chapter 6** describes experiment techniques and procedures for the fabrication and transport measurement of graphene Hall bars including thin flake preparation, transfer, lithography, and metal deposition.

**Chapter 7** introduces pulsed laser deposition method for YIG, reports the structural and magnetic properties of YIG from X-ray diffraction, atomic force microscopy, and vibrating sample magnetometer measurements.

**Chapter 8** reviews the intrinsic and extrinsic origins of nonlocal resistance in graphene-based Hall bars.

**Chapter 9** reports hBN/graphene/hBN superlattice Hall bars in which nonlocal resistance approaches  $h/2e^2$  at the primary Dirac point due to spin-degenerate ballistic valley helical edge states.

**Chapter 10** reports the proximity-induced magnetic exchange field in graphene of the order 60 T by placing graphene on a ferrimagnetic insulator YIG using local and nonlocal transport measurements.

**Chapter 11** summarizes main achievements.



# Chapter 2

## Two-dimensional materials

Two-dimensional materials exist in bulk form as strongly bonded layers with weak out-of-plane interactions, allowing exfoliation into two-dimensional layer of single unit cell thickness. In 2004, graphene was first obtained through mechanical exfoliation from graphite [7] and attracts a lot of interests as it is an extremely thin electrical and thermal conductor [25], with high carrier mobility of  $180,000 \text{ cm}^2 \text{ V}^{-1} \text{ s}^{-1}$  at 300 K [6] and ambipolar field-effect gate modulation [7, 26]. Recent advances in sample preparation, optical detection, transfer and manipulation of thin layer materials have opened up new opportunities for two-dimensional van der Waals crystals in scientific research and engineering applications. Hexagonal boron nitride (hBN) is a two-dimensional insulator with a similar lattice structure to graphene and has been widely used as an encapsulation layer and an insulating substrate due to its atomic flatness, chemical inertness, absence of dangling bonds and effective dielectric screening for impurities [27].

### 2.1 Graphene

#### 2.1.1 Crystal and band structures

Graphene is made of carbon atoms in a honeycomb structure [Figure 2.1(a)]. The structure can be seen as a triangular Bravais lattice with a basis of two atoms (A and B) per unit cell. The distance ( $a$ ) between nearest neighbor carbon atoms is 0.142 nm, which is the average of the lengths of the single (C-C) and double (C=C) covalent  $\sigma$  bonds. The lattice vectors ( $\vec{a}_1$  and  $\vec{a}_2$ ) can be described in the  $(x, y)$  coordinates as,

$$\vec{a}_1 = \sqrt{3}a\vec{k}_x, \vec{a}_2 = \frac{\sqrt{3}a}{2} (\vec{k}_x + \sqrt{3}\vec{k}_y). \quad (2.1)$$

The modulus of the lattice vectors yields the lattice spacing of  $0.24 \text{ nm}$  ( $\sqrt{3}a$ ). The reciprocal lattice is defined with the base vectors ( $\vec{b}_1$  and  $\vec{b}_2$ ) corresponding to the triangular Bravais lattice [Figure 2.1(b)],

$$\vec{b}_1 = \frac{2\pi}{\sqrt{3}a} \left( \vec{k}_x - \frac{\vec{k}_y}{\sqrt{3}} \right), \vec{b}_2 = \frac{4\pi}{3a} \vec{k}_y. \quad (2.2)$$

The formation of the Brillouin zone in graphene is an intrinsic property of the Bravais lattice. There are two sets of points (K and K') at the corners of the Brillouin zone, which are named as Dirac points (DPs).

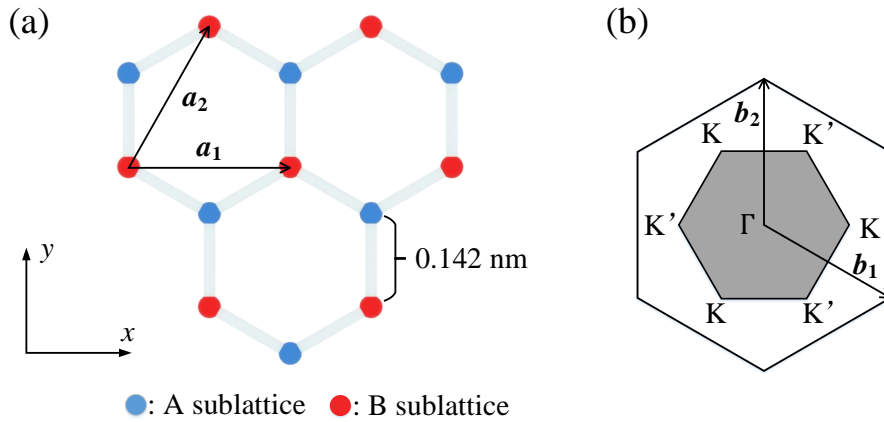


Fig. 2.1 (a) Hexagonal crystal structure of graphene.  $\vec{a}_1$  and  $\vec{a}_2$  are base vectors of the triangular Bravais lattice. (b) Reciprocal lattice of graphene with base vectors  $\vec{b}_1$  and  $\vec{b}_2$ . The shaded region shows the first Brillouin zone with its centre ( $\Gamma$ ) and the two sets of inequivalent corners (K and K').

Carbon has six electrons in the orbital configuration  $1s^2 2s^2 2p^2$ , two of which are in the core  $1s$  orbital, while the other orbitals hybridize, forming three  $sp^2$  orbitals and one  $p_z$  orbital. The  $sp^2$  orbitals form the  $\sigma$  bond including three localized electrons. The  $\sigma$  bond is responsible for the robustness of the lattice structure and makes it hard for alien atoms to replace the carbon atoms in the lattice. The bonding configuration among the  $p_z$  orbitals of different lattice sites generates a filled valence band ( $\pi$  band), whereas the antibonding configuration generates an empty conduction band ( $\pi^*$  band). The  $\sigma$ -electrons generate energy bands far away from the Dirac point, whereas the  $\pi$ -electrons are responsible for the electronic properties at low energy [28].

The energy bands of graphene are calculated by the tight-binding model [29],

$$E_{\pm}(\vec{k}) = \pm t \sqrt{3 + f(\vec{k})} - t' f(\vec{k}), \quad (2.3)$$

$$f(\vec{k}) = 2\cos(\sqrt{3}a\vec{k}_y) + 4\cos\left(\frac{\sqrt{3}}{2}a\vec{k}_y\right)\cos\left(\frac{3}{2}a\vec{k}_x\right), \quad (2.4)$$

where the plus sign in Equation(2.3) applies to the  $\pi^*$  band and the minus sign applies to the  $\pi$  band,  $t$  is the nearest-neighbor hopping energy, and  $t'$  is the next nearest-neighbor hopping energy. Figure 2.2 shows the band structure of graphene with both  $t$  and  $t'$ . The valence band ( $E < 0$ ) and the conduction band ( $E > 0$ ) touch each other at six discrete points at the corners of the Brillouin zone. The six points (K and K') can be divided into two inequivalent groups, the points within each group are all equivalent because they can reach each other by reciprocal lattice vectors. Since each carbon atom contributes one electron, the valence band is completely filled up to the Fermi level. From the zoom in band structure close to one of the DPs (K or K'), the energy spectrum in graphene is linear and the electrons move at a constant speed ( $v_F$ ) which is  $\sim 10^6$  m/s. Due to its peculiar lattice structure and dispersion relation, the electron density of states vanishes at the DP and hence graphene is neither a metal nor an insulator because there is no an open gap in the spectrum [30].

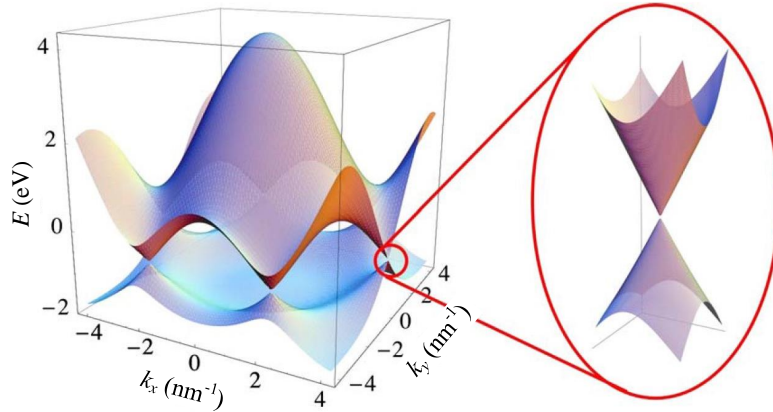


Fig. 2.2 Energy band of graphene. (Left) Energy spectra in units of  $t$  for finite values of  $t = 2.7$  eV and  $t' = (-0.2t)$ . (Right) Zoom in of the energy band close to one of the DPs. Reprinted with permission from [31]. Copyright (2009) American Physical Society.

### 2.1.2 Electrical properties

In graphene, the backscattering is suppressed due to the Berry's phase induced by the rotation of pseudospin from inherent sublattice symmetry [32]. Therefore electrons can propagate over long distance of the order of micrometers [7] and carrier mobility in graphene could be extremely high even at room temperature. However, intrinsic scatterers such as phonons which can not be eliminated at room temperature and set a limit on the mobility. It has been

proposed that  $200,000 \text{ cm}^2 \text{ V}^{-1} \text{ s}^{-1}$  is the upper limit of intrinsic mobility for graphene at 300 K [33]. And indeed mobility as high as  $180,000 \text{ cm}^2 \text{ V}^{-1} \text{ s}^{-1}$  at room temperature has been reported [6].

At low temperature, corrections may happen to the classical expressions for the conductivity due to quantum effects [34, 35]. In a conventional two-dimensional electron system, the scattering amplitude and associated phase of each process equal its complementary time-reversal process. This constructive interference leads to the enhancement of the backscattering amplitude and the localization of the electron states. The probability that the electrons go back to the origin is enhanced, so that quantum corrections decrease the conductivity. This mechanism is known as weak localization. In graphene, each scattering process leads to a rotation of the pseudospin, and a change of the corresponding wave-function phase. This leads to a destructive interference for the backscattering. Therefore, the non-trivial quantum correction to the conductivity in graphene should have a positive sign without intervalley scattering, known as weak antilocalization. In general, the correction depends on the relative value of intravalley ( $\tau_{intra}$ ) and intervalley ( $\tau_{inter}$ ) elastic scattering time, weak antilocalization happens when  $\tau_{intra} \ll \tau_{inter}$ , otherwise weak localization will take place.

The ambipolar field-effect in graphene is shown in Figure 2.3. The carrier density can be tuned continuously between holes and electrons by applying a gate voltage [7]. Under a negative gate voltage, the Fermi level drops below the DP, introducing a significant population of holes into the valence band. Under a positive gate voltage, the Fermi level rises above the DP, promoting a significant population of electrons into the conduction band.

### 2.1.3 Raman spectroscopy

Raman spectroscopy is a tool to measure atomic vibrational energy in materials and phonons in crystals. Raman spectra fall into two spectrum ranges, in terms of energy scale, an ultra-low frequency ( $< 100 \text{ cm}^{-1}$ ) and a high frequency ( $> 100 \text{ cm}^{-1}$ ). In general, Raman spectra are measured in the high frequency range because of the cut-off limit of Raman filters used in the Raman spectrometer. In the high frequency, Raman spectroscopy is used to determine the number and orientation of layers, the quality and types of edge, defects, strain and doping. There is a damage threshold of the laser power for measuring the thin layer of two-dimensional materials. Typically, the power should be kept below 1 mW for single layer graphene.

Graphene has an open surface and hence is readily accessible by Raman spectrometer to investigate phonons, electron-phonon, magneto-phonon, and electrons interactions. The gapless structure of graphene makes all wavelengths of incident radiation resonant, then Raman spectra have information about atomic structure and electronic properties. A typical

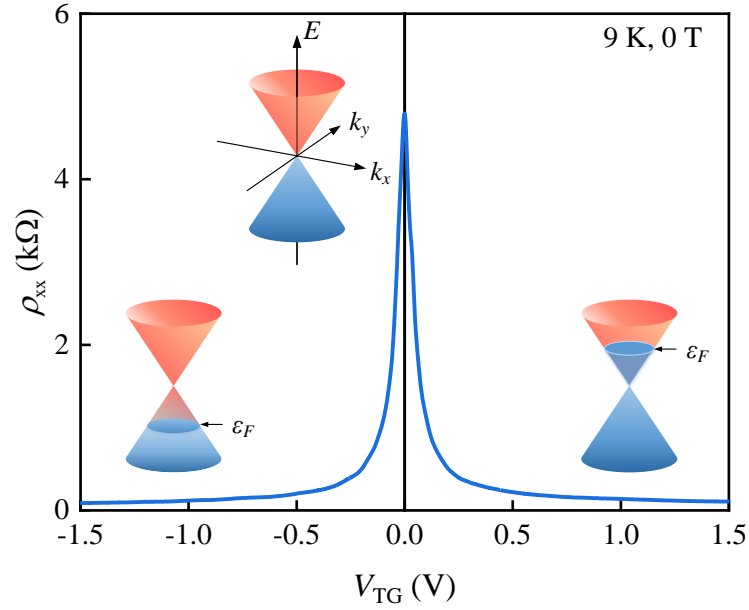


Fig. 2.3 Ambipolar electric field effect in single layer graphene showing longitudinal resistivity ( $\rho_{xx}$ ) versus gate voltage ( $V_{TG}$ ). The insets show the low-energy spectra  $E(k)$  with  $V_{TG}$ .  $\varepsilon_F$  is Fermi level.

514 nm Raman spectrum of graphene (Figure 2.4) consists of two main peaks, the G peak ( $\sim 1580 \text{ cm}^{-1}$ ) and 2D peak ( $\sim 2700 \text{ cm}^{-1}$ ). The G peak is due to the high-frequency  $E_{2g}$  phonon at the centre of Brillouin zone. If graphene has defects, additional peaks such as the D, D' and their combination D+D' peaks appear. The 2D and 2D' peaks originate from a process where momentum conservation is satisfied by two phonons with opposite wave-vectors, and these two types of peaks are always present. The 2D peak of graphene changes in shape, width, and position for different numbers of layers [36–39] (Figure 2.5), reflecting the change in the electronic band structure.

To interpret Raman spectrum, it is fitted with a Lorentzian-distribution function, which has peak position (Pos), full-width at half-maximum (FWHM), peak height ( $I_p$ ) and area ( $S$ ). For single layer graphene, it can be fitted with a single peak Lorentzian function, while in bilayer graphene it splits into four components due to the evolution of the band structure. For more than five-layer graphene, the 2D peak shape is similar to that of graphite. Raman spectroscopy can also be used to determine the doping level [41–43]. In doped graphene, Pos(G) increases due to the removal of non-adiabatic Kohn anomalies, while FWHM(G) decreases due to the Pauli blocking of the phonon decay channel into electron-hole pair from the increase of Fermi level [42, 44–46]. Pos(2D) shifts up for hole doping and down

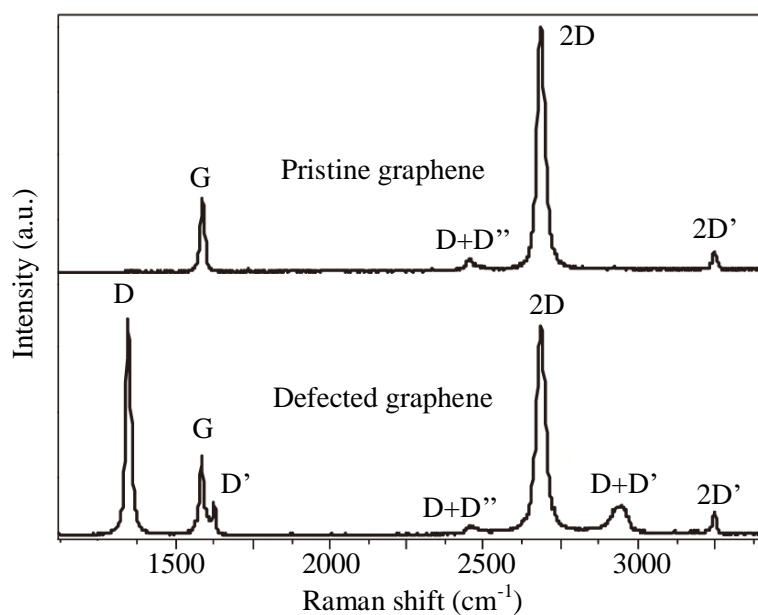


Fig. 2.4 Raman spectra (514 nm) of pristine (top) and defected (bottom) graphene. Reprinted with permission from [36]. Copyright (2013) Springer Nature.

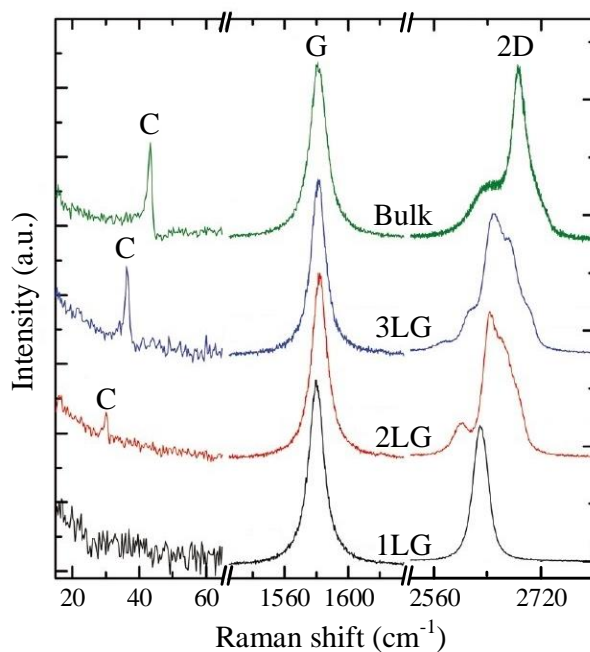


Fig. 2.5 Raman spectra (633 nm) of single layer graphene (1LG), bilayer graphene (2LG), trilayer graphene (3LG) and bulk graphite. Reprinted with permission from [40]. Copyright (2013) American Chemical Society.

for electron doping due to the change of the equilibrium lattice parameter.  $I_p(2D)/I_p(G)$  and  $S(2D)/S(G)$  maximize for zero doping and decrease for higher doping [45]. Strain can occur in graphene compressed or stretched out of equilibrium. Compressive strain causes an upshift of the Raman peaks, but tensile strain causes a downshift. Biaxial strain does not cause any change in peak shape, while uniaxial strain causes splitting of the G peak into two components  $G^+$  and  $G^-$  for mechanical strain more than 0.5% [47].

## 2.2 Hexagonal boron nitride

Born nitride is a wide band gap III-V compound with remarkable physical properties and chemical stability. Hexagonal boron nitride (hBN) is an insulating isomorph of graphite with boron and nitrogen atoms occupying the inequivalent A and B sublattices in the Bernal structure, consisting of  $sp^2$  bonds. Within each layer of hBN, boron and nitrogen atoms are connected by strong covalent bonds, whereas the layers are held together by weak van der Waals forces. Figure 2.6 shows the two-dimensional hexagonal lattice of BN, composed of boron and nitrogen atoms.

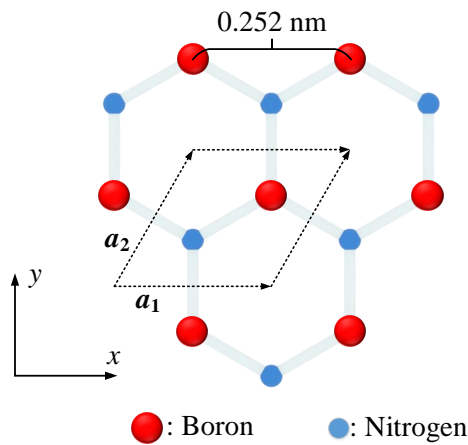


Fig. 2.6 Hexagonal crystal structure of BN. The unit cell is represented by enclosed lattice vectors ( $\vec{a}_1$  and  $\vec{a}_2$ ).

The different on-site energy of the boron and nitrogen atoms result in a large direct band gap (5.97 eV) [48] but a small lattice mismatch with graphite (1.8%) [49]. hBN is relatively inert and is expected to be free of dangling bonds or surface charge traps, due to the strong in-plane ionic bond of the planar hexagonal lattice structure. Moreover, rippling in graphene can be suppressed by the atomically planar surface, which has been proved to mechanically conform to both corrugated and flat substrate [50, 51]. The dielectric constant (3 – 4) and

the breakdown field ( $\sim 0.8 \text{ V nm}^{-1}$ ) of hBN are similar to those of  $\text{SiO}_2$ , meaning hBN can be used as an alternative gate dielectric material [51].

There are two main Raman peaks in hBN, the C peak near  $50 \text{ cm}^{-1}$  and a high frequency  $E_{2g}$  mode near  $1366 \text{ cm}^{-1}$  [52] (Figure 2.7). The C peak can be used to estimate the number of hBN layer [53, 54]. The high frequency  $E_{2g}$  peak is insensitive to layer number, Pos( $E_{2g}$ ) of  $\sim 1368 \text{ cm}^{-1}$  for the single layer hBN and  $\sim 1366 \text{ cm}^{-1}$  for bulk hBN [54–57].

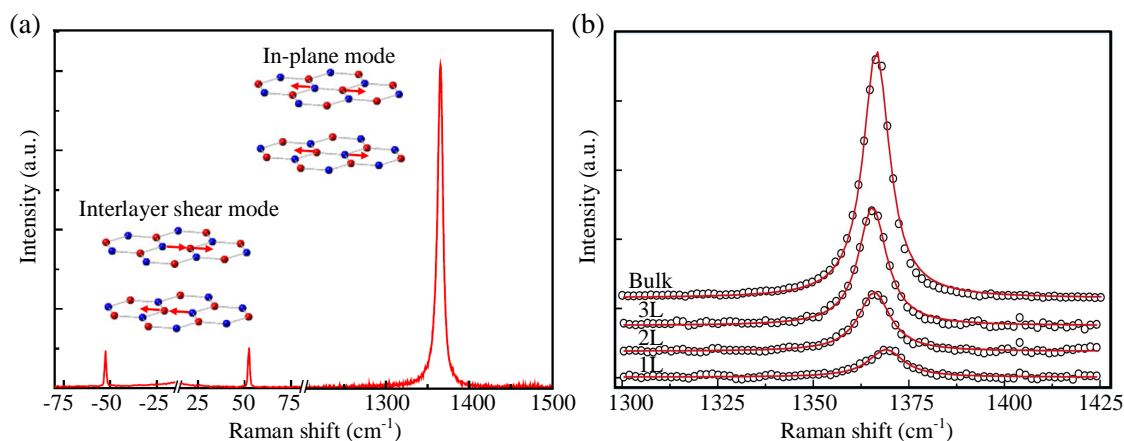


Fig. 2.7 Raman spectra of BN. (a) Raman spectrum of bulk BN. The insets illustrate the phonon mode responsible for the Raman peaks. Reprinted with permission from [53]. Copyright (2017) IOP Publishing. (b) Raman spectra of single layer BN (1L), bilayer BN (2L), trilayer BN (3L) and bulk BN at high frequency ( $E_{2g}$ ) mode. Reprinted with permission from [58]. Copyright (2011) John Wiley and Sons.

## 2.3 Summary

Two-dimensional van der Waals crystals exhibit unique electronic, optical, mechanical and chemical properties. Graphene's charge carriers behave as massless Dirac fermions, have extremely high mobility and remarkable optical properties, which can be detected via Raman spectra. However pristine graphene does not have a band gap, which limits its use in digital logic transistors. hBN is an ideal two-dimensional insulator and can be used as the atomically flat substrate for graphene as well as dielectric layer.

# Chapter 3

## Localized magnetism

Magnetism is attributed to electron motion and interactions, which create orbital (around the nucleus of atom) and spin (around the electron axis) magnetic moments. The combination of these two leads to a material-dependent atomic magnetic moment, which determines the nature of the magnetism. For paired electrons, total magnetic moment is zero as the opposite directions of spins cancel out by each other. On the other hand, materials with unpaired electrons show a net magnetic moment. This chapter reviews basic theories used to describe magnetism in magnetic insulators.

### 3.1 Magnetism in magnetic insulators

Magnetism relates to magnetic moments and their behavior in an applied magnetic field ( $\vec{H}$ ). The Zeeman energy is  $E_Z = -\mu_0 \int \vec{H} \cdot \vec{M} dV$ , where  $\vec{M}$  is the magnetization of the material and  $\mu_0 = 4\pi \times 10^{-7} \text{ H m}^{-1}$  is the permeability of free space. The magnetic induction or magnetic flux density  $\vec{B}$  is related to  $\vec{H}$  through  $\vec{B} = \mu_0(\vec{H} + \vec{M})$ . And  $\vec{M} = \chi\vec{H}$ , where  $\chi$  is the magnetic susceptibility. Then  $\vec{B} = \mu_0(1 + \chi)\vec{H} = \mu_0\mu_r\vec{H}$ , where  $\mu_r = 1 + \chi$  is a relative permeability .

In a magnetic insulator, the magnetization originates from individual atomic-like localized magnetic moments. The strength of the magnetic interactions between two neighboring localized moments ( $M_i$  and  $M_j$ ) is described by an exchange interaction, resulting from the overlap of the localized orbitals of electrons. The exchange energy ( $E_{ex}$ ) was first proposed by Heisenberg in 1926 [59] to demonstrate the origin of the molecular field, i.e.  $E_{ex} = -\sum_{ij} J_{ij} \vec{S}_i \cdot \vec{S}_j$ , where  $J_{ij}$  is the strength of the exchange interaction between the spins of magnetic ions on sites  $i$  and  $j$ , and  $\vec{S}_i$  is the spin operator on site  $i$ . For a two-spin system,  $S_1 = S_2 = 1/2$ , the charge distribution depends on the relative orientation of the spins. The splitting between parallel and antiparallel spin configurations is given by  $E^{\uparrow\downarrow} - E^{\uparrow\uparrow} = J_{12}$ .

Since the exchange interaction is short-ranged,  $J_{12}$  is maximum for nearest-neighbour spins. When  $J_{12} > 0$ , the exchange energy is minimal, leading to the ferromagnetism, i.e. parallel spin configurations; while  $J_{12} < 0$  gives rise to the antiferromagnetism, i.e. antiparallel configurations.

## 3.2 Magnetocrystalline anisotropy

The magnetization in a material tends to align with one or several energetically favored directions (known as easy axes). The energy consumption for rotating the magnetization away from an easy axis to a hard axis is the magnetic anisotropy energy [60]. Magnetocrystalline anisotropy in the case of materials with a single axis (i.e. hexagonal, tetragonal and rhombohedral crystals) is uniaxial, but in the case of materials with two dominant axes (i.e. monoclinic, triclinic and orthorhombic crystals) is biaxial. The easy axis direction is normally determined by a competition of magnetocrystalline anisotropies, which microscopically originate from the spin-orbit coupling and shape anisotropy. In thin films, the easy axis is usually in-plane due to the predominant of shape anisotropy. Anisotropy energy can be estimated from the magnetic hysteresis loop by measuring loops at various angles between the applied magnetic field and the easy axis.

A magnetic domain is the region inside a magnetic material where the magnetization is oriented along a given direction. In general, a magnetic material contains many domains where the magnetization is along one direction to minimize the magnetostatic energy. Neighboring domains with opposite magnetization are separated by a domain wall. The domain wall results from a competition between exchange and anisotropy energy, which is narrow for either high anisotropy energy or low exchange energy. There are two common types of domain walls. In a Bloch wall, the magnetization rotates  $180^\circ$  in a plane parallel to the plane of the wall. In a Néel wall, the magnetization rotates in a plane perpendicular to the plane of the wall [61]. Bloch wall prefers to occur in bulk-like films, while Néel wall is predominant in thin films, where the stray field is reduced by a rotation of the magnetization within the surface plane [60, 61].

## 3.3 Magnetic hysteresis

Magnetization is a behavior that explains the extent to which a magnetic material is influenced by an applied magnetic field. The typical magnetic hysteresis loops are shown in Figure 3.1. In low magnetic fields, a reversible nucleation of magnetic domains is initiated along the path O-a in Figure 3.1(a), meaning that if the magnetic field decreases, the magnetization

will decrease to zero following the same path as domain walls are pinned by impurities. In high magnetic fields, the domain walls are depinned and able to move along the path a-b. Irreversible path b-c is related to the free domain wall movement. The magnetic moment rotation along the path c-d will change the magnetization. When the applied magnetic field is reversed towards  $-H_c$ ,  $M$  changes along the path d-e-f, which is different from initial path.

The saturation field ( $H_{\text{sat}}$ ) is the applied magnetic field for achieving an aligned single domain state, and the magnetization at this field is saturation magnetization ( $M_s$ ). The coercive field is defined as  $H_c$  which reduces the magnetization to zero. The remanent magnetization ( $M_r$ ) is the leftover magnetization when the applied magnetic field is decreased to zero. The ratio  $M_r/M_s$  is close to 1 when the applied magnetic field is aligned with the easy axis. Therefore the hysteresis loop is close to square [Figure 3.1(b); thin line] compared to when magnetic field is aligned with the hard axis [Figure 3.1(b); thick line].

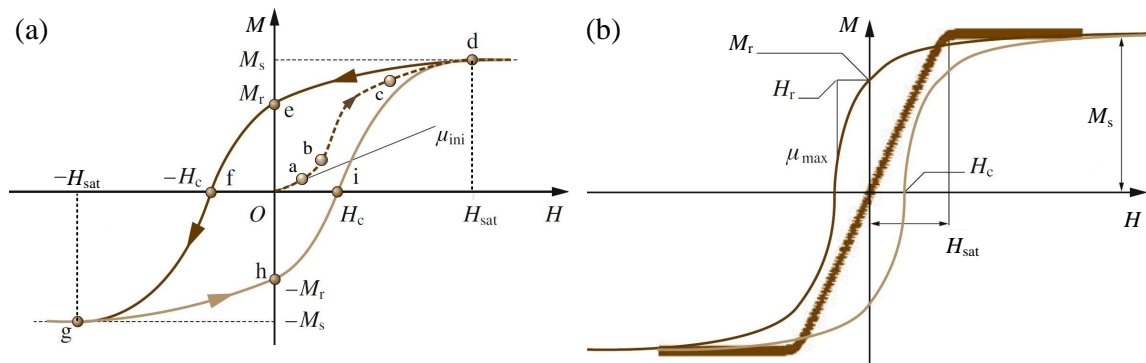


Fig. 3.1 Magnetic hysteresis loops. (a) Magnetization ( $M$ ) versus applied magnetic field ( $H$ ) hysteresis loop. The dashed line with arrow shows the initial magnetization curve of a demagnetized material with permeability of  $\mu_{\text{int}}$ . (b) Magnetic hysteresis loops for a ferromagnetic material along its easy axis (thin line) and hard axis (thick line). Reprinted with permission from [62]. Copyright (2017) Springer Nature.

### 3.4 Magnetic properties of materials

All materials can be classified into: diamagnetic, paramagnetic, ferromagnetic, ferrimagnetic and antiferromagnetic materials on the basis of magnetic moment direction in an applied magnetic field. Accordingly, there are five corresponding magnetism existing in nature including diamagnetism, paramagnetism, ferromagnetism, ferrimagnetism and antiferromagnetism.

### 3.4.1 Diamagnetism

A material exhibits diamagnetism whenever the constituent atoms have closed shells and subshells, which means each constituent atom has no permanent magnetic moment in the absence of an applied magnetic field. For graphene, it doesn't consist of  $d$  or  $f$  electrons, so the magnetic moment formation would be non-trivial and pristine graphene is strongly diamagnetic [63]. When a diamagnetic material is placed in a magnetic field ( $B$ ), the magnetization in the material is in the opposite direction to the applied magnetic field in order to cancel out  $B$ . This interaction is very weak, so the susceptibility is typically  $-10^{-5}$  for solid and liquid materials.

### 3.4.2 Paramagnetism

Paramagnetism occurs in materials that show permanent magnetic dipole moments due to unpaired electron spins. In the absence of an applied magnetic field, the directions of magnetic dipole moments are aligned randomly as a result of thermal agitation. An applied magnetic field tends to align magnetic moments and leads to a magnetization along with the same direction of the applied magnetic field. Therefore the magnetization of a paramagnetic material depends on the sum of Zeeman effect and thermal agitation. In low magnetic fields, magnetization ( $M$ ) is proportional to the applied magnetic field ( $H$ ). And the susceptibility is inversely proportional to temperature described by Curie-Weiss law [64, 65],

$$\chi = \frac{C}{T - T_C}, \quad (3.1)$$

where  $C$  is Curie constant and  $T_C$  is the Curie temperature. The equation is only valid for  $T > T_C$ . Paramagnetic material has a positive but small susceptibility  $\sim 2 \times 10^{-5}$  at room temperature. At low temperatures ( $T < T_C$ ) or high magnetic fields,  $M \propto H$  is no longer valid because of saturation magnetization. Then the susceptibility does not follow the Curie-Weiss law.

### 3.4.3 Ferrimagnetism

The ferromagnetic, ferrimagnetic, and antiferromagnetic behaviors can be described in terms of susceptibility and temperature. The Curie temperature ( $T_C$ ) signals the onset of ferromagnetic order and the Néel temperature ( $T_N$ ) signals the onset of antiferromagnetic order from paramagnetic disorder. There is a local Heisenberg exchange interaction between atomic moments in ferromagnetic, ferrimagnetic, and antiferromagnetic materials, which can be described as an exchange field [59].

A ferromagnet is made of magnetic moments with a positive exchange field that will minimize their energy by aligning the magnetic moments parallel to each other with a net total magnetization. The ordering effect of the exchange field is opposed by thermal agitation, and when temperature is increased above the  $T_C$ , the material becomes paramagnetic. The magnitude of the exchange field can be as high as  $10^3$  T. The value of susceptibility in a ferromagnetic material is positive and large. EuO, EuS and garnets are common ferromagnetic materials [66, 67].

For antiferromagnet, the exchange field between the adjacent atoms leads to the antiparallel configuration of the atomic magnetic moments, which shows a zero net magnetization. If the antiferromagnetic crystal is made of two interlocking sublattices, it has parallel magnetic moments inside each sublattice but with oppositely equal magnetization. The susceptibility reaches its maximum value at  $T_N$  where there is a kink in the curve. Oxides are generally antiferromagnetic materials except EuO [67, 68].

The intermediate order between ferromagnet and antiferromagnet is a ferrimagnet, which is usually used in microwave devices [69]. For the ferrimagnetic insulator, following the analysis of the antiferromagnet, it is possible to consider the crystal as being made of two nonequivalent sublattices with opposite magnetization. Because the magnitude of each magnetization is different, leading to a net spontaneous magnetization as a ferromagnet but with a relatively small value. The intrinsic exchange interaction is still antiferromagnetic and the ordering temperature is  $T_N$ . Ferrite is a common ferrimagnetic material, which has the chemical formula of  $MO \cdot Fe_2O_3$ , where M is a divalent cation, i.e.  $Zn^{2+}$ ,  $Cd^{2+}$ ,  $Fe^{2+}$ ,  $Ni^{2+}$ ,  $Cu^{2+}$ ,  $Co^{2+}$  or  $Mg^{2+}$ .

### 3.5 Yttrium iron garnet

Ferrimagnetism in yttrium iron garnet ( $Y_3Fe_5O_{12}$  or YIG) was discovered by Bertaut and Forrat in 1956 [70], then by Geller and Gilleo in 1957 [71] independently. YIG is regarded as the prototype of magnetic garnet. Garnet has a chemical formula of  $A_3B_2C_3O_{12}$  with a cubic unit cell of  $(A_3B_2C_3O_{12})_8$  [72], where A is a large dodecahedral site, B is a moderate-size octahedral site, and C is a small tetrahedral site (Figure 3.2). The crystal structure of garnets belongs to the symmetry point group of  $Ia\bar{3}d$  and the lattice constant is  $12.376 \pm 0.004$  Å. The lattice spacing of allowed (004) reflection corresponds to the charge neutrality layer that is 1/4 of the unit cell length, which is also valid for [111] and [110] directions. The  $T_C$  of YIG is above room temperature (550 K) which is due to the B-C site interaction. YIG has a cubic magnetocrystalline anisotropy with an easy axis along the [111] direction and a hard

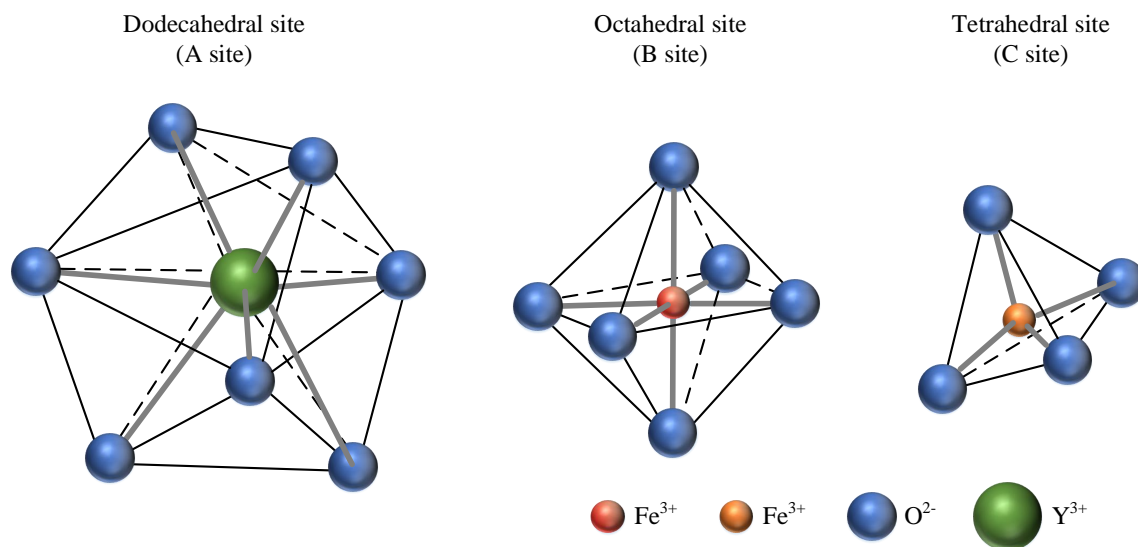


Fig. 3.2 Schematic diagrams of A, B, and C sites occupied by Y<sup>3+</sup> and Fe<sup>3+</sup> in YIG.

axis along the  $[1\bar{1}0]$  direction. The magnetic anisotropy of YIG is preserved as well as that of the crystallographic anisotropy, regardless of the shape anisotropy of the YIG films.

In YIG, the Y<sup>3+</sup> ions on the A site are diamagnetic and have no permanent magnetic moments. The Fe<sup>3+</sup> ions on the B and C sites antiferromagnetically couple to each other, which results in a net magnetization. The magnitude of the exchange interaction between Fe<sup>3+</sup> ions on the B and C sites depends on the angle of the Fe-O-Fe bond according to the Néel theory, which is maximum at 180° and minimum at 90°. The largest exchange interaction happens between the nearest Fe<sup>3+</sup> ions on the B and C sites with a angle of 126.6° [73]. Because each Fe<sup>3+</sup> ion has a magnetic moment of  $5\mu_B$ , each unit cell has a net magnetic moment of  $40\mu_B$ , corresponding to a saturation magnetization of  $196.6 \text{ emu cm}^{-3}$  at 0 K. The saturation magnetization decreases with increasing temperature. YIG thin films at room temperature typically have a saturation magnetization of  $139.3 \text{ emu cm}^{-3}$ .

YIG thin films are usually grown on (111) and (110)-oriented gadolinium gallium garnet (GGG) substrates because the lattice constant difference between the YIG and GGG is extremely small, on the order of 0.01 Å. YIG is also a ferrimagnetic insulator with a band gap of 2.7 eV. Due to the large band gap, YIG exhibits a resistivity of  $\sim 10^{12} \Omega \text{ cm}$  at room temperature [74], which is suitable as a substrate for electronic devices.

## 3.6 Summary

Temperature is a key parameter in magnetism. Above  $T_C$  or  $T_N$ , ferromagnetism or antiferromagnetism is lost. Without an applied magnetic field, spontaneous magnetization can occur in ferromagnetic (ferrimagnetic) materials below  $T_C$  ( $T_N$ ) due to the exchange interaction. Then ferrimagnetic insulator YIG is a promising candidate for spintronic applications as it has a high  $T_C$  (550 K) and thin film can be epitaxially grown on lattice-matched GGG substrates.



# Chapter 4

## Hybrid two-dimensional materials

Graphene exhibits extraordinary mechanical strength and electronic quality. However, weak spin-orbit coupling, diamagnetic property and gapless band structure limit applications in electronic devices. The possibility of stacking multilayer van der Waals heterostructures was demonstrated experimentally in 2011 [75]. Graphene can be modified structurally by placing it on top of either thin films or two-dimensional crystals exhibiting magnetism or spin-orbit coupling. Moreover, crystallographic alignment in van der Waals heterostructures becomes possible with improved transfer techniques, which results in a moiré pattern due to the interaction between stacked crystals [49]. This chapter introduces the graphene-based hybrid two-dimensional systems with hBN and magnetic insulators.

### 4.1 Increased mobility in graphene

Graphene was first exfoliated on SiO<sub>2</sub> due to the high optical contrast between the single layer region and substrate using an optical microscope [76]. The mobility of graphene device is limited by scattering from surface states and impurities [77–79], surface roughness [33, 50] and surface optical phonons [79, 80]. Moreover, near the Dirac point (DP), substrate-induced disorder breaks up the two-dimensional electron gas (2DEG) into an inhomogeneous network of electron and hole puddles, while impurities trapped at the graphene-substrate interface cause doping of the 2DEG away from the DP [78, 81]. Graphene on SiO<sub>2</sub> is always disordered due to the high roughness and trapped charges in the SiO<sub>2</sub>, which reduce the mobility far inferior to the expected intrinsic value [82]. To achieve high mobility, the substrate should be removed or changed with low roughness. It has been demonstrated that the mobility of suspended graphene by current annealing exceeds 100,000 cm<sup>2</sup> V<sup>-1</sup> s<sup>-1</sup> for  $n_{2D} \sim 10^{11}$  cm<sup>-2</sup> at room temperature [83–85], but suspended devices are extremely fragile, and are susceptible to the ambient atmosphere.

hBN is an ideal substrate for graphene because it has a small (1.8%) lattice mismatch with graphite [49], an atomically smooth surface that is relatively free of dangling bonds and charge traps, and a large band gap (5.97 eV) [48, 86]. The atomically planar surface of hBN can suppress rippling in graphene, which has been shown to mechanically conform to both corrugated and flat substrates [50, 51]. Graphene on hBN substrate [Figure 4.1(a)] has mobility that is almost a factor of three improvement over graphene on SiO<sub>2</sub> [86] and electron-hole charge fluctuations are reduced by two orders of magnitude than on SiO<sub>2</sub> [87]. Graphene device on hBN shows reduced roughness, intrinsic doping and chemical reactivity. Furthermore, graphene encapsulated with two pieces of hBN crystals [Figure 4.1(b)] exhibits robust room-temperature ballistic transport over distance of 1 μm and has mobility of more than 100,000 cm<sup>2</sup> V<sup>-1</sup> s<sup>-1</sup> for  $n_{2D} \sim 10^{11}$  cm<sup>-2</sup> [26]. The encapsulation makes graphene insusceptible to the ambient environment and free from contamination of photoresist used in the electron beam lithography which may affect electronic properties of graphene [88], simultaneously, allows the use of top hBN as an ultra thin gate dielectric layer.

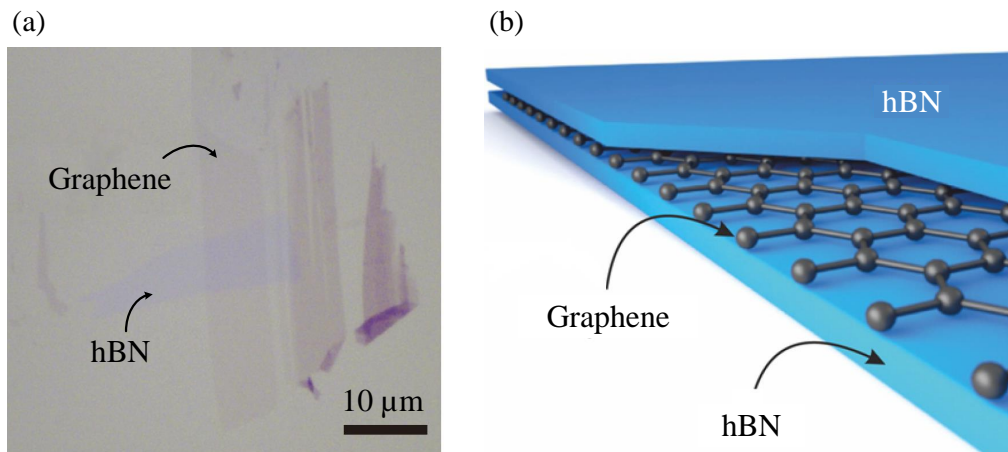


Fig. 4.1 Graphene/hBN structure. (a) Optical image of graphene on hBN. Reprinted with permission from [86]. Copyright (2010) Springer Nature. (b) Schematic illustration of encapsulated graphene with two hBN flakes. Reprinted with permission from [89]. Copyright (2016) American Chemical Society.

## 4.2 Band gap opening in graphene

The band structure of pristine graphene consists of linearly dispersing energy bands, which touch each other at the DPs. This degeneracy is protected by the equivalence of the A and B triangular sublattices and is responsible for graphene's semimetallic behavior [20]. The

absence of a band gap in graphene prevents the Dirac fermions from attaining a finite mass and limits the use of graphene in electronic devices. One method to lift the degeneracy of the conduction and valence bands at the DP is to break the equivalence between the A and B sublattices [90]. It has been proposed that a band gap can be induced in graphene aligning to an hBN crystal [91]. The reconstruction of graphene's band structure is plotted in Figure 4.2.

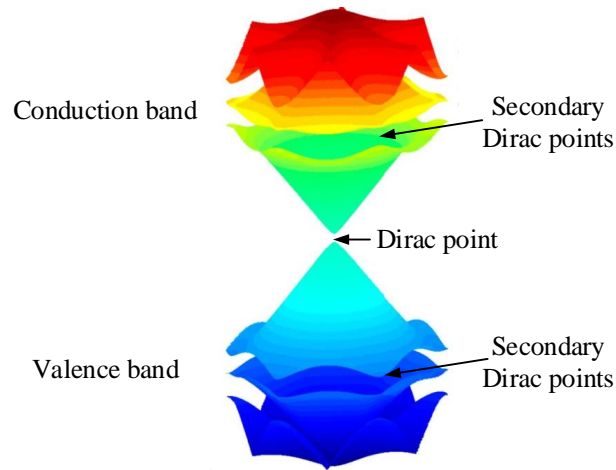


Fig. 4.2 Band structure of graphene on hBN. Secondary Dirac points appear in both conduction and valence bands at the edges of the superlattice Brillouin zones. Reprinted with permission from [92]. Copyright (2015) National Academy of Sciences.

A rotation-angle-dependent ( $\varphi$ ) moiré pattern with wavelength ( $\lambda$ ) occurs when the atoms in the graphene layer form a superlattice structure with the atoms in the hBN layer shown in Figure 4.3. The moiré pattern leads to a modulation of the coupling between graphene and hBN, forming a local asymmetry between the graphene sublattices due to the difference of induced potentials from boron and nitrogen atoms in the hBN. The band gap formed at the DP in graphene is not solely due to the moiré pattern, but also requires orientation-dependent structural relaxation of the carbon atoms, and nonlocal many-body exchange interactions between electrons [93]. The maximum band gap size at the equilibrium layer separation for a perfectly lattice matched hBN/graphene superlattice is predicted to be  $\sim 50$  meV [91]. In general, the band gap size becomes larger when the moiré wavelength increases. A band gap of 27.7-32.0 meV was observed in exfoliated graphene/hBN samples with  $\lambda$  of 12.9-14.0 nm [20, 94, 95]. The epitaxially grown graphene/hBN samples with  $\lambda$  of  $15.6 \pm 0.4$  nm showed a band gap of 160 meV extracted from the band edges in angle-resolved photoemission spectroscopy [91], which suggested that the band gap size increased sharply upon reducing the separation distance between the graphene and hBN layers [91].

The band gap size also depends on the measurement techniques [91], defects and charge impurities [96].

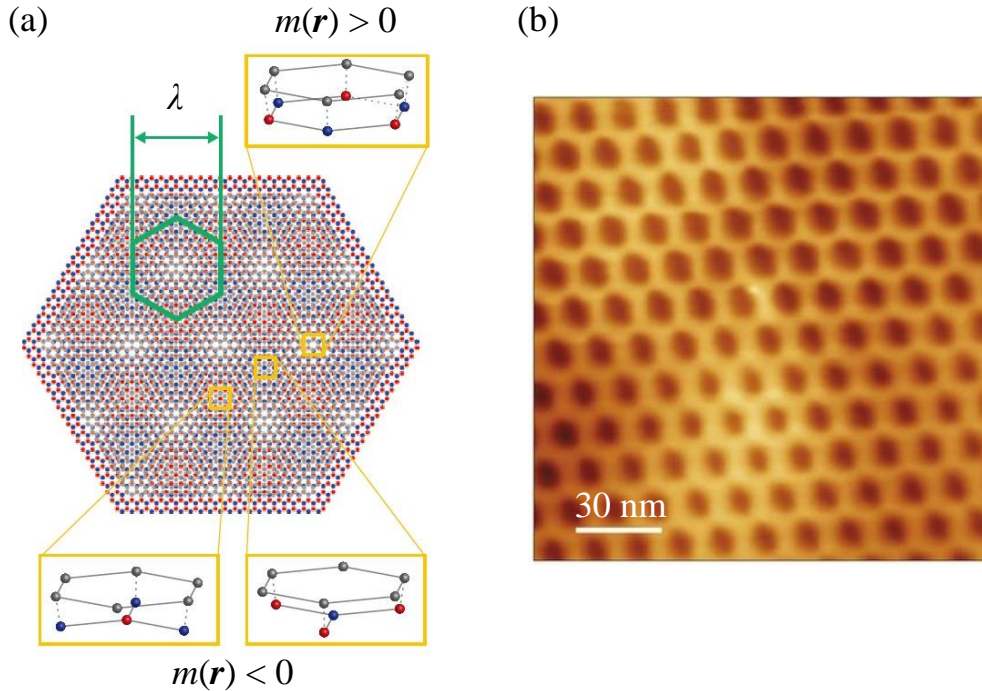


Fig. 4.3 Graphene/hBN superlattice moiré pattern. (a) Schematic of the moiré pattern for an aligned graphene/hBN sample. Green hexagon outlines the moiré unit cell. Local quasi-epitaxial alignment leads to opposite signs of the sublattice asymmetry,  $m(\vec{r})$ , in different regions (gray, carbon; red, boron; blue, nitrogen). Reprinted with permission from [20]. Copyright (2013) the American Association for the Advancement of Science. (b) Scanning tunneling microscopic image of the moiré pattern for aligned graphene/hBN sample. Reprinted with permission from [94]. Copyright (2014) Springer Nature.

### 4.3 Magnetic proximity effect in graphene

The introduction and control of magnetism in graphene can lead to significant advances in electronics, which will utilize the spin degree of freedom. The intrinsic ferromagnetism of graphite and its derivatives is due to the presence of grain boundaries, which can be regarded as two-dimensional periodic network of point-defects [98, 99].

For massless Dirac particles like graphene, localized state is more difficult to establish than in Fermi system because of Klein paradox, where the fermions can easily tunnel through a barrier regardless of its height [30]. Defects are shown to generate localized states in

Table 4.1 Structural details for magnetic materials suitable for graphene-based systems, including the bulk lattice parameter, the lattice mismatch between the magnetic materials and graphene, and the Curie temperature. Reprinted from [97].

Structure	Lattice parameter ( $\text{\AA}$ )	Mismatch (%)	$T_C$ (K)
EuS	5.92	-1.76	16.5
EuO	5.18	0.8	77
$\text{Y}_3\text{Fe}_5\text{O}_{12}$	12.38	2.5	550

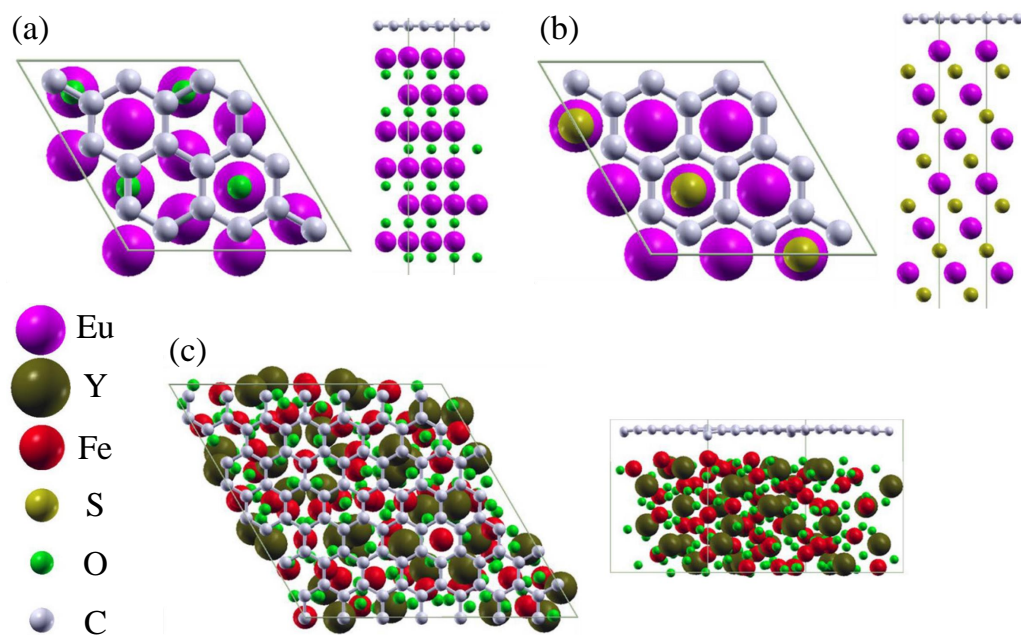


Fig. 4.4 Top and side views of crystalline structures for graphene on top of (a) EuO, (b) EuS and (c)  $\text{Y}_3\text{Fe}_5\text{O}_{12}$ . Adapted from [97].

graphene. Therefore the magnetic properties of graphene can be changed by adatoms or defect engineering [100, 101]. But random impurities from defects cause scattering and reduce the mobility of graphene.

Magnetic proximity effect (MPE) is a more robust and less invasive way to induce magnetism in graphene via a magnetic substrate than other methods [24, 102]. The non-vanishing overlap between the wave-functions of the localized moments in the magnetic insulator and the itinerant electrons in graphene could cause hundreds of meV exchange interaction [24], which is determined by the magnetization direction of magnetic material and the interface properties. MPE in graphene has been explored with EuO [102, 103], EuS [104], and YIG [23, 24]. The structural parameters for these magnetic materials are listed in Table 4.1. In graphene/EuS heterostructure [Figure 4.4(b)], a magnetic exchange field of more than 14 T leads to orders of magnitude enhancement in the spin current detected from nonlocal measurements [104]. Proximity induced magnetism in graphene/YIG [Figure 4.4(c)] is due to the hybridization between the  $\pi$  orbital in graphene and the surface state in YIG, which has been proved by the observation of anomalous Hall effect [23]. Also YIG has advantages over EuS and EuO for a high Curie temperature (550 K) and chemical stability in the air.

## 4.4 Summary

The possibility to combine graphene with other materials has expanded the range of applications. With the advanced fabrication of van der Waals heterostructures and growth of novel two-dimensional crystals, the choices of possible hybrid two-dimensional systems will be unlimited. Two-dimensional hBN flake can be used as a flat substrate or a protective cover for graphene. Encapsulation with hBN preserves devices with consistently high quality under ambient conditions. A rotation-angle-dependent band gap in graphene on hBN is triggered by the moiré pattern. Graphene can be magnetized by the proximity effect from magnetic materials. Moreover, the thermal and chemical stability, and the interfacial contamination from adsorbates such as water and hydrocarbons should be considered during device fabrication and material selection. In addition, the growing interest in hybrid two-dimensional materials for industrial applications will require scalable fabrication approaches. Up to date, several methods have been reported, like epitaxially multilayer growth for graphene, hBN and TMD [105, 106], and layer-by-layer deposition from two-dimensional crystal suspensions [107].

# Chapter 5

## Quantum effects in graphene

Quantum effects are the basis of the next generation electronics, such as quantum communication devices. The high mobility of graphene ( $180,000 \text{ cm}^2 \text{ V}^{-1} \text{ s}^{-1}$  at 300 K [6]) makes it possible to investigate transport phenomena such as quantum Hall effect (QHE) in the extreme quantum limit. In addition, quantum spin Hall effect (QSHE) and quantum anomalous Hall effect (QAHE) have been theoretically predicted based on the honeycomb lattice structure of graphene. This chapter reviews the unconventional QHE in graphene and demonstrates the possibility to achieving QSHE and QAHE in graphene-based systems.

### 5.1 Landau level

In an out-of-plane magnetic field ( $B_{\perp}$ ), the electron in two-dimensional materials goes around in a circular orbit with an angular frequency  $\omega_c = eB_{\perp}/m_e$ , where  $e$  is the electron charge and  $m_e$  is the electron mass. In quantum mechanics, the electron motion has to be quantized. The discrete energy levels ( $E_N$ ) are called Landau levels (LLs), and they are equally separated by the cyclotron energy ( $\hbar\omega_c$ ,  $\hbar$  is the Planck's constant divided by  $2\pi$ ),

$$E_N = \left(N + \frac{1}{2}\right) \hbar\omega_c = \left(N + \frac{1}{2}\right) \frac{\hbar e B_{\perp}}{m_e}, N = 0, 1, 2, \dots, \quad (5.1)$$

which scales proportionally with  $B_{\perp}$ . The density of states  $DOS(E)$  splits into evenly spaced peaks locating at each LL,

$$DOS(E) = \frac{2eB_{\perp}}{h} \sum_N \delta \left[ E - \left(N + \frac{1}{2}\right) \hbar\omega_c \right], \quad (5.2)$$

and each LL has the same number ( $2eB_{\perp}/h$ ) of degenerate states. The factor of two comes from the spin degeneracy. These peaks are ideally  $\delta$  function, but in fact they spread out in energy due to disorder.

For the massless Dirac fermion, the linear energy spectrum implies a linear density of states given by  $E/(2\pi\hbar^2v_F^2)$ , where  $v_F$  is the Fermi velocity. The LL structure of graphene is characterized by the fourfold spin and valley degeneracy [31, 108],

$$E_N = \text{sgn}(N)\sqrt{2e\hbar v_F^2 |N| B_{\perp}}, \quad (5.3)$$

where  $N > 0$  corresponds to electron-like LLs and  $N < 0$  corresponds to hole-like LLs. When the applied magnetic field is increased, there are more available states, and less spacing between the LLs in order to keep the same amount of states for each LL. This is shown in Figure 5.1.

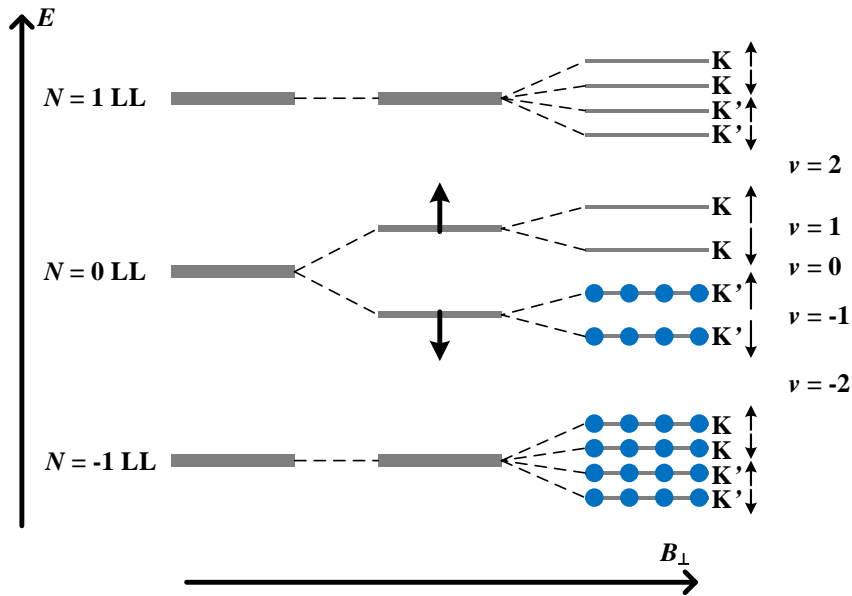


Fig. 5.1 Landau level structure in graphene. Each LL is fourfold degenerate due to two projections of spin and two valleys. At  $\nu = 0$  filling factor, each orbital of the  $N = 0$  LL is occupied on average by two electrons, and LLs with  $N < 0$  are filled.

## 5.2 Quantum Hall effect

When a conductive material carrying a longitudinal current is placed in  $B_{\perp}$ , the charge carriers travel towards the transverse side of the material by a Lorentzian force. Therefore a transverse Hall voltage is developed across the material. The Hall resistance ( $R_{xy}$ ) is the Hall voltage divided by the inject current. The components of the resistivity and conductivity tensors are given by

$$\rho_{xx(xy)} = \frac{\sigma_{xx(xy)}}{\sigma_{xx}^2 + \sigma_{xy}^2}, \quad (5.4)$$

where  $\sigma_{xx}(\rho_{xx})$  is the longitudinal conductivity (resistivity) and  $\sigma_{xy}(\rho_{xy})$  is the Hall conductivity (resistivity). The Hall effect was discovered by E. H. Hall in 1879 [109] shown in Figure 5.2(a). Hall effect is used to measure the carrier density and mobility, and to identify the carrier type. In 1881, E. H. Hall found the anomalous Hall effect (AHE) in ferromagnetic materials. The electrons carry spins and related magnetic moments with a transverse force [Figure 5.2(b)]. The transverse force causes a charge imbalance in the direction perpendicular to the inject current. The predominant origin of AHE is spin-orbit coupling.

In 1980, von Klitzing discovered the integer QHE in the Si/SiO<sub>2</sub> field-effect transistor [110]. QHE can occur in two-dimensional systems with strong out-of-plane magnetic field at low temperature [Figure 5.2(d)]. When the Fermi level is inside a localized state, i.e. between two neighboring LLs, the electrons can move along the edge of the sample in one direction. The states at the edge are defined as the chiral edge states which can carry charge currents without dissipation, because all electrons move in the same direction, and backscattering is prohibited [111]. The vanishing longitudinal conductivity ( $\sigma_{xx} = 0$ ), and quantized Hall conductivity [ $\sigma_{xy} = \pm 4 \frac{e^2}{h} (N + \frac{1}{2})$ ,  $N = 0, \pm 1, \pm 2 \dots$ ] are the hallmark of the QHE. On the other hand, when the Fermi level is in a delocalized state, i.e. Fermi level is crossing a LL, longitudinal conductivity does not vanish, and Hall conductivity varies continuously.

The QHE in graphene (Figure 5.3) is different from that in conventional two-dimensional systems because of the additional 1/2 in the quantized values of  $\sigma_{xy}$ . This half-integer shift is a result of the Berry's phase [32, 112]. The square root dependence ( $E_N \propto \sqrt{B_{\perp}}$ ) leads to a much larger LL spacing than that for electrons with the conventional quadratic dispersion in semiconductors, which enables the QHE to persist up to room temperature [113].

In high magnetic fields, new filling factors may appear from the splitting of the valley or spin degeneracy of the LLs, which can be observed in the appearance of new quantum Hall plateaus [115–118]. The combination of disorder and magnetic field may also lift the valley degeneracy, resulting in valley-polarized states [119]. A band gap can be open due to

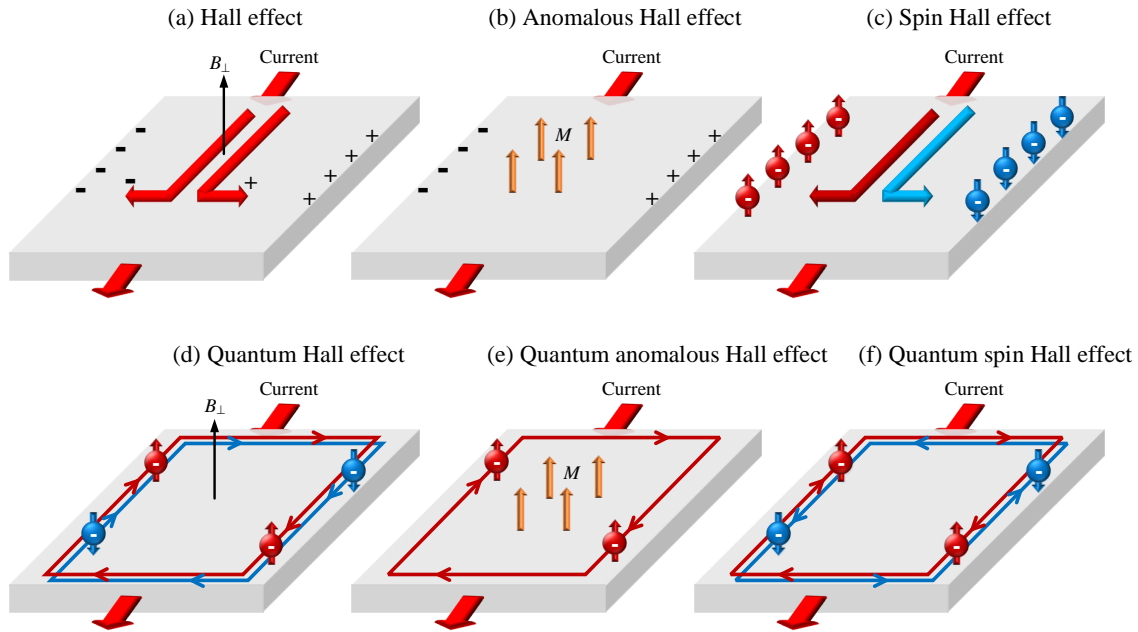


Fig. 5.2 Schematic illustrations of the Hall family: (a) Hall effect; (b) Anomalous Hall effect; (c) Spin Hall effect; (d) Quantum Hall effect; (e) Quantum anomalous Hall effect; and (f) Quantum spin Hall effect.  $B_{\perp}$  is the applied magnetic field perpendicular to the sample surface,  $M$  is the intrinsic magnetization. Red or blue arrows with spheres show the up or down spins. Red and blue lines with arrows show the charge currents in (d) and (e), spin currents in (f).

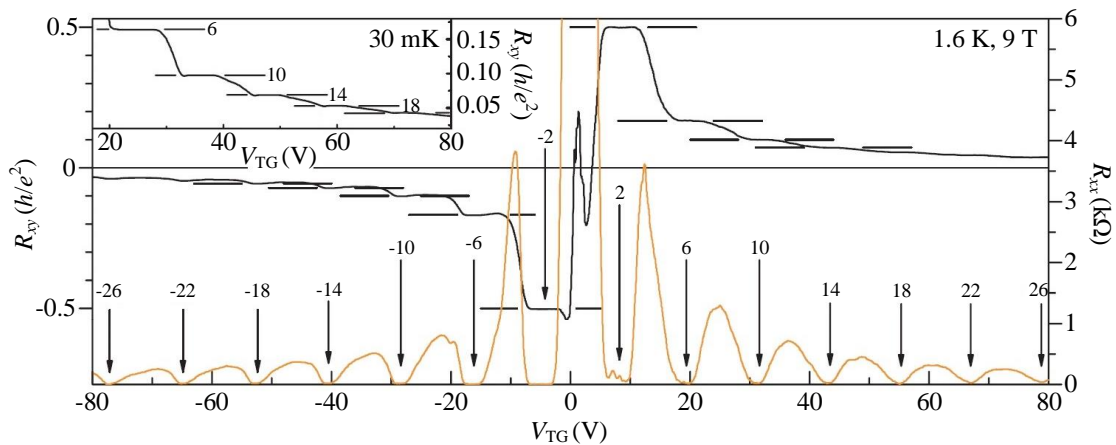


Fig. 5.3 Unconventional quantum Hall effect in graphene.  $R_{xy}$  (black) and  $R_{xx}$  (orange) as a function of gate voltage with  $B_{\perp} = 9$  T at 1.6 K. The vertical arrows and the numbers indicate the corresponding filling factor  $\nu$  of the quantum Hall states. The upper inset shows a detailed view of large filling factor plateaux measured at 30 mK. Reprinted with permission from [114]. Copyright (2005) Springer Nature.

the breaking of valley degeneracy associated with a charge-density wave [120] or a moiré pattern [91].

### 5.3 Quantum spin Hall effect

Spin Hall effect (SHE) was proposed by M. I. Dyakonov in 1971 [121]. Carriers with different spins accumulate at opposite edges of the sample and form the transverse spin current induced by charge currents shown in Figure 5.2(c). Intrinsic SHE is due to spin-orbit coupling and the extrinsic one comes from spin-dependent scattering on impurities [121].

In 2005, QSHE was predicted on the basis of two-dimensional models describing graphene nanoribbons by C. Kane [122]. In a system with spin-orbit coupling, electrons with opposite spins move to different directions in an external electric field due to the opposite direction of forces, which leads to a net spin current [Figure 5.2(f)]. When the Fermi level is inside the bulk gap, the longitudinal conductivity is quantized in units of  $e^2/h$ . Spin-orbit coupling can be regarded as a spin-dependent magnetic field, and electrons with opposite spins have opposite sign of quantized Hall conductivity. A hallmark of QSH state is the existence of gapless edge states which are protected from elastic backscattering and localization by time reversal symmetry [123].

The pure spin current from SHE and QSHE could be used in logic devices, which flows from the injector to the detector via the spin channel. Due to the spin relaxation, the spin-dependent chemical potential exponentially decays during the spin diffusion. For spintronic application, it requires spin channel material with long spin lifetime and long spin diffusion length. Graphene is a promising candidate due to its low spin-orbit coupling and high mobility [15, 63]. But QSHE in graphene was not able to observe as the band gap opened by the spin-orbit coupling is extremely small ( $10^{-3}$  meV) under current experiment conditions [124, 125]. Therefore it has attracted interests to artificially enhance graphene's spin-orbit coupling strength to increase the band gap size, protecting the QSH state to observable levels. It has been demonstrated that the spin-orbit coupling in graphene can be enhanced by proximity effect with other materials exhibiting large spin-orbit coupling such as TMDs [126, 127].

At the same time, QSHE was experimentally observed in topological insulators (TIs), such as (Hg,Cd)Te quantum wells [128, 129], bismuth antimony alloys [130, 131],  $\text{Bi}_2\text{Se}_3$  and  $\text{Bi}_2\text{Te}_3$  bulk crystals [132–135]. TI is a quantum phase of matter with gapless states on the surface or edge and a two-dimensional bulk gap [136]. The edge or the surface states are topologically protected and have a distinct helical property: states with opposite spin-polarization counter-propagate at a given edge [92]. The topological properties of the

QSH state are characterized by a topological invariant ( $Z_2$ ). The time reversal symmetry leads to the topological protection of each Kramers partner and then a suppression of the backscattering. The robustness of the QSH edge states makes TIs promising for quantum spintronic devices.

## 5.4 $\nu = 0$ state

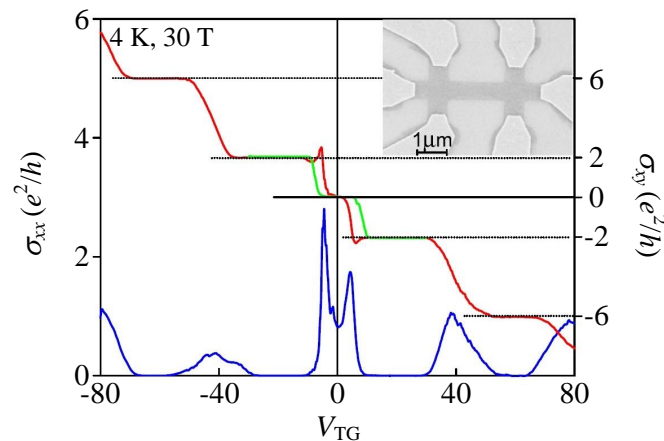


Fig. 5.4 The  $\nu = 0$  state in longitudinal ( $\sigma_{xx}$ ) and Hall ( $\sigma_{xy}$ ) conductivity. The inset shows the device structure. Reprinted with permission from [116]. Copyright (2007) the American Physical Society.

In a strong magnetic field, graphene has spontaneously broken approximate  $SU(4)$  symmetry involving spin and valley degeneracy [137–141]. The  $N = 0$  LL is unusual as it is half-filled in the ground state of undoped graphene. The electron-electron and electron-phonon interactions break the symmetry and determine the ground state of the  $\nu = 0$  state. Zeeman effect is the most obvious anisotropy which naturally favors a spin-polarized state, but the A/B sublattice structure adds additional interaction anisotropy [138] which favors a spin-unpolarized state characterized by sublattice spin or charge-density wave order [142, 143].

In the presence of Zeeman field, the  $\nu = 0$  state has a bulk gap and a pair of edge states with opposite spin-polarization [144, 145]. In the transport measurement,  $\rho_{xx}$  remains finite, but  $\rho_{xy}$  is absent at  $\nu = 0$  state and changes sign without exhibiting a plateau. The bulk conductivity short-circuits the edge state transport and suppresses  $\sigma_{xx}$ , leading to a dip in  $\sigma_{xx}$  and a plateau in  $\sigma_{xy}$ . The spin-split  $\nu = 0$  state can be used to generate and detect spin currents.

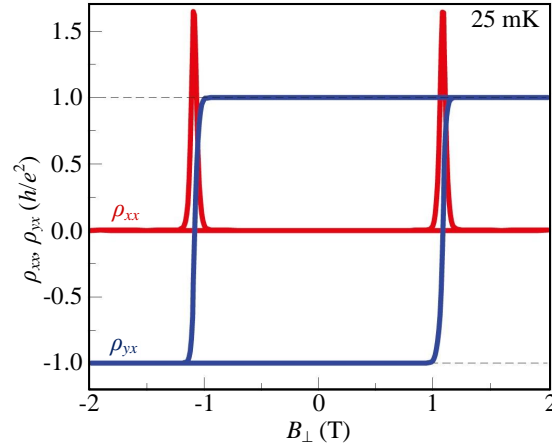


Fig. 5.5 The quantum anomalous Hall effect in magnetically doped TIs. It shows magnetic field dependence of the  $\rho_{xx}$  and  $\rho_{yx}$  at the DP and 25 mK. Reprinted with permission from [146]. Copyright (2015) Springer Nature.

## 5.5 Quantum anomalous Hall effect

QAHE was predicted by F. Duncan and M. Haldane in 1988 [147] and observed in thin films of magnetically doped TIs by C.-Z. Chang in 2013 [148]. QAHE is like the QHE realized in a two-dimensional system where time reversal symmetry is broken [Figure 5.2(e)], which relies on intrinsic magnetization and strong spin-orbit coupling. When the Fermi level is tuned into the gap of the surface state, the Hall resistance exhibits a distinct plateau with the quantized value  $h/e^2$  (25.8 k $\Omega$ ) in zero magnetic field and such quantized value is nearly invariant with the external magnetic field (Figure 5.5), indicating perfect edge conduction and charge neutrality of the TIs. Meanwhile, the longitudinal resistance reaches a value of  $0.098 h/e^2$ .

In theory when graphene is placed on a magnetic material, it forms a hybridization between the  $\pi$ -orbital in graphene and surface states in the magnetic material [149]. A long-range ferromagnetic order is induced in graphene by the magnetic proximity effect. Wang *et al.* achieved AHE in graphene proximity to ferrimagnetic insulator YIG (Figure 5.6), which proved the induced ferromagnetism in graphene with a large exchange field and enhanced spin-orbit coupling [23]. Later Wei *et al.* reported that a 14 T magnetic exchange field was induced in graphene coupling to the semiconducting ferromagnet EuS shown in Figure 5.7 [104]. If both strong exchange field and large spin-orbit coupling are present in graphene, a bulk gap can be formed and the fourfold degenerate LLs become completely non-degenerate. The presence of such a bulk gap indicates an insulating state, which is topologically non-trivial with gapless chiral edge states and exhibiting a quantized Hall

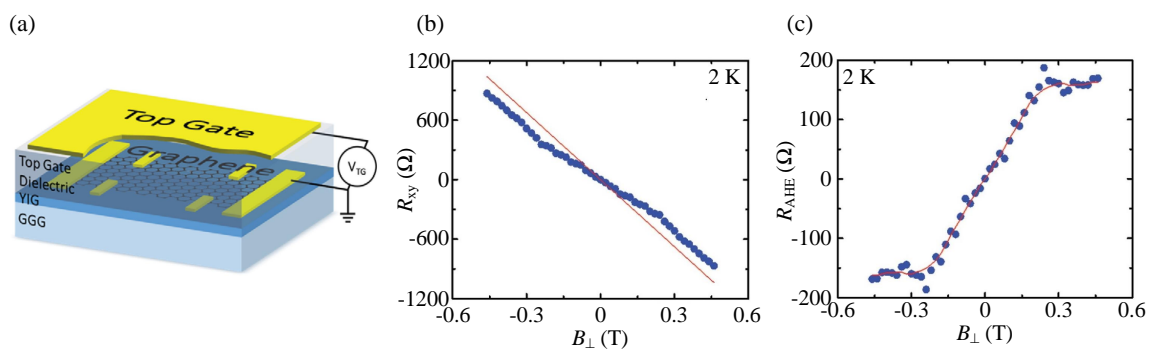


Fig. 5.6 The anomalous Hall effect in graphene on YIG. (a) Graphene device on YIG/GGG with a top-gate electrode. (b) Hall resistivity ( $R_{xy}$ ) versus  $B_{\perp}$  at 2 K with a fitted red line indicating the linear Hall background. (c) The nonlinear Hall resistivity after the linear background is removed from the data in (b). Reprinted with permission from [23]. Copyright (2015) the American Physical Society.

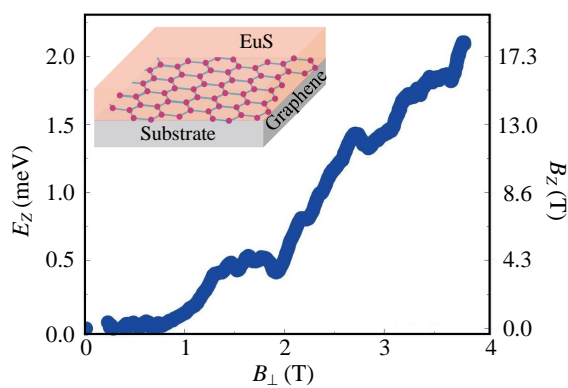


Fig. 5.7 Quantitative estimation of the Zeeman energy ( $E_z$ ) and Zeeman field ( $B_z$ ) in graphene enhanced by the EuS induced magnetic exchange field. Inset shows graphene/EuS hybrid system. Reprinted with permission from [104]. Copyright (2016) Springer Nature.

conductance ( $2e^2/h$ ). In the semiclassical picture, the QAHE can be viewed as a response to the Berry curvature in momentum space rather than the magnetic field in real space.

## 5.6 Summary

The electrons of graphene behave like massless, relativistic Dirac particles, and the chiral nature of the electrons has a fundamental impact on the quantum transport of graphene. The rotation of pseudospin under a magnetic field results in a phase shift of  $\pi$  in the quantum oscillation and leads to an unconventional QHE which is described by half-integer rather than integer values. The spin-split  $\nu = 0$  state can be used to generate and detect spin currents. Due to the weak spin-orbit coupling in pristine graphene, it is impossible to observe the QSHE, but the spin-orbit coupling in graphene can be enhanced by proximity effect. Theoretically a non-trivial bulk gap in graphene can be produced in the presence of large spin-orbit coupling and strong exchange field, which leads to the QAHE.



# Chapter 6

## Experimental methods for device fabrication and measurements

Graphene has extraordinary electrical, mechanical properties and the Dirac cone structure in its low-energy spectrum, which involves three binary internal degrees of freedom: charge, spin and valley [7, 31, 114, 150]. Manipulating these degrees of freedom can effectively control the properties of graphene-based systems. However, for using valley or spin degree of freedom, it requires a band gap and intrinsic magnetism. In order to engineer the band gap and bring long-range ferromagnetic order in graphene from proximity effects, a series of fabrication methods have been developed. This chapter includes all the experimental techniques used in the fabrication and measurements.

### 6.1 Raman spectroscopy

Raman spectroscopy is a fast, accurate and non-destructive tool for characterizing the properties of two-dimensional materials. It does not require any sample preparation or specific substrates and can be performed on electronic devices during operation. Raman spectra are acquired using a Renishaw inVia micro-Raman spectrometer, coupled with Ar<sup>+</sup> and He-Ne lasers emitting at 514.5 nm and 632.8 nm respectively. The spectrometer includes a microscope that serves both for the optical identification of the sample area and for the focusing of the laser beam into a spot of  $\sim 1 \mu\text{m}$  diameter.

Raman scattering includes the inelastic scattering of photons by phonons [151]. Photons impinging on a sample cause a time-dependent perturbation, increasing the total energy to  $E_0 + \hbar\omega_L$ .  $E_0$  is the energy of ground state and  $\omega_L$  is the frequency of the incident photon. In

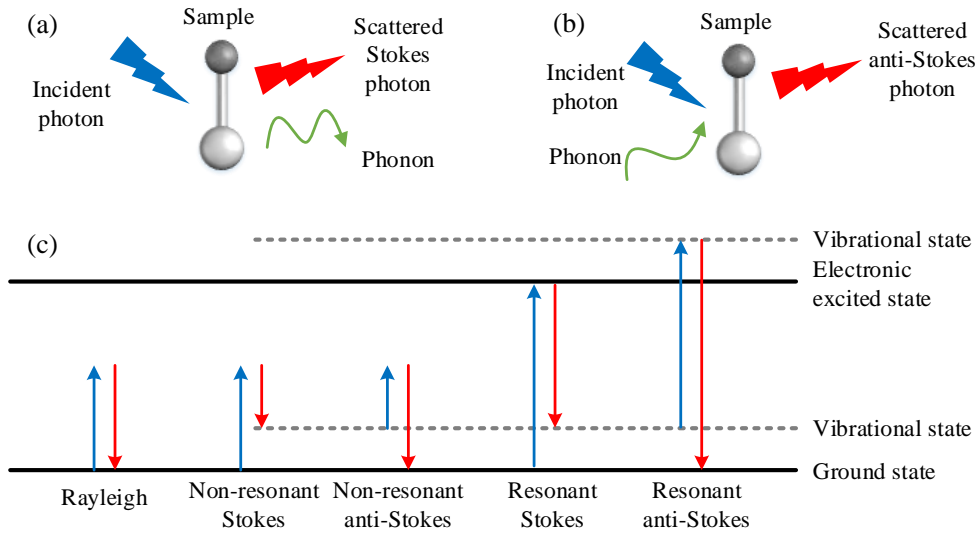


Fig. 6.1 Raman scattering. (a) Stokes scattering. (b) Anti-Stokes scattering. (c) Rayleigh and Raman scatterings in resonant and non-resonant conditions.

general, the total energy is at a virtual level [151]. The perturbed system eventually relaxes to a stationary state with the emission of a photon.

The photon scattering process can be either elastic or inelastic [151]. The elastic case is called Rayleigh scattering, meaning that the emitted photon has the same frequency as the incident one and only changes its propagation direction. But Raman scattering is an inelastic process, where the emitted photon shows a lower or higher energy than the incident one. If the interaction results in the loss of energy, the process is called Stokes scattering. If the sample is in an excited vibrational state and the system returns to its ground state after the interaction, the photon can leave the sample with a higher energy and this process is called anti-Stokes scattering. The most common Raman process is non-resonant that the excitation does not match a specific energy level and therefore the transition involves a virtual state. Instead, when the excitation energy matches an energy level, the process is resonant and the intensities are strongly enhanced. Fundamental Raman selection rules can be derived from energy and momentum conservation, and only phonons with zero momentum can be involved in the first order Raman scattering process. For processes involving more than one phonon, the total momentum has to be zero.

Raman spectra are usually plotted as a function of the wavenumber difference ( $\text{cm}^{-1}$ ) between the incident and scattered photons. Since the Stokes process is more probable, conventionally Stokes shifts are plotted in the positive axis. The intensity corresponding to the number of counts on the charge-coupled device (CCD) at a specific pixel, is plotted

in arbitrary units. Excitations used for Raman spectroscopy are typically in the infrared to ultraviolet spectra range [36]. For this range of wavelength, the photon energy is larger than phonon energy, therefore the main scattering mechanism involves electronic excitations as intermediate states, rather than direct photon-phonon coupling. Any variations of electronic properties change the position, width and intensity of the Raman peaks [36]. Therefore Raman spectra can be used to study the vibrational properties of the materials, and the behaviors of electrons.

## 6.2 Atomic force microscopy

Atomic force microscopy (AFM) is used to characterize the surface topography of materials by using a probe which interacts with the sample's surface. AFM uses a cantilever-tip as a probe and a piezoelectric scanner which moves either the sample or the tip, scanning the surface of the sample line by line [152, 153]. A laser beam is focused on the backside of the cantilever and is reflected onto a photodetector. During scanning, the tip passes above peaks or valleys which causes the cantilever to bend leading to a displacement of the spot at the photodetector. A feedback system keeps the force or the cantilever deflection constant by moving up or down the scanner in the  $z$ -axis, corresponding to the topography. The movement of the feedback generates the image of topography.

The AFM can be operated in different scanning modes. In contact mode, scanning is carried by keeping the force constant and provides high resolution images. However, when the cantilever's stiffness is higher than the sample, it can drag the sample and scratch the surface. To solve this problem, tapping mode was introduced in which the cantilever is oscillating at or near its resonance frequency. Feedback loop keeps oscillation amplitude constant. Latest PeakForce tapping mode is performed at a frequency well below the cantilever resonance, which results in continuous force-distance curves. It shows a better control of the force similar to that applied in contact mode.

Advanced image analysis software is used to visualize the AFM data after measurements, including scanner and tip artifact correction, roughness and cross-section analysis. For two-dimensional materials and thin films, AFM can be used to measure flake size, thickness, and surface roughness. For all the measurements performed in this thesis, the AFM (manufactured by Bruker) was operated in PeakForce tapping mode.

### 6.3 Thin flake preparation

Mechanical exfoliation of high-purity natural graphite is simple and highly reliable to prepare high quality graphene [7]. A schematic illustration of mechanical exfoliation process is shown in Figure 6.2. Graphite is repetitively cleaved by the use of adhesive tape in order to expose a flat and clean surface. Another piece of tape is used to pick a thin and flat graphite flake from the bulk crystal. This flake is then exfoliated 3-5 times in order to uniformly distribute graphite on the tape. A silicon wafer with 285 nm  $\text{SiO}_2$  is used as the substrate which is able to image single layer regions using an optical microscope.  $\text{Si}/\text{SiO}_2$  substrates have been fabricated with alignment markers of Au. Then the substrate is cleaned by acetone, 2-propanol (IPA), and oxygen plasma (100 W, 400 s). The oxygen plasma can increase the adhesion between the graphite flake and the substrate surface in order to improve the size of exfoliated graphene. The clean  $\text{Si}/\text{SiO}_2$  substrate is placed on the tape, bringing its flat surface in contact with the graphite flakes. When the tape is removed, graphite flakes are transferred on the substrate because of van der Waals interactions. The size of transferred graphene varies between several micrometer and millimeter, which is limited by the single crystal grain size of the picked graphite. The quality of graphene flake is measured by Raman spectroscopy and AFM. Mechanical exfoliation is also used for the production of hBN flakes.

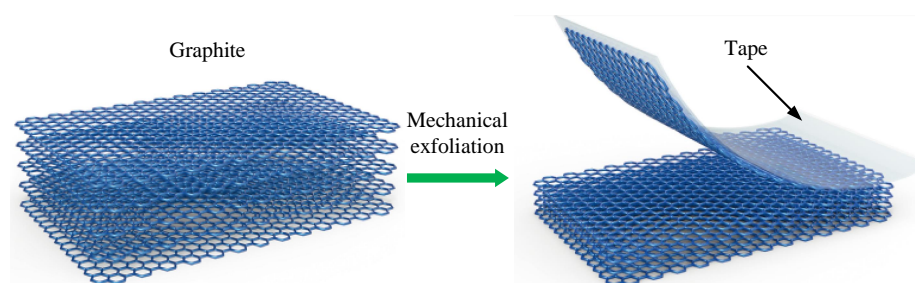


Fig. 6.2 Mechanical exfoliation of graphene. Adapted with permission from [154]. Copyright (2017) Springer Nature.

The single layer graphene on  $\text{Si}/\text{SiO}_2$  can be identified by optical contrast using Nikon LV optical microscope with ImageJ software [155]. Figure 6.3 shows a single layer graphene exfoliated on  $\text{Si}/\text{SiO}_2$  substrate. Despite of low yield, graphene produced by mechanical exfoliation is close to pristine graphene with very few defects. Therefore mechanical exfoliated graphene is widely used in research.

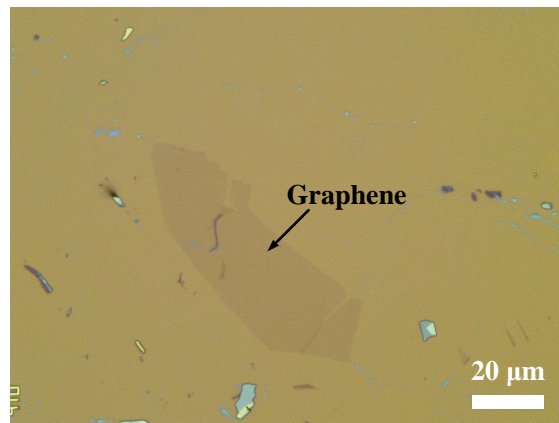


Fig. 6.3 Mechanical exfoliated single layer graphene on Si/SiO<sub>2</sub> substrate.

## 6.4 Thin flake transfer technique

Si/SiO<sub>2</sub> wafers are usually chosen as substrates for two-dimensional materials due to the high optical contrast for identifying the number of layers. However, applications require specific substrates besides Si/SiO<sub>2</sub>. In addition, heterostructures use more than one type of two-dimensional flakes in a stack to achieve tailored properties [156]. Therefore thin flake transfer is one of the most important procedures to build a hybrid two-dimensional systems. Transfer techniques can be classified into two types with respect to water involvement [157]. In a wet transfer method, at least of one side of target material is in contact with water. In a dry transfer method, it uses only organic solvents.

### 6.4.1 Transfer procedures for hBN/graphene/hBN device

hBN/graphene/hBN devices are fabricated by the dry transfer method. Thin flakes of graphene and hBN are prepared by mechanical exfoliation, and are selected by optical microscope and AFM. hBN flakes with thickness of 10-50 nm are used. A stamp is prepared for the transfer process, which includes three layers. The first layer is a piece of thin transparent glass slide for mechanical support. The second layer is a block of polydimethylsiloxane (PDMS) with two adhesive sides, which is transparent and flexible, for connecting the first and third layers. The third layer is an ultra-thin polycarbonate (PC) film, which is prepared by drop casting a solution of PC in chloroform (5 wt%) onto a glass slide and then peeled off by tape. The stamp is attached to a micro-manipulator ( $\sim 1 \mu\text{m}$  resolution of  $x, y, z$  direction) with the PC layer facing down under a microscope. The target flakes on SiO<sub>2</sub>/Si substrates are put on a rotating stage with heater, which is aligned with the stamp and objective lens.

Before transfer, the stage is heated to 40 °C, which improves the successful rate of picking up graphene and hBN flakes. The first step of transfer is to place the PC layer on the stamp to contact with a target hBN flake and withdraw [Figure 6.4(a)]. The hBN adheres to the PC surface and is peeled off from the substrate when the stamp is lifted [Figure 6.4(b)].

To align the crystal lattices, straight and long edges of graphene and hBN flakes are found by the optical microscope, which indicate the principal crystallographic directions. The top hBN for the device is positioned over a chosen graphene flake and the graphene on stage is rotated relatively to the hBN to make their edges parallel. Then the top hBN on the stamp is brought into contact with the graphene with a defined rotating angle [Figure 6.4(c)]. The portion of the graphene in contact with hBN delaminates from the SiO<sub>2</sub>/Si, while that in contact with the PC remains on the SiO<sub>2</sub>/Si, due to the preferential adhesion of graphene to hBN [158] [Figure 6.4(d)]. Stamp/hBN/graphene is then aligned and brought into contact with another hBN flake to encapsulate the graphene [Figure 6.4(e)]. The stage temperature is increased to 180 °C, which is above the glass transition temperature of PC (150 °C) [159]. At 180 °C, the PC layer with stacked hBN/graphene adheres to the bottom hBN on SiO<sub>2</sub>/Si, allowing the PDMS with glass slide to be peeled off [Figure 6.4(f)]. The PC is then removed by rinsing the sample in chloroform [Figure 6.4(g)].

## 6.4.2 Transfer procedures for graphene/YIG device

Single layer graphene on transparent substrate is difficult to identify by optical contrast. But both YIG thin film and GGG substrate are transparent, directly exfoliating graphene on YIG/GGG to find single layer regions is not efficient. Then transfer technique is necessary for the graphene/YIG device fabrication. Both wet and dry transfer methods have been developed to transfer graphene onto YIG/GGG substrates.

Wet transfer method is illustrated in Figure 6.5. A thin layer of poly(methyl methacrylate) (PMMA, Micro Chem,  $M_w = 950,000$ , 8 wt% in anisole) is subsequently spin-coated onto the graphene/SiO<sub>2</sub>/Si without baking. The coated sample is then immersed in deionized (DI) water overnight at room temperature. Because of the water molecules insertion at the SiO<sub>2</sub>-PMMA and SiO<sub>2</sub>-graphene interfaces, the PMMA/graphene is detached from silicon substrate and floats on the water surface. Before transfer, YIG/GGG substrate is fabricated with alignment markers and then cleaned by acetone, IPA and oxygen plasma. PMMA/graphene can be transferred onto the YIG/GGG substrate. The sample is left to dry in the air at room temperature. Finally, the sample is immersed in acetone, leaving only graphene on YIG/GGG. Figure 6.5(f) shows the AFM image of graphene transferred onto YIG/GGG. There are some residues on the graphene surface after dissolving the PMMA.

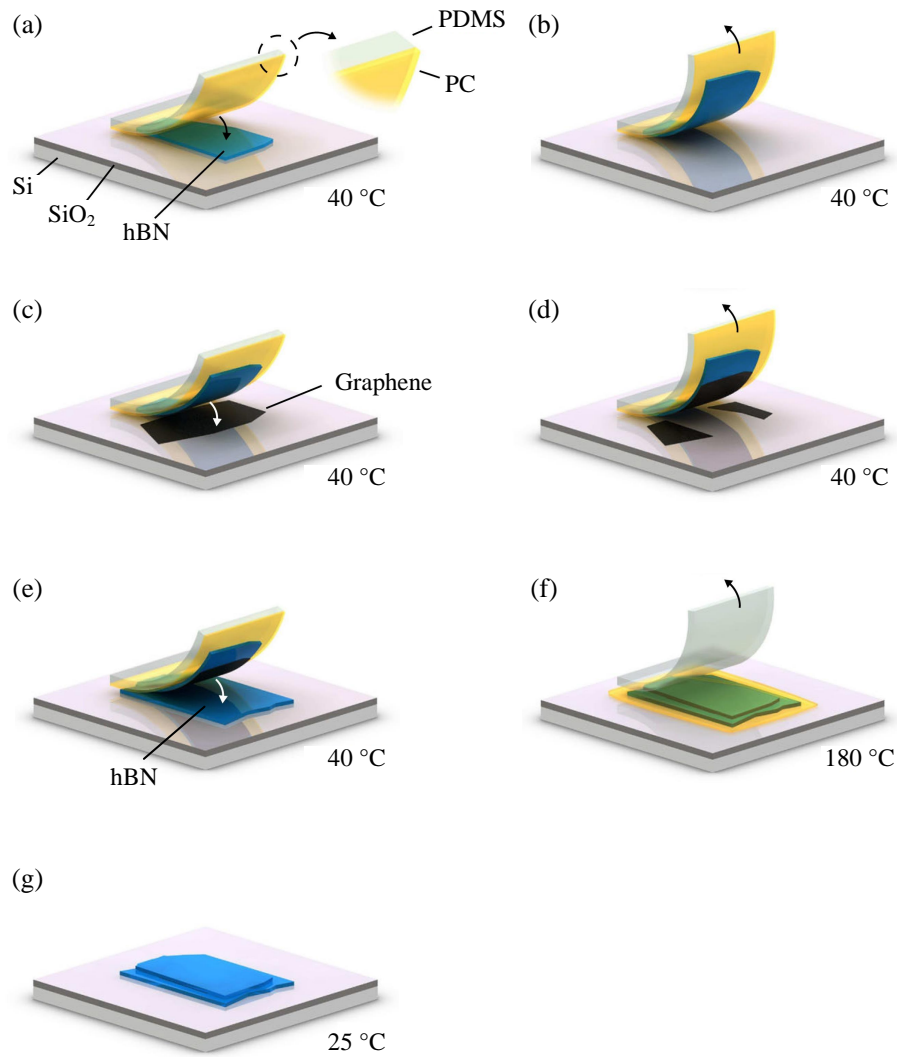


Fig. 6.4 Transfer procedures for hBN/graphene/hBN. (a) A stamp including glass, PDMS and PC is brought into contact with an hBN flake on SiO<sub>2</sub>/Si substrate. (b) hBN is picked up by the stamp. (c) The stamp with hBN is brought into contact with an aligned graphene flake on SiO<sub>2</sub>/Si substrate. (d) Part of graphene is picked up by hBN and stamp. (e) The stamp/hBN/graphene is brought into contact with another hBN flake. (f) PDMS is peeled off and PC with sample adheres to the substrate. (g) PC is dissolved in chloroform. Adapted from [6].

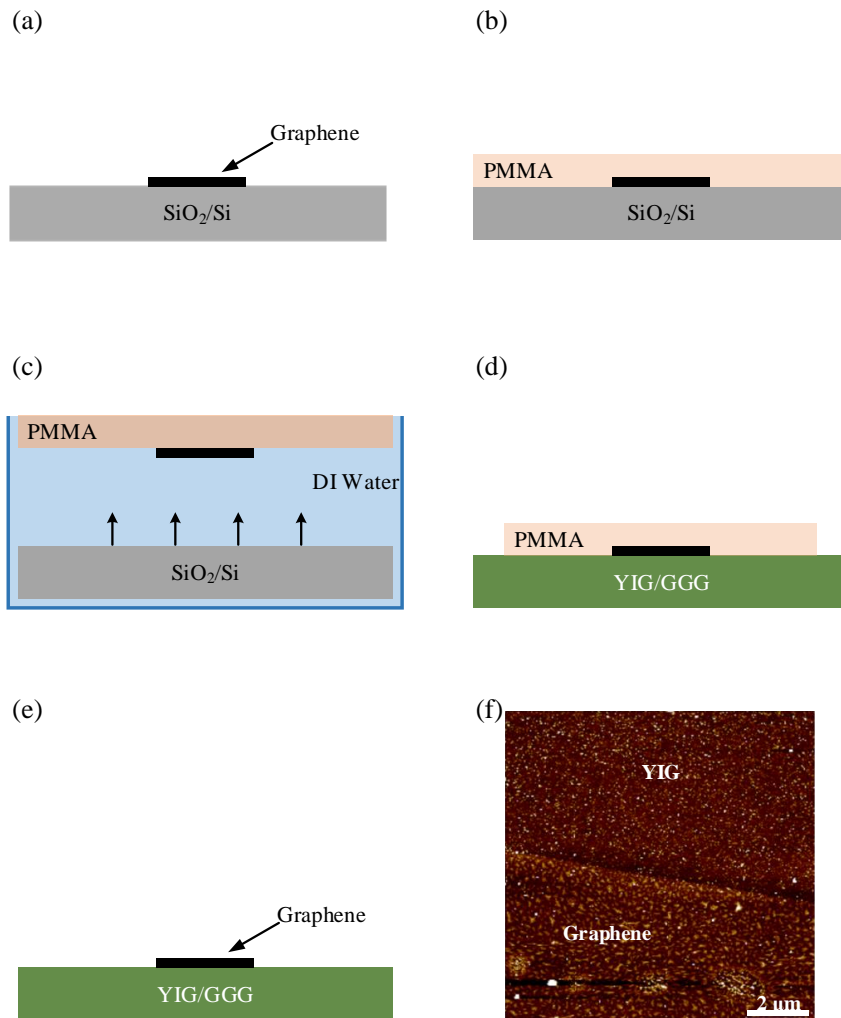


Fig. 6.5 Wet transfer procedures for graphene/YIG device. (a) Exfoliation of graphene on SiO<sub>2</sub>/Si. (b) PMMA is spin-coated onto graphene. (c) The coated sample is immersed in DI water to detach the graphene/PMMA. (d) The sample is transferred onto YIG and left to dry in the air at room temperature. (e) PMMA is dissolved in acetone. (f) High resolution AFM image showing the surface of graphene and YIG after transfer.

This wet transfer is simple and versatile, but left water and PMMA resist on the graphene surface may dope the graphene and decrease its mobility.

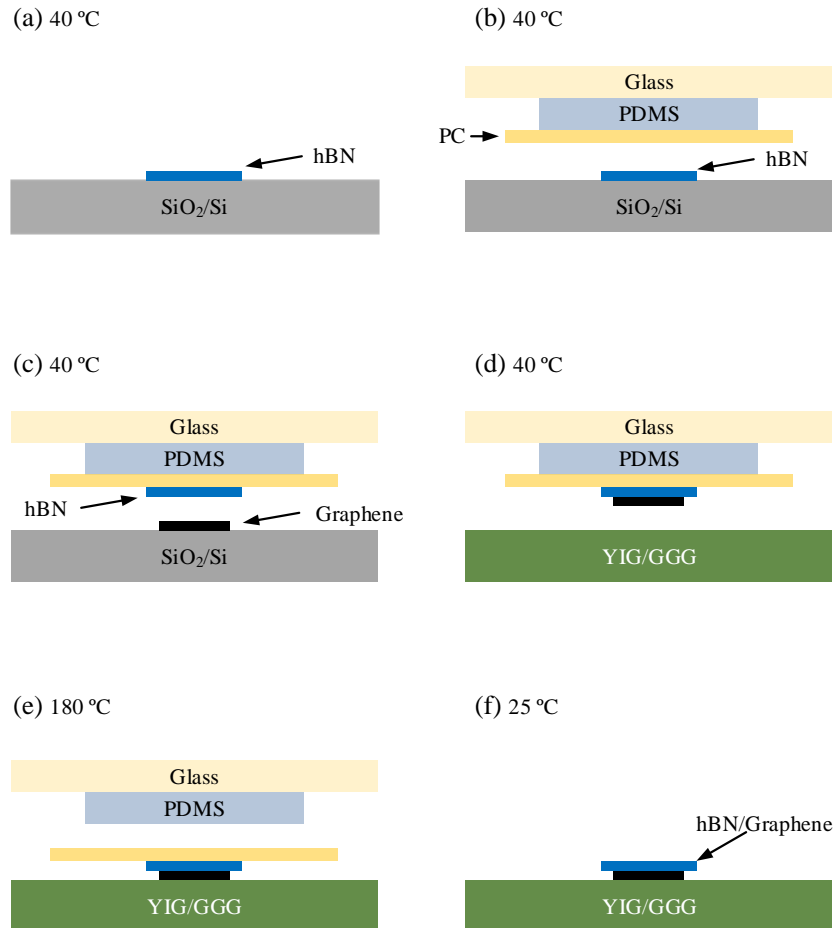


Fig. 6.6 Dry transfer procedures for hBN/graphene/YIG device. (a) Exfoliation of hBN flakes on SiO<sub>2</sub>/Si. (b) A stamp including glass, PDMS and PC is brought into contact with a hBN flake on SiO<sub>2</sub>/Si substrate and the hBN is picked up by the stamp. (c) The stamp with hBN is brought into contact with target graphene flake on SiO<sub>2</sub>/Si substrate. (d) The stamp/hBN picks up the graphene and is brought into contact with YIG/GGG. (e) PDMS is peeled off and the PC with sample adheres to the substrate. (f) PC is dissolved in chloroform.

To preserve the quality of graphene on YIG/GGG, a dry transfer process including hBN encapsulation is used as described in Figure 6.6. Suitable size and defect-free graphene flakes on SiO<sub>2</sub>/Si are selected using an optical microscope in combination with Raman spectroscopy and AFM. A stamp as described above is prepared for the transfer process. Then the target flake is picked up by the stamp using a transfer system including a micro-manipulator, a hot plate and an optical microscope. Under microscope, the target graphene flake is aligned with

the preferred position on the YIG/GGG substrate. When the stamp touches the substrate, the temperature of hot plate is set at around 180 °C to melt PC film. When the stamp is lifted, the graphene/PC film is detached from the PDMS on the stamp. The sample is immersed in chloroform to remove the PC film. Although dry transfer method provides a cleaner interface between two-dimensional materials than the wet transfer method, adsorbates can still be trapped in some regions [160].

## 6.5 Graphene-based Hall bar fabrication

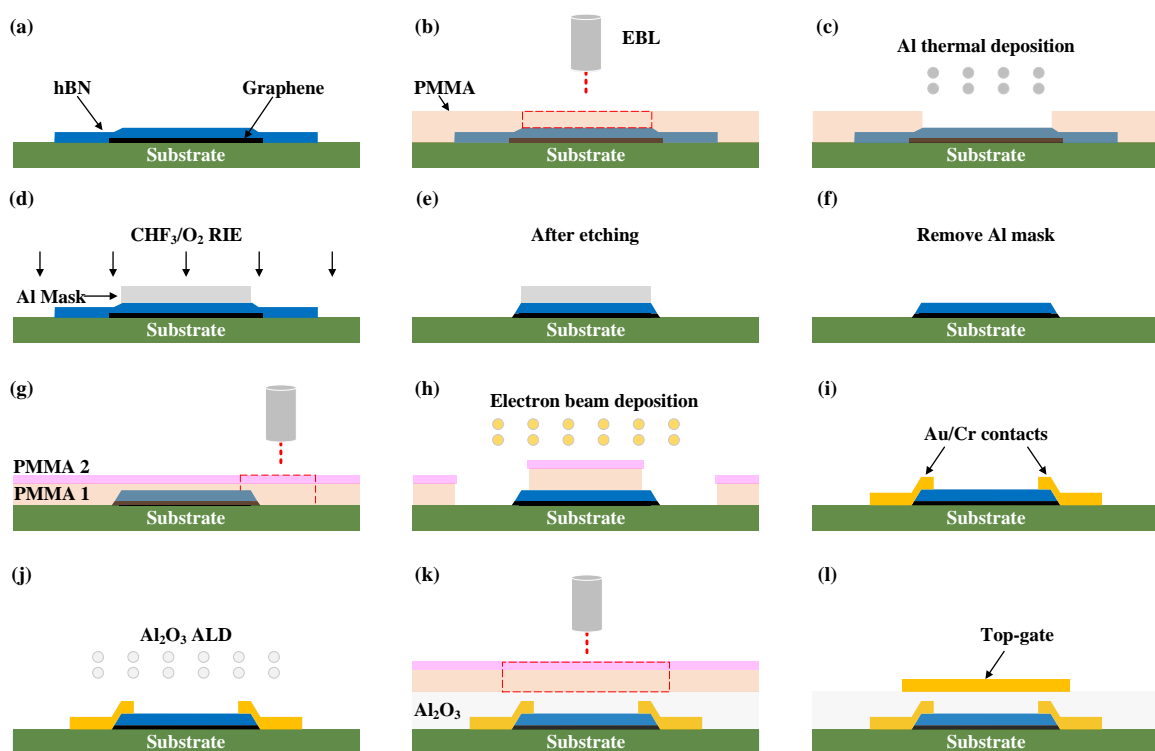


Fig. 6.7 Schematic diagrams showing Hall bar fabrication process.

For all transport measurements, samples are patterned into Hall bars by electron beam lithography (EBL, Nanobeam Ltd) and metal deposition. Detailed procedures are described as following and shown in Figure 6.7.

### 6.5.1 Charging effects on insulating substrate

Electron charging problem appears in the EBL on insulating substrates, which distorts the patterns. To reduce this effect, a conductive charge dissipation layer of 5 nm Au is deposited

by thermal evaporation on the PMMA resist to conduct electrons away from the writing area (Figure 6.8). After the EBL writing, thin Au layer can be wet-etched with a potassium iodide/iodine solution.

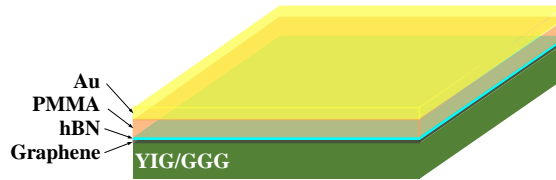


Fig. 6.8 Schematic diagrams of Au charge dissipation layer.

### 6.5.2 Hall bar etching

The first step of fabrication is to shape the stacked two-dimensional materials into Hall bar and expose the graphene edges for side-contact deposition. Samples are encapsulated with hBN, which can be etched by a mixture of  $\text{CHF}_3$  and  $\text{O}_2$ . The standard mask for etching is made of PMMA, but which can be etched with the same recipe at a faster etching rate than hBN. Therefore a 30-nm-thick Al metal mask layer is fabricated by EBL, and is deposited by thermal evaporator [Figures 6.7(b)-(c)]. The hBN/graphene stack is shaped into Hall bar using reactive ion etcher (RIE) with a forward radio frequency power of 60 W, pressure of 10 mTorr, and a 40 sccm flow of  $\text{CHF}_3$  and a 6 sccm flow of  $\text{O}_2$ . The etching rate is  $0.5 \text{ nm s}^{-1}$ . The Al mask can be wet-etched by AZ 326 MIF developer [Figure 6.7(f)].

### 6.5.3 Side-contact deposition

A double-layer PMMA resist (PMMA 495K A6 and 950K A2) is used to pattern the contacts on the edge of graphene with EBL [Figure 6.7(g)]. 10-nm-thick Cr and 70-nm-thick Au films are deposited by electron beam evaporation to define contacts [Figure 6.7(h)]. Upon evaporation, the metal conformally coats both hBN surface and graphene edge, resulting in a good contact with graphene [Figure 6.7(i)].

### 6.5.4 Top-gate dielectric layer and contacts fabrication

Due to the side-contact configuration, the encapsulated hBN layer can not be directly used as a top-gate dielectric layer and it requires to transfer another hBN layer to cover all the side-contacts. Therefore the dielectric layer for the top-gate uses  $\text{AlOx}$  which is prepared by atomic layer deposition (ALD) with trimethylaluminum and  $\text{H}_2\text{O}$  as precursors at  $120^\circ\text{C}$ .

AlO<sub>x</sub> is deposited as 40-nm-thick in order to achieve a uniform and continuous thin film without any defects. The top-gate contacts are prepared by electron beam evaporator of 10-nm-thick Cr and 70-nm-thick Au [Figures 6.7(k)-(l)].

## 6.6 Measurement setup

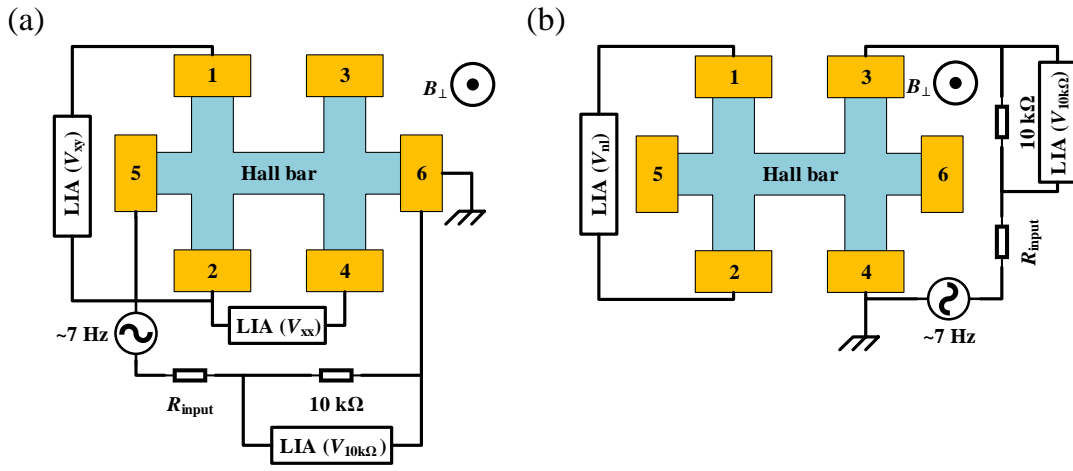


Fig. 6.9 Transport measurement configurations: (a) local and (b) nonlocal measurement setups.  $B_{\perp}$  is an out-of-plane magnetic field. LIA represents a lock-in amplifier.

Transport measurements are performed in a low-temperature system using lock-in amplifiers at  $\sim 7$  Hz with a low excitation current ( $< 100$  nA) as a function of magnetic field, gate voltage and temperature. A series resistance of  $R_{\text{input}}$  (1 or 100 M $\Omega$ ) is introduced to maintain a constant current condition confirmed by the signal from the lock-in amplifier which measures the current through a 10 k $\Omega$  series resistor.

For the local measurements [Figure 6.9(a)], a current  $I$  is applied between contacts, for example, 5 and 6, and the measured voltage between the electrodes (1 and 2) is Hall voltage ( $V_{xy}$ ) and between the electrodes (2 and 4) is longitudinal voltage ( $V_{xx}$ ). Then  $\rho_{xx}$  is given by  $V_{xx}/I$  divided by the geometrical factor,  $L/W$ . The Hall resistivity  $\rho_{xy}$  is calculated by  $\rho_{xy} = V_{xy}/I$ .

For the nonlocal measurements [Figure 6.9(b)], a current  $I$  is applied between the electrodes (3 and 4), the measured voltage between the electrodes (1 and 2) is nonlocal voltage ( $V_{nl}$ ) and is often converted to resistance by dividing the injection current ( $R_{nl} = V_{nl}/I$ ).

Low temperature transport measurements in applied magnetic fields are performed in a Lakeshore probe station and an Oxford Instruments Heliox cryostat. Lakeshore probe station

can provide temperature of 9 K-400 K and out-of-plane magnetic field of up to 2.5 T. Heliox cryostat can provide temperature of 2.7 K - 300 K and rotating magnetic field of up to 12 T.

## **6.7 Summary**

Mechanical exfoliation of graphene and hBN flakes are achieved. A dry transfer method with multi-layer heterostructure and crystal alignment has been developed. With the help of hBN encapsulation, graphene doesn't show structural defects and exhibits low doping. A metal mask is used to shape the heterostructure and side-contacts are fabricated for the device. Transport measurements are performed with lock-in amplifiers to achieve a high signal-to-noise ratio.



# Chapter 7

## Fabrication of thin film YIG on GGG

Yttrium iron garnet (YIG) is chosen as the magnetic substrate for graphene because it is electrically insulating with a Curie temperature above room temperature (550 K) and is chemically stable in atmospheric conditions. YIG films can be fabricated by liquid phase epitaxy, pulsed laser deposition (PLD), and radio frequency magnetron sputtering [161–164]. Liquid phase epitaxy is suitable for the growth of micron-thick films [165, 166], while PLD and radio frequency magnetron sputtering are for the deposition of submicron-thick films.

Here PLD method is selected to grow YIG thin film on gadolinium gallium garnet (GGG) substrate for following reasons: (1) the setup of PLD is relatively simple while the quality of the film is high; (2) PLD system can operate under ambient gases with relatively high growth rate, which is important in oxide material growth. And the layer-by-layer growth of YIG on GGG substrate by PLD with high laser repetition rate has been reported [167]. This chapter introduces the basic process of PLD, and presents experimental results of high quality YIG films with optimized growth parameters.

### 7.1 Substrate selection and preparation

GGG is paramagnetic and used as the substrate for the epitaxial growth of rare earth iron garnet films such as YIG. Because it is one of the most perfect artificially made crystals with extremely few defects (less than one defect per  $\text{cm}^2$ ). The lattice constants of GGG are a function of composition which depend on the factors that influence  $\text{Ga}_2\text{O}_3$  loss from the melt [168], i.e. 12.376 Å from flux-grown crystals and 12.383 Å from Czochralski-grown crystals [169]. Bulk GGG and YIG have the same garnet crystal structure (space group  $Ia\bar{3}d$ ) and matched lattice parameters, which enable the growth of high quality and defect-free unstressed films. The band gap for pure GGG is more than 5 eV [170] and the electrical resistivity is  $10^{14} \Omega \text{ m}$  [171].

Commercial (110) and (111)-oriented GGG substrates (MTI Corporation) are used for YIG growth. GGG substrate is cleaned in DI water, acetone and IPA for 15 minutes respectively by ultrasonic cleaner. Then it is annealed in oxygen at 1000 °C for 8 hours with a flow rate of 100 cm<sup>3</sup> min<sup>-1</sup> in order to have high crystallinity and flat surface, which are essential in epitaxial growth. Because the high temperature annealing in oxygen can effectively reduce oxygen vacancies and improve the crystalline condition on the surface.

## 7.2 Pulsed laser deposition

PLD belongs to the high vacuum physical vapor deposition technique. The target material with complex components can be ablated by the laser and deposited stoichiometrically on the substrates. Therefore the PLD has been widely used in the deposition of complex compounds, such as garnets, ferrites and superconductor materials. Figure 7.1 shows a schematic diagram of the PLD system, which has a pulsed laser source (248 nm KrF), a high vacuum chamber, a rotating target, and a substrate holder with a built-in heater. The pulsed laser beam is reflected and converged by a series of mirrors and lenses, and then strikes on the target inside the chamber.

In general, PLD process can be divided into the following four stages and each of them is important for the crystallinity, uniformity and stoichiometry of the film: (1) creation of target material plasma by laser ablation; (2) dynamic evolution of the plasma plume, which is made of electrons, ions, evaporated atoms, molecules and clusters; (3) deposition of the material plume onto the substrate; (4) nucleation and formation of the thin films on the substrates [172].

Thin film by PLD has atomically flat surface, which is good for interface related research. However, it has been difficult to fabricate thin films (< 1 μm) while keeping the bulk properties ( $T_c$ , magnetization and magnetic anisotropy). The film quality depends on the deposition and post-deposition annealing parameters. A layer-by-layer growth method of YIG films with atomically flat surface is optimized to produce bulk-like magnetic properties.

A high density single phase target of YIG (Moltech Inc.) has been prepared by solid state synthesis reaction. The target is placed on a rotation holder to minimize target surface modification. If the laser pulses strike the same position of target too many times, a cone-like structure forms on the surface, leading to a low deposition rate.

GGG substrates are placed on the hot plate and fixed using high temperature silver paste. After loading substrates, the PLD chamber is pumped overnight to reach pressure of  $1.33 \times 10^{-6}$  Pa. Prior to growth, substrates are baked at 500 °C for 20 minutes. During the growth, the substrate temperature is kept at 750 °C with flowing oxygen at 12 Pa. The

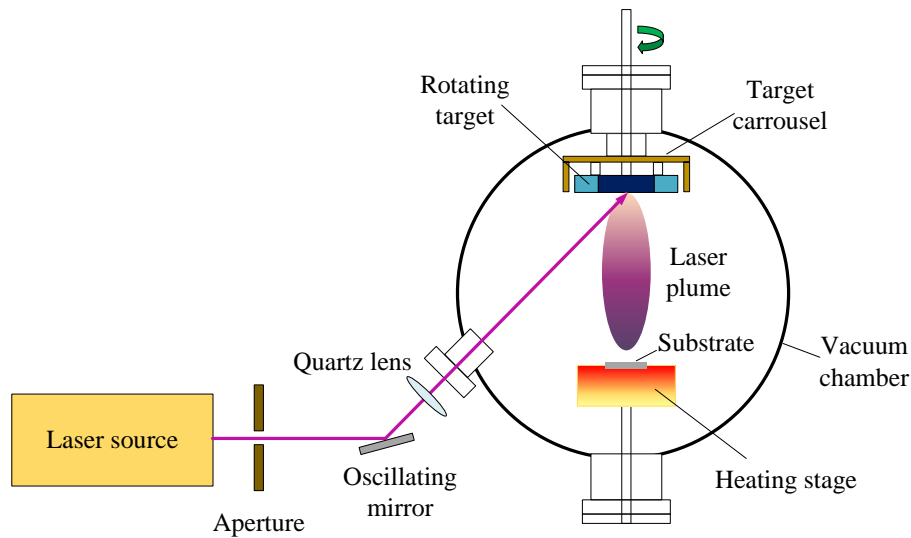


Fig. 7.1 Schematic diagram of the pulsed laser deposition system used in this thesis.

power of KrF laser is set to around 450 mJ per pulse and the repetition rate is 4-7 Hz. A high repetition rate of laser ablation is crucial to deposit as-grown epitaxial films with bulk magnetic properties. After the deposition, samples are post-annealed at 850 °C for two hours with oxygen pressure of 50 Pa and then slowly cooled down with a rate of 5 °C min<sup>-1</sup> to room temperature in the oxygen environment. The substrate temperature is critical to achieve the layer-by-layer growth, since low substrate temperature generally causes polycrystalline or amorphous film, while high temperature leads to a slow deposition rate. The ambient oxygen pressure is important in film stoichiometry, but it is hard to maintain the same level during deposition. When the oxygen pressure is increased, high density of particulates is often induced.

### 7.3 X-ray diffraction

X-ray diffraction (XRD) is used to determine the phase and crystallographic orientation of a material. X-ray is generated when a particle of sufficient kinetic energy rapidly decelerates, the wavelength of which is 0.1-10 nm. In the X-ray diffractometer, X-ray is generated inside a vacuum tube which includes two metal electrodes and a source of electrons. High velocity electrons are released from a hot cathode and then collide against the anode (a metallic target) to generate X-ray.

The lattice spacing in a crystalline sample usually is in the range of the wavelength of X-ray. Then the crystal lattice can be regarded as a diffraction grating for the incident X-ray

beam, resulting constructive interference between the diffracted X-rays, which should satisfy Bragg's Law [173],

$$n\lambda_x = 2d\sin(\beta), \quad (7.1)$$

where  $n$  is an integer number,  $\lambda_x$  is the wavelength of the X-ray,  $d$  is the distance between two adjacent crystallographic planes and  $\beta$  is the angle between the incident X-ray beam and the crystallographic plane.

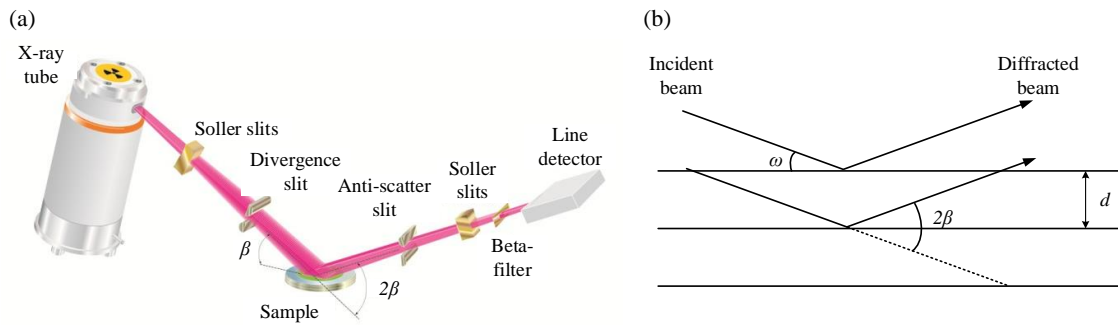


Fig. 7.2 (a) Schematic illustration of XRD setup. Adapted from [174]. (b) Schematic illustration of Bragg's law.

The X-ray diffractometer has five main parts: the X-ray tube, the primary optics including a divergence slit, the sample stage, the secondary optics and a detector with specific sensitivity to the wavelength used in the system [Figure 7.2(a)]. Two different XRD scan modes are typically performed on the sample:  $2\beta - \omega$  and  $\omega$  scans.  $\omega$  is the angle between the incident beam and the sample surface [Figure 7.2(b)] and the diffracted beam angle measured with respect to the incident beam direction is denoted as  $2\beta$ . These two scans are usually measured together, since they provide complimentary structural information about the sample [175].

In a  $2\beta - \omega$  scan mode, the detector angle ( $2\beta$ ) is changing over a certain range with a simultaneous rotation of the  $\omega$ . This scan mode probes along a crystallographic direction perpendicular to the atomic plane. The change of the  $2\beta$  position of a certain diffraction peak relates to the presence of strain in the sample. If there are additional diffraction peaks than those expected during scan, it indicates the presence of impurity phases [175].

In a  $\omega$  scan mode, the detector position is at a fixed angle ( $2\beta$ ) and the sample is rotated to vary the  $\omega$ . This scan is sensitive to the defects in the sample and its crystallographic orientation. For a single phase material, the  $\omega$  scan gives a very narrow peak, while for a sample with a completely random grain orientation, it shows wider peaks because there are many grains which can provide Bragg reflections along the  $\omega$  scan [175].

Low-angle X-ray reflectivity (XRR) is used to determine the thickness and the roughness of thin film, in which X-ray is reflected at the interfaces of materials with different electron

densities and refractive indexes [176, 177]. The total reflectivity amplitude depends on the multiple interface reflections, roughness and thickness, which is recorded in a XRR scan as a function of the  $2\beta$ . The XRR curve shows a series of Laue fringes. From the period of these fringes with a fitting curve by the simulation software, it is able to estimate the thickness and roughness of the thin film.

## 7.4 Vibrating sample magnetometer

Magnetic properties are investigated using a vibrating sample magnetometer (VSM) with a sensitivity of  $10^{-6}$  emu and a maximum applied field of 1 T (Micromag 2900, Princeton Measurement Corporations). The sample can be rotated to measure the dependence of the magnetic field orientation. According to Faraday's law, the voltage ( $V$ ) induced in a coil by a changing magnetic field ( $B$ ) is proportional to the changing rate, i.e.  $V \propto -dB/dt$ . In a VSM, the sample is mounted on a rigid rod which is oscillating at a constant frequency of 10-80 Hz with an amplitude of a few millimeters in an applied magnetic field. Therefore a varying magnetic field is provided and integrating the voltage gives a measurement of  $B$ , then magnetization can be determined.

Two pairs of pickup coils are used to detect magnetic flux cutting. The flux cutting induces an electromotive force signal, which is then compared to a calibration signal recorded on a reference sample and therefore converted into the sample's magnetic moment measured in the applied magnetic field. The presence of two pickup coils, which are wound in series opposition, eliminates any flux noise generated by the electromagnet. Therefore the flux change measured by the two pickup coils coincides with that generated by the vibrating sample cutting the magnetic flux lines across a surface area, and the flux change is proportional to the amplitude of the sample's magnetic moment. The magnetic moment amplitude normalized by the volume is the bulk magnetization, which can be used to compare magnetic properties of samples with different thickness.

## 7.5 Structural characterization of YIG on GGG

With optimized growth parameters, atomically flat thin film YIG of 50-80 nm thickness is obtained. The morphological and structural properties of the YIG films are analyzed using XRD, XRR and AFM. The AFM analysis reveals a smooth surface with a root mean squared roughness ( $R_q$ ) of 0.1-0.2 nm, as shown in Figure 7.3. For (110)-oriented YIG, each monolayer corresponds to 1/4 of unit cell face diagonal length, thus the theoretical height of each monolayer is 0.4375 nm. The step height at the edge of the terrace is measured

as  $\sim 0.44$  nm by AFM, which agrees well with the theoretical atomic layer spacing. The roughness within the terraces is 0.0663 nm, which is much smaller than the step height. But the atomically flat terraces are not observed on (111)-oriented YIG.

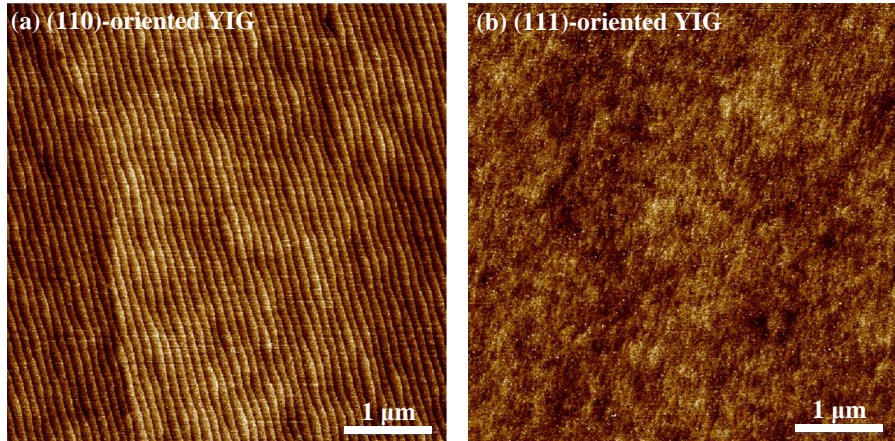


Fig. 7.3 AFM images of YIG thin films. (a) (110)-oriented YIG with roughness of 0.158 nm. (b) (111)-oriented YIG with roughness of 0.179 nm.

XRD measurements have been carried out on the YIG to know the epitaxial relations, and to estimate crystalline quality and film thickness. The YIG film is shown to fully inherit the lattice orientation of the GGG due to the matched lattice constant between bulk YIG and GGG. From XRD measurements, only ( $hh0$ ) or ( $lll$ ) reflection peaks have been observed, respectively, with the clear Laue fringes inversely proportional to the film thickness. Figure 7.4 shows the XRD spectra of YIG on GGG for both (110) and (111) orientations. For the scan angle between  $20^\circ$  and  $90^\circ$ , (220), (440), (660), (880) diffraction peaks can be observed in (110)-oriented YIG and (222), (444), (666) in (111)-oriented YIG. These indicate the YIG film is epitaxially grown along the [110] or [111] direction of the single crystal GGG substrate. Low-angle XRR in Figure 7.5 confirms a typical roughness of 0.14 nm and thickness of 84 nm.

## 7.6 Magnetic properties

The magnetic properties of YIG are assessed through magnetization ( $M$ ) versus magnetic field ( $\mu H$ ) by VSM. As the GGG substrate is a paramagnetic material, the  $M$ - $H$  measurements of YIG/GGG give the full magnetic signals from both the ferrimagnetic YIG and the paramagnetic GGG. The ferrimagnetic material has hysteresis behavior in the  $M$ - $H$  loop, while paramagnetic materials show a linear response. When the thickness of YIG is in the

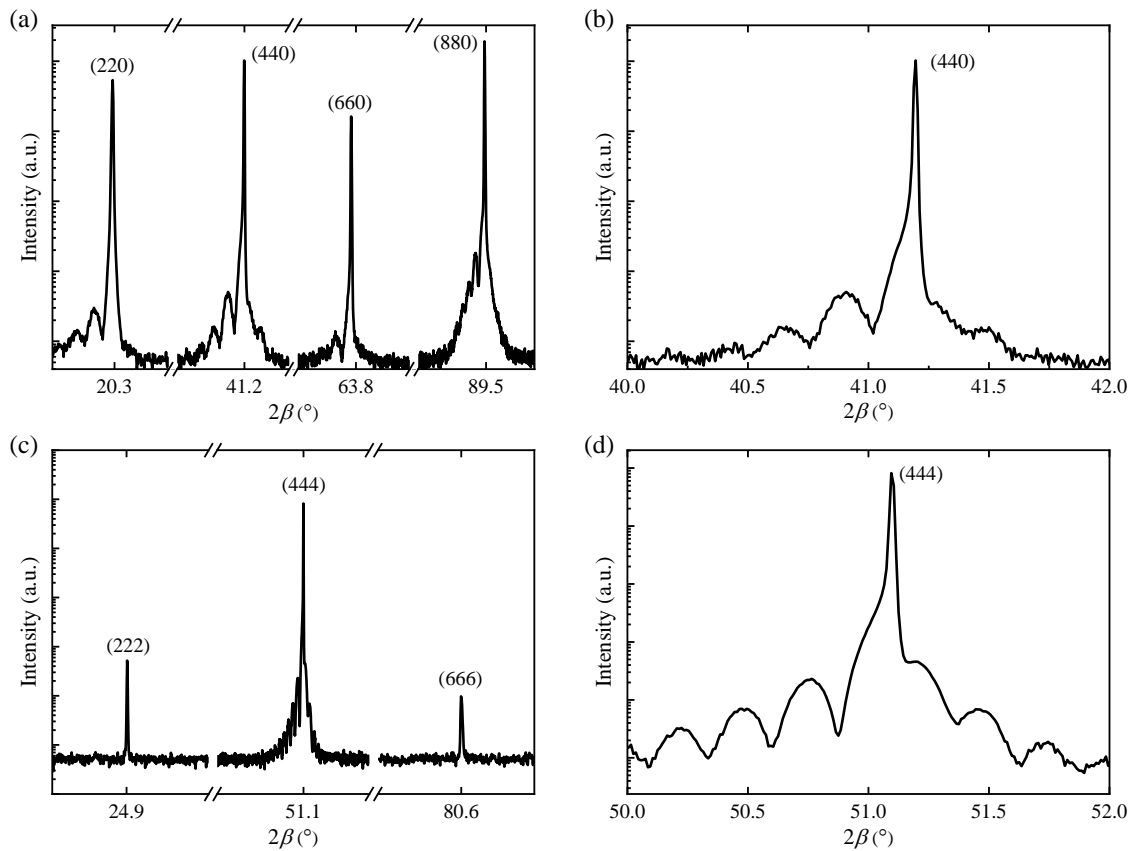


Fig. 7.4 X-ray diffraction spectra demonstrating single phase (a) and (b) (110)-oriented, (c) and (d) (111)-oriented YIG films.

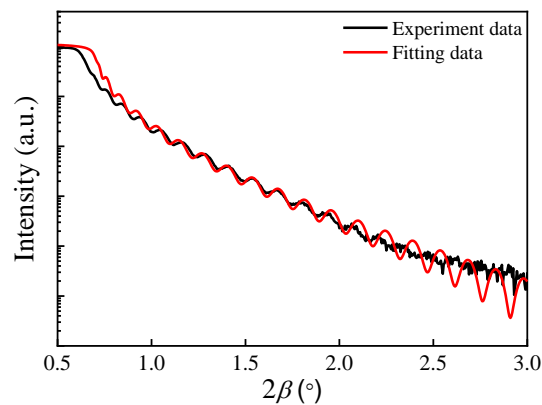


Fig. 7.5 Low angle X-ray reflectometry of (110)-oriented YIG confirming a thickness of 84 nm and roughness of 0.14 nm. The black line is the experiment data, and the red line is the fitting result.

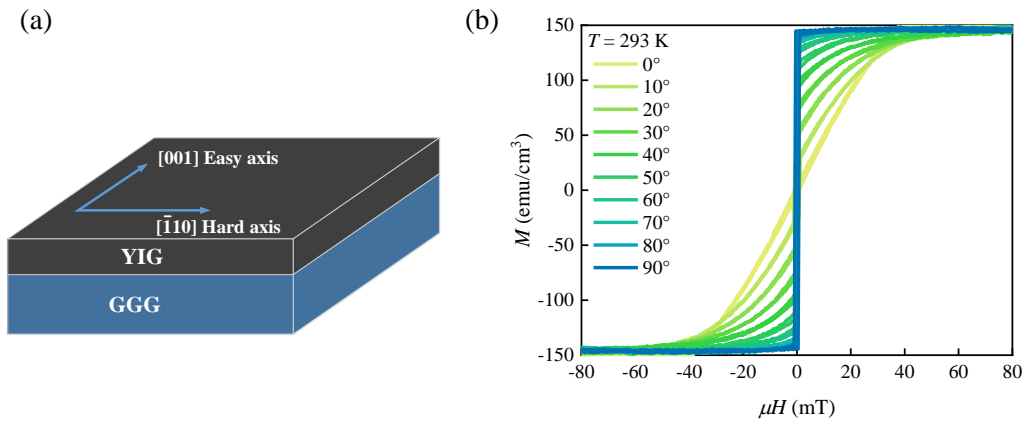


Fig. 7.6 Magnetic properties of YIG. (a) Schematic illustration of in-plane easy and hard axes on (110)-oriented YIG. (b) Magnetization ( $M$ ) versus in-plane magnetic field ( $\mu H$ ) hysteresis loops for different in-plane magnetic field directions. At  $0^\circ$ ,  $\mu H$  is parallel to the hard axis  $[\bar{1}10]$ , while for  $90^\circ$  along the easy axis  $[001]$ .

nanometer scale, the magnetic moment of the YIG film can be as low as  $10^{-5}$  emu if the sample's in-plane dimension is in the millimeter scale. This leads to the measured YIG/GGG  $M$ - $H$  loop having a linear response due to the dominant contribution from the paramagnetic GGG substrate. To obtain the hysteresis loop of the YIG film, the substrate's paramagnetic background needs to be removed by subtracting the slope of the data measured at the high field beyond the  $M_s$  of YIG.

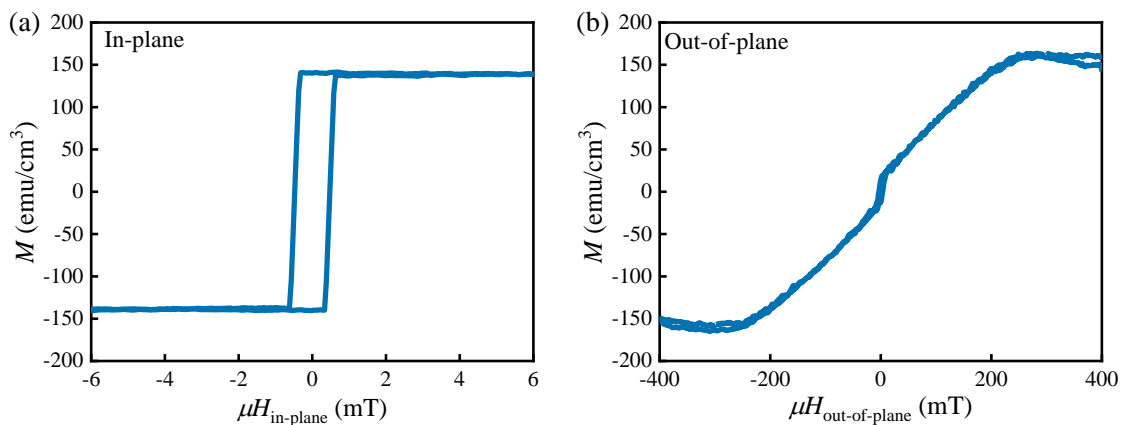


Fig. 7.7 Magnetic hysteresis loops of YIG/GGG. (a) In-plane and (b) out-of-plane magnetic hysteresis loops of (110)-oriented YIG/GGG film at 293 K by VSM. The magnetization has an in-plane easy axis.

The in-plane magnetic anisotropy of (110)-oriented YIG/GGG is investigated by applying the magnetic field parallel to the sample surface with rotating direction relative to one edge of the sample, which is shown in Figure 7.6. The shape of hysteresis loops suggest that the easy axis in-plane is at  $90^\circ$  and the relative hard axis is at  $0^\circ$ , which is strongly anisotropic with coercivity of  $\sim 0.3$  mT and a volume magnetization at saturation of  $144 \text{ emu cm}^{-3}$ . The maximum in-plane (out-of-plane) field required to fully magnetize the YIG is 0.7 mT (200 mT), which is shown in Figure 7.7. The  $M_s$  and  $M_r$  are measured from the hysteresis loops corresponding to each direction, and are plotted in Figure 7.8. Quantitatively,  $M_s$  keeps constant value at all directions, but  $M_r$  is minimized or maximized at  $0^\circ$  or  $90^\circ$  respectively.

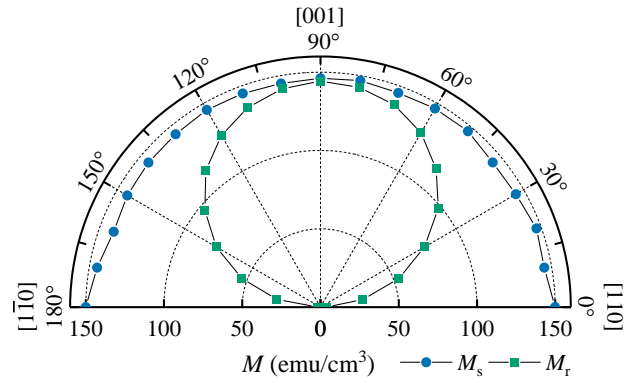


Fig. 7.8 Stoner plot showing constant saturation magnetization ( $M_s$ ) and the variation of the remanent magnetization ( $M_r$ ) versus the angle ( $\gamma$ ) of in-plane applied magnetic field.  $\gamma$  is the angle between the applied magnetic field and  $[\bar{1}10]$  direction. When  $\gamma = 0^\circ$ , the applied magnetic field is parallel to  $[\bar{1}10]$  direction.

## 7.7 Summary

The growth of atomically flat epitaxial YIG thin film depends on the morphology of substrates, target materials and growth parameters. The substrate temperature and laser pulse repetition rate have been optimized to achieve high quality YIG films with a thickness of 50-80 nm, a surface roughness of 0.1-0.2 nm, in-plane anisotropy and bulk-like magnetic properties with a volume magnetization at saturation of  $144 \text{ emu cm}^{-3}$ . The high quality YIG films can be used as the magnetic substrates for the graphene Hall bars fabrication.



# Chapter 8

## Nonlocal transport in graphene

Nonlocal transport in Hall bars refers to the appearance of a voltage across contacts that are far away from the excitation current path. It is associated with non-trivial electronic interactions of the sample, which has been used to probe the dynamics of population imbalance from edge state in the quantum Hall regime [178, 179], spin diffusion [180] and magnetization [181]. The advantage of nonlocal measurement is that it can detect more subtle effects without interference from charge current. There are some proposed theory for the existence of a finite nonlocal resistance ( $R_{nl}$ ) in graphene, including Ohmic effect [182, 183], thermal effect [184, 185], spin current [182, 186, 187], valley Hall effect (VHE) [188], and edge state transport [116, 119, 144].

### 8.1 Spin Hall and Zeeman spin Hall effects

The spin-related transport was first described as spin Hall effect (SHE) [121]. SHE implies that a current can be transferred between a normal metal and a magnetic material due to a spin accumulation with opposite direction at the edge of a magnetic material perpendicular to the charge current [189].

Graphene is promising for spintronics due to its weak intrinsic spin-orbit coupling (SOC) and long spin diffusion length. SOC is a relativistic effect in which an electron changes its spin and angular momentum simultaneously [31, 190]. This coupling strength is strong in heavy ions due to the high average velocity of electrons. Carbon is a light atom, therefore the intrinsic SOC of graphene is weak ( $\sim 10 \mu\text{eV}$  [191]). Rashba SOC in graphene can be enhanced if it is grown on specific substrates due to breaking time reversal symmetry [18, 192]. For example, a 225 meV of Rashba SOC was achieved for graphene grown on Ni [193]. SHE can appear in graphene with strong SOC. Because the SOC can

form a band gap in graphene at the Dirac point (DP), which gives rise to a non-trivial spin Hall resistance (related to the conversion of charge current into spin current).

In an applied magnetic field, the Zeeman field and induced magnetic exchange field in graphene may split the Dirac cone, and generate spin-up electrons and spin-down holes at zeroth Landau level. This is due to graphene's gapless band structure and can be probed by Zeeman spin Hall effect (ZSHE) and its inverse via nonlocal transport measurements. When a charge current flows between the contact 3 and 4 in Figure 6.9(b), due to the Lorentzian force, these electrons and holes propagate in opposite direction, giving rise to a pure spin current perpendicular to the charge current and along the Hall bar channel. The spin current has an inverse effect, inducing a transverse voltage across the detector contacts [104]. The ZSHE depends on the orbital effect (applied out-of-plane magnetic field,  $B_{\perp}$ ) and the Zeeman effect (applied magnetic field  $B = \sqrt{B_{\perp}^2 + B_{\parallel}^2}$ ).  $R_{nl}$  from ZSHE and its inverse can be described as [182, 187, 194],

$$R_{nl} \propto \frac{1}{\rho_{xx}} \left( \frac{\partial \rho_{xy}}{\partial \varepsilon_F} E_Z \right)^2, \quad (8.1)$$

where  $\varepsilon_F$  is the Fermi level. The longitudinal ( $\rho_{xx}$ ) and Hall ( $\rho_{xy}$ ) resistivity depend on  $B_{\perp}$ , and the Zeeman energy ( $E_Z$ ) is proportional to  $B$ .  $R_{nl} \sim 120 \Omega$  in graphene on  $\text{SiO}_2$  was reported due to ZSHE [183] when the device was placed in  $B_{\perp} = 12 \text{ T}$ . A larger  $R_{nl} \sim 800 \Omega$  from ZSHE was observed in graphene on magnetic substrate (EuS) with  $B_{\perp} = 2 \text{ T}$  due to the induced magnetic exchange field from EuS [104].

## 8.2 Valley Hall effect

Topological materials can exhibit Hall-like voltage in the absence of a magnetic field. Placing graphene on hBN with a certain angle can transform graphene into a topological phase [92]. The topological currents originating from two valleys of graphene flow in opposite direction and combine to a long-range charge-neutral current. This effect is called VHE and it arises from a nonzero Berry curvature ( $\Omega$ ) in graphene [188]. Topological currents associated with each valley can propagate over extended distances as long as the intervalley scattering is weak. A nonlocal voltage in zero magnetic field has been detected at distance of  $\sim 10 \mu\text{m}$  away from the excitation current path in graphene superlattice [188].

Berry curvature emerges when inversion symmetry is broken, as both time reversal symmetry and inversion symmetry have different constraints on  $\Omega(k)$ , where  $k$  is the wave-vector. Time reversal symmetry requires that  $\Omega(k) = -\Omega(-k)$ , and inversion symmetry requires  $\Omega(k) = \Omega(-k)$ . When both symmetries are present,  $\Omega(k) = 0$ . Therefore if graphene inversion symmetry is broken, a nonzero Berry curvature occurs and generates transverse

current in the presence of time reversal symmetry [18, 94, 188]. This transverse current results in Hall-like conductivity ( $\sigma_{xy}$ ) given by the sum of Berry fluxes for all occupied states in the Fermi sea [195],

$$\sigma_{xy} = 2 \frac{e^2}{h} \int \frac{d^2k}{2\pi} \Omega(k) f(k), \quad (8.2)$$

where  $f(k)$  is the Fermi function and the factor of two accounts for spin degeneracy. As  $\Omega(k)$  is odd in energy,  $\sigma_{xy}$  has the same sign for both electrons and holes. When the Fermi level is tuned into one of Berry curvature hot spots,  $R_{nl}$  occurs near the DP. Because of time reversal symmetry, both  $\Omega(k)$  and  $\sigma_{xy}$  have opposite signs in valley K and K', which leads to a total valley Hall conductivity of  $\sigma_{VH} = 2\sigma_{xy} = 2e^2/h$ . Nonlocal measurements provide an all-electrical and robust method to probe the bulk valley Hall conductivity. A cubic scaling formula has been proposed for  $R_{nl}$  which originates from the VHE and its inverse [92, 188],

$$R_{nl} \propto (\sigma_{VH})^2 \rho_{xx}^3. \quad (8.3)$$

This scaling has been confirmed experimentally [95, 188, 196–198].

### 8.3 Edge state transport

The observed nonlocal resistance in zero magnetic field ( $B = 0$ ) can come from the edge state transport mechanism. For topological insulator, it has a gapless edge state and a gapped bulk state [188]. When the Fermi level is positioned within the gap, the existence of the time reversal symmetry manifests at the macroscopic level in the form of nonlocal resistance. Weak disorder helps to pin the Fermi level within the gap, creating optimal conditions for the edge state transport which results from the counter-propagating topologically protected helical edge states.

Edge states also exist in graphene, which depend on the type of the edge termination [199]. For the pristine armchair edge (Figure 8.1), it does not support localized edge states without magnetic field [200]. But armchair localized states can appear in the presence of intrinsic spin-orbit coupling and a suitable strain [201]. For the zigzag edge (Figure 8.1), it supports spin-polarized zero-energy edge states, which forms an one-dimensional conducting channel between the two Dirac points [202, 203]. In the presence of a magnetic field (i.e. breaking time reversal symmetry), and a gapped bulk state, the edge states are responsible for the nonlocal transport [116, 119, 144].

In Figure 8.2, it shows a Hall bar geometry with six contacts, where contacts 5 and 6 serve as current source and drain. When unpolarized current is injected through contact 5, the up-spins and down-spins spatially separate in a symmetric way, flowing along the opposite

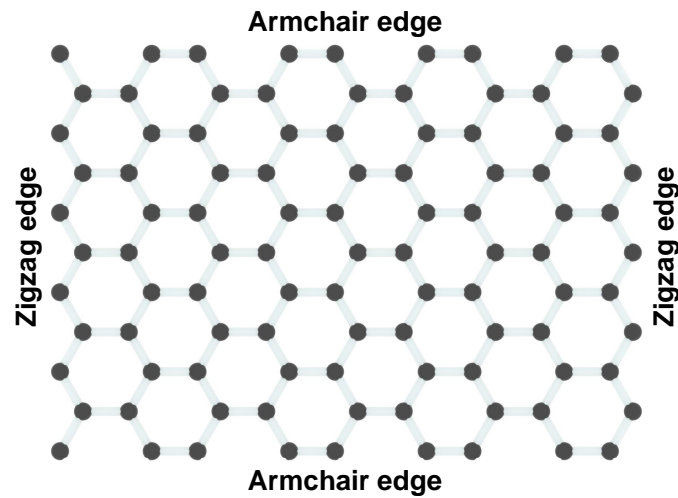


Fig. 8.1 Schematic illustration of a graphene crystal structure with edges. Top and bottom edges are armchair edges, left and right are zigzag edges.

edges of the Hall bar. This can be interpreted as circulating spin current, and described as a spin Hall effect with quantized spin conductance ( $e^2/h$ ). There is no Hall effect from charge carriers between the voltage probes 1 and 2 or 3 and 4.

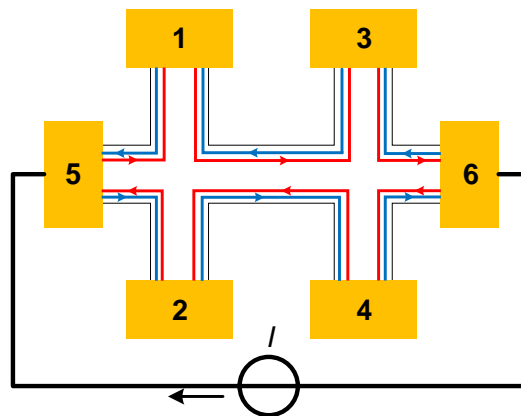


Fig. 8.2 Edge state transport in a Hall bar. Blue and red lines represent edge currents with up and down spins. Contacts 5 and 6 are source and drain, which are used to inject current. Contacts 1, 2, 3 and 4 are voltage probes with full spin mixing.

A general approach based on the Landauer-Büttiker formalism [204] can be used to calculate edge currents for any configurations of Hall bars [144]. In this approach, transport is described by a scattering matrix of transmission coefficients [204], because the edge states act as scattering channels, and the reservoirs supply in-states and absorb out-states. In the quantum Hall regime, it is assumed that the transmission coefficients at the edge

for the different channels equal unity and the backscattering in the sample is suppressed. The non-equilibrium of edge states is important for the occurrence of nonlocal transport over macroscopic distances in magnetic fields [179]. The nonlocal resistance is increased at low temperature, because the non-equilibrium population at the edge is strong due to the suppression of couplings between the edge states.

In addition, contacts play an important role in the edge state transport, which are electron reservoirs incoherently populating edge state channels. An ideal contact is considered to cause no reflection of edge states, meaning that both edge state channels are populated with equal probability by injecting spin-up and spin-down electrons [205]. However, contacts which have high contact resistances partially reflect edge states.

## 8.4 Ohmic contribution

The major extrinsic factor for  $R_{nl}$  is the Ohmic effect [182], which is proportional to the longitudinal resistance ( $R_{xx}$ ) and exists in  $B = 0$ . For a Hall bar [Figure 6.9(b)], the finite length/width ratio ( $L/W$ ) of the channel leads to a detectable voltage across contacts 1 and 2 when a current flows across contacts 3 and 4.  $R_{nl,\Omega}$  is defined as the Ohmic contribution to the  $R_{nl}$ , and is calculated according to the van der Pauw formula and Laplace equation [182] when  $L \geq W$ ,

$$R_{nl,\Omega} = \frac{W}{\pi L} R_{xx} \ln \left[ \frac{\cosh(\pi L/W) + 1}{\cosh(\pi L/W) - 1} \right], \quad (8.4)$$

where  $L$  and  $W$  are the channel length and width. If  $L \gg W$ , Equation (8.4) is simplified as,

$$R_{nl} \approx \frac{4}{\pi} \rho_{xx} e^{-\pi L/W}. \quad (8.5)$$

For a typical Hall bar device of hBN/graphene/YIG,  $L/W = 2.75$  and  $R_{xx} = 9.8 \text{ k}\Omega$ , and from Equation (8.4),  $R_{nl,\Omega} \approx 1 \text{ }\Omega$ , which is two orders of magnitude smaller than the measured  $R_{nl}$  (Figure 8.3). Furthermore,  $R_{nl}$  is sharper than  $R_{xx}$  when gate voltage approaches the DP ( $V_D$ ). Therefore  $R_{nl}$  is not simply proportional to  $R_{xx}$  in zero magnetic field meaning that the nonlocal signal is dominated from other factors than the Ohmic effect.

## 8.5 Thermal contribution

In electrical transport, the charge carriers drift under an applied electric field and result in charge current. However, a temperature gradient can also drive the carriers to diffuse, leading

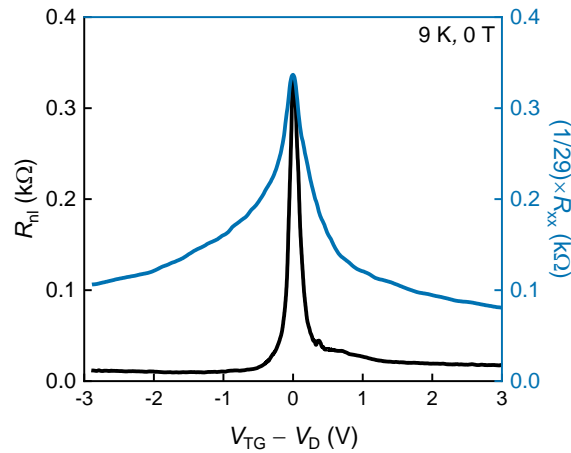


Fig. 8.3 Scaled  $R_{xx}$  and  $R_{nl}$  in zero magnetic field at 9 K.

to a heat current. Thermal contribution to  $R_{nl}$  results from the Nernst effect [184, 206, 207] and its inverse, the Nernst-Ettingshausen effect.

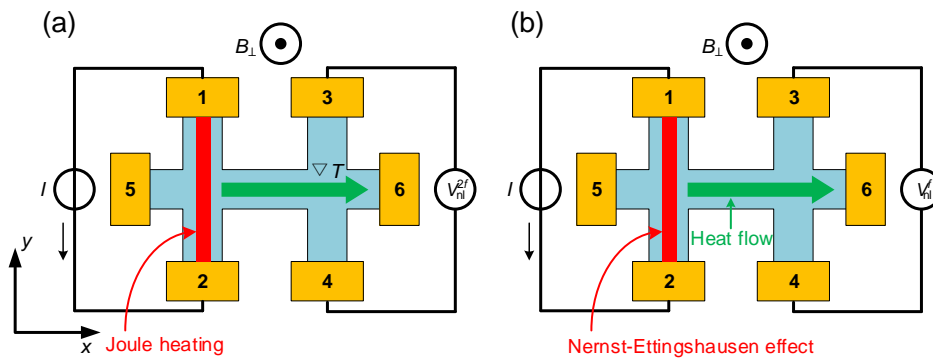


Fig. 8.4 Thermal contribution to  $R_{nl}$ . (a) Joule heating gives rise to second harmonic nonlocal signal. (b) Nernst-Ettingshausen effect gives rise to first harmonic nonlocal signal.

Nernst effect is related to the transverse voltage built up perpendicular to the direction of the temperature gradient along the Hall bar channel in an applied magnetic field. The basic mechanism of Nernst effect is similar to the Hall effect, whereas the flow of the carrier is induced only by temperature gradient. Joule heating at the current injectors would cause heat to flow and pass the detector region shown in Figure 8.4(a). The resulting temperature gradient ( $\nabla T$ ) along the detector region results in a nonlocal voltage across the detector contacts via the Nernst effect, which can be described by the transverse thermopower

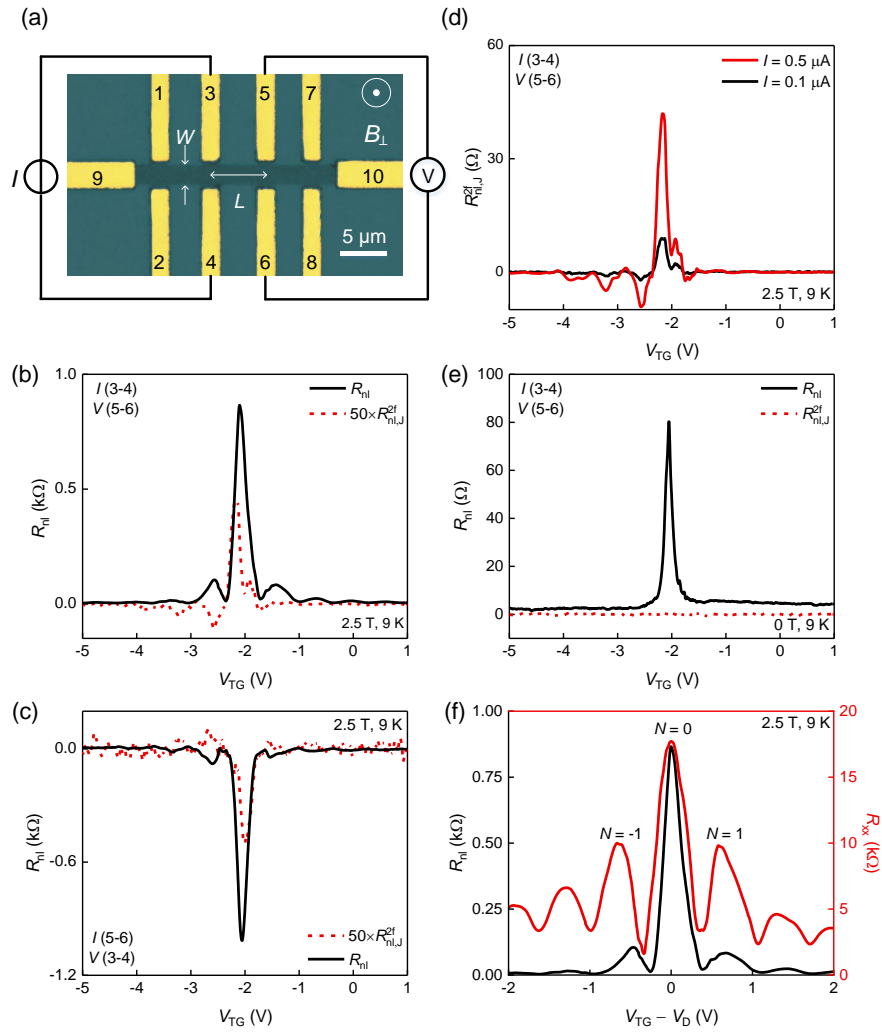


Fig. 8.5 Comparison of first and second harmonic signal of  $R_{nl}$  and  $R_{xx}$  in an hBN/graphene Hall bar on YIG. (a) Optical micrograph of a Hall bar. (b) The second harmonic signal of  $R_{nl}$  (multiplied by 50) and (c)  $R_{nl}$  versus  $V_{TG}$  in  $2.5 \text{ T}$  with reverse nonlocal connections. (d) The second harmonic signal of  $R_{nl}$  versus  $V_{TG}$  with inject current of  $0.1 \mu\text{A}$  and  $0.5 \mu\text{A}$ . (e) Comparison of the first and second harmonic signal of  $R_{nl}$  in  $0 \text{ T}$ . (f) Comparison of  $R_{nl}$  and  $R_{xx}$  with no additional oscillations in  $R_{nl}$  at  $N = \pm 1$  Landau levels, indicating that the Nernst-Ettingshausen effect is negligible.

coefficient,

$$S_{yx} \equiv E_y(\delta T/\delta x)^{-1} \propto V_{nl}(\delta T/\delta x)^{-1}, \delta T/\delta x \propto Q_J = I^2 R, \quad (8.6)$$

where  $E_y$  is the applied electric field on the  $y$ -direction in Figure 8.4,  $T$  is the temperature,  $V_{nl}$  is the nonlocal voltage,  $Q_J$  is the Joule heating flow,  $I$  is the applied current and  $R$  is the resistance between current injectors. As the temperature gradient is quadratic in applied current, Joule heating contributes to the nonlocal voltage only at the second harmonic of the excitation frequency [184, 206, 207] and does not affect the first harmonic of  $R_{nl}$ . In addition,  $R_{nl,J}^{2f}$  is due to thermal effects and not to spin-related effect, therefore it does not depend on in-plane magnetic field.

In an hBN/graphene Hall bar on YIG shown in Figure 8.5(a) and in 2.5 T,  $R_{nl,J}^{2f}$  is typically two orders of magnitude below the  $R_{nl}$  [Figures 8.5(b)-(c)] and in the range of 8-10  $\Omega$  when  $I = 100$  nA. Figure 8.5(d) shows that  $R_{nl,J}^{2f}$  is proportional to the excitation current and hence low current amplitude ( $< 100$  nA) is chosen to minimize thermal contributions. When the current and voltage probes are switched to reverse the current direction,  $R_{nl,J}^{2f}$  changes sign due to reversal heat flow along the Hall bar [Figures 8.5(b)-(c)]. In zero magnetic field,  $R_{nl,J}^{2f}$  is less than 1  $\Omega$  [Figure 8.5(e)].

Nernst-Ettingshausen effect contributes to the first harmonic nonlocal signal due to the generated heat flow, which can be described as [183, 208],

$$Q_E = S_{yx} T I, \quad (8.7)$$

where heat flow ( $Q_E$ ) is linear in excitation current ( $I$ ) and builds up a temperature gradient along the channel ( $\nabla T \propto Q_E$ ), yielding a transverse Nernst voltage ( $V_{nl,E}^f$ ) in an out-of-plane applied magnetic field ( $B_{\perp}$ ):  $V_{nl,E}^f = S_{yx} \nabla T \propto S_{yx}^2 T I$ . Therefore the resulting nonlocal resistance  $R_{nl,E}^f \propto S_{yx}^2 T$ , and appears at the first harmonic of  $R_{nl}$ .

The maxima of both  $R_{nl,E}$  and  $S_{yx}$  occur at  $N = 0$  Landau level, but  $S_{yx}$  changes sign when the gate voltage locates between adjacent Landau levels or in the centre of a Landau level [104], in which  $R_{nl,E}^f$  should show peaks. Figure 8.5(f) compares the  $R_{nl}$  and  $R_{xx}$  as a function of gate voltage, but  $R_{nl}$  does not show additional peaks except for at the Landau level positions, which demonstrates the Nernst-Ettingshausen effect contribution is negligible.

## 8.6 Summary

Nonlocal measurement is a powerful tool for investigating electronic properties in graphene. In order to distinguish the extrinsic and intrinsic origins of nonlocal resistance, both the first and second harmonic nonlocal voltages are measured. In zero magnetic field, spin Hall

---

effect, edge state transport or Ohmic effect could contribute to  $R_{nl}$ . When a magnetic field is applied, Zeeman spin Hall effect and thermal effects could appear as well.



# Chapter 9

## Zeroth Landau level in graphene/hBN superlattice

Graphene has spectacular electronic properties, but gapless band structure limits the development of high performance graphene-based devices. Graphene/hBN van der Waals heterostructure not only shows improved electrical properties for devices, such as suppressed charge inhomogeneity, reduced ripples and high mobility [86, 87], but also provide unique opportunities for band structure engineering by a periodic potential [209, 210]. The induced potential is from the lattice mismatch and crystal orientation, which could lead to a gap opening at the Dirac point (DP) [91, 94, 188], topological current [188] and the emergence of secondary Dirac points (SDPs) [19, 211].

### 9.1 Introduction

Graphene valley-dependent electronics was proposed a decade ago [17, 18], but inversion symmetry in graphene makes it challenging to apply the valley degree of freedom in electronics. However, minimal lattice mismatch (1.8%) [49] between graphene and hBN results in a rotation-dependent moiré pattern, which leads to weak periodic potentials [87] and broken inversion symmetry [91] in graphene. In atomically aligned graphene/hBN, a band gap at the primary DP ( $V_D$ ) [91, 94, 188] and SDPs are stabilized at energy relating to the moiré wavelength [19, 91].

Recently,  $R_{\text{nl}}$  at the DP and SDPs in aligned graphene/hBN in zero magnetic field have been interpreted as being related to a finite Berry curvature, which leads to the valley Hall effect (VHE) due to a coupling between the valley degree of freedom and the electron orbital motion [18, 95, 188, 212]. The improved electronic property of graphene on hBN

weakens intervalley scattering, and enables long-range topological valley currents [95, 188]. In Ref. [188],  $R_{nl}$  was  $\sim 1$  k $\Omega$  at the DP in the encapsulated (i.e. hBN/graphene/hBN) and non-encapsulated (i.e. hBN/graphene/SiO<sub>2</sub>) Hall bars. However, the longitudinal resistivity in the encapsulated Hall bars showed metallic-like behavior despite the presence of a band gap opening at the DP. The opening of the band gap could be due to inversion asymmetric perturbation potential [91]. In Ref. [95],  $R_{nl}$  reached the quantum-limited value at the SDP in a ballistic hBN/graphene/hBN Hall bar, albeit with an anomalously low value of  $R_{nl}$  at the DP, similar to Ref. [188]. In the Hall bars reported in Ref. [188], the top hBN layer was misaligned with respect to the graphene by 10°, whilst in Ref. [95] the top and bottom hBN layer were aligned to graphene. Here fully encapsulated hBN/graphene/hBN superlattice Hall bars with designed misalignments are investigated by nonlocal transport measurements near the DP where  $R_{nl}$  approaches  $h/2e^2$  in zero magnetic field below 20 K in contrast to Ref. [95].

## 9.2 Device fabrication

hBN/graphene/hBN Hall bars are fabricated by van der Waals assembly with side-contacts as shown in Figure 9.1 (details are discussed in Chapter 6). The relative rotation angle  $\varphi$  ( $\varphi > 0^\circ$  when rotation is clockwise) between hBN and graphene is determined using a transfer system with a rotating stage under an optical microscope with an accuracy of better than 1.5°. Three typical devices denoted as I, II, and III are shown in Figure 9.2. For Device I, the top and bottom hBN layers are 151- and 33-nm-thick respectively with  $\varphi \sim 0^\circ$ . For Device II, the graphene is aligned to the top layer of hBN ( $\varphi \sim 0^\circ$ ) but misaligned ( $\varphi \sim 30^\circ$ ) with respect to the bottom hBN. For Device III, the graphene is aligned with respect to the top ( $\varphi \sim 10^\circ$ ) and bottom ( $\varphi \sim -10^\circ$ ) hBN layers.

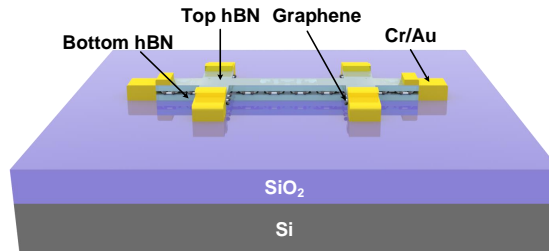


Fig. 9.1 Schematic illustration of an hBN/graphene/hBN Hall bar.

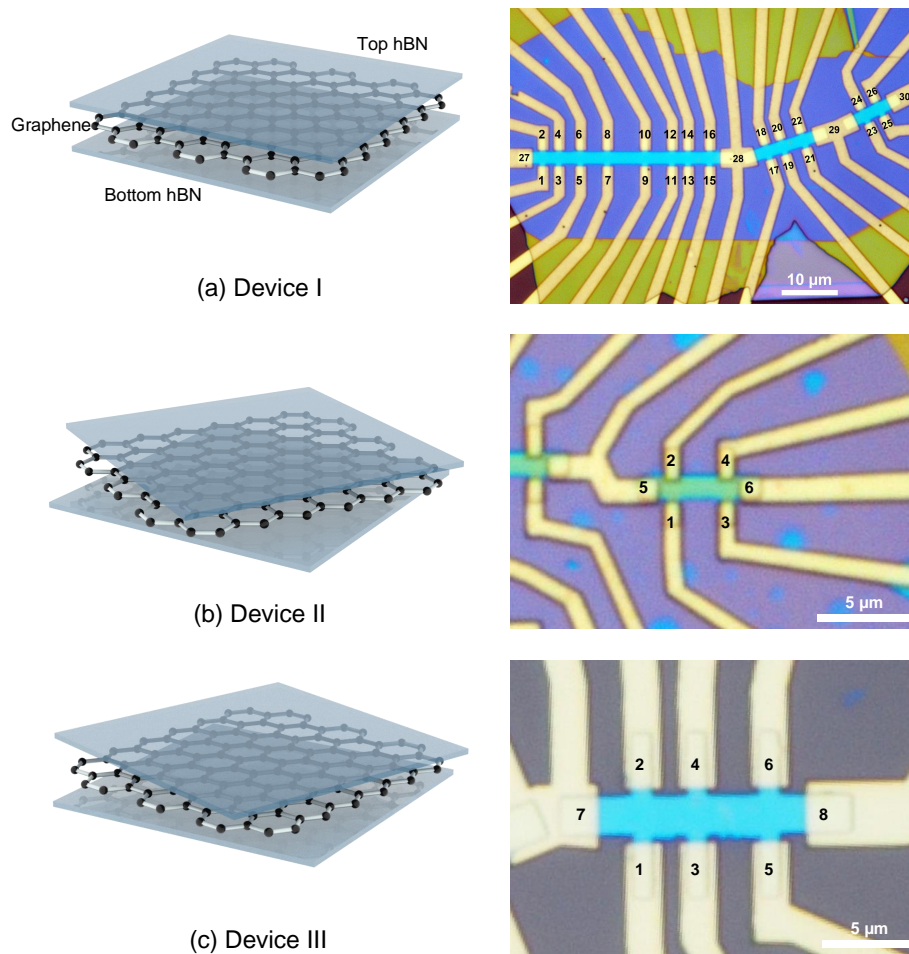


Fig. 9.2 Schematic illustration and optical micrographs of (a) Device I, (b) Device II and (c) Device III.

## 9.3 Device characterization

### 9.3.1 Raman spectroscopy

The transfer of graphene on hBN results in numerous bubbles containing trapped adsorbates (i.e. hydrocarbons), and if present in the active region of devices such bubbles cause significant change of inhomogeneity. To investigate structural and electronic homogeneity of the graphene on hBN, Raman spectroscopy is performed over entire region at 293 K and is recorded using a microscope ( $\times 50$  objective) with 2400 lines/mm grating, 514.5 nm excitation and  $< 300 \mu\text{W}$  laser power. The spectra in Figure 9.3 exhibit the characteristic peak of hBN as well as the G and 2D peaks of graphene. The absence of the D peak ( $1345 \text{ cm}^{-1}$ ) indicates there is no detectable lattice defects in graphene. The positions of the G ( $1580\text{-}1585 \text{ cm}^{-1}$ ) and 2D ( $2686\text{-}2691 \text{ cm}^{-1}$ ) peaks indicate an overall low doping concentration of graphene [213]. Hall bars are fabricated in areas that are free of bubbles and where the full width at half maximum of the 2D peak [FWHM(2D)] is in the range of  $25\text{-}30 \text{ cm}^{-1}$  (Figure 9.4).

hBN has the same lattice structure as graphene with a 1.8% longer lattice constant. The alignment between the graphene and hBN lattices leads to moiré patterns. The moiré wavelength  $\lambda$  is described as,

$$\lambda = \frac{(1 + \delta)a}{\sqrt{2(1 + \delta)(1 - \cos \varphi) + \delta^2}}, \quad (9.1)$$

where  $\delta$  is the lattice mismatch between hBN and graphene, and  $a$  is the graphene lattice constant [49]. Figure 9.5(a) plots the wavelength of the moiré pattern as a function of  $\varphi$  and shows a maximum wavelength of 14 nm. In particular, the 2D peak of graphene is sensitive to  $\varphi$ , and FWHM(2D) is increased by rotating from a misaligned to an aligned position due to the strain distribution with matched periodicity of the moiré potential [214]. Figure 9.5(b) shows the 2D peaks of the different structures investigated: FWHM(2D) of perfect aligned Device I ( $\sim 27 \text{ cm}^{-1}$ ) is larger than Devices II ( $\sim 17 \text{ cm}^{-1}$ ) and III ( $\sim 22 \text{ cm}^{-1}$ ) for which  $\varphi$  is  $30^\circ$  and  $10^\circ$ .

### 9.3.2 Field-effect mobility

The quality of Hall bar devices is characterized through field-effect mobility shown in Figure 9.6: for Device I, it is in the range of  $100,000 - 220,000 \text{ cm}^2 \text{ V}^{-1} \text{ s}^{-1}$  at 9 K, for Device II it is in the range of  $200,000 - 350,000 \text{ cm}^2 \text{ V}^{-1} \text{ s}^{-1}$  at 9 K, and for Device III, it is

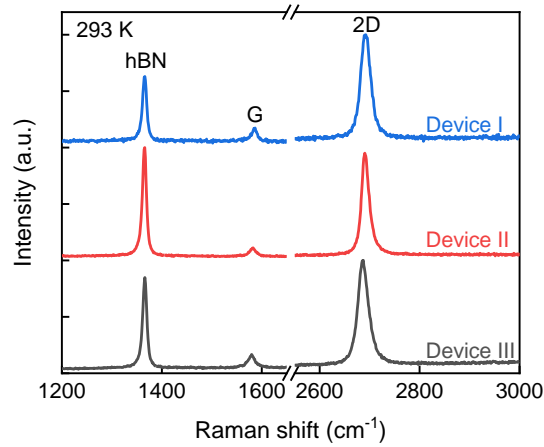


Fig. 9.3 Raman spectra on hBN/graphene/hBN at 293 K.

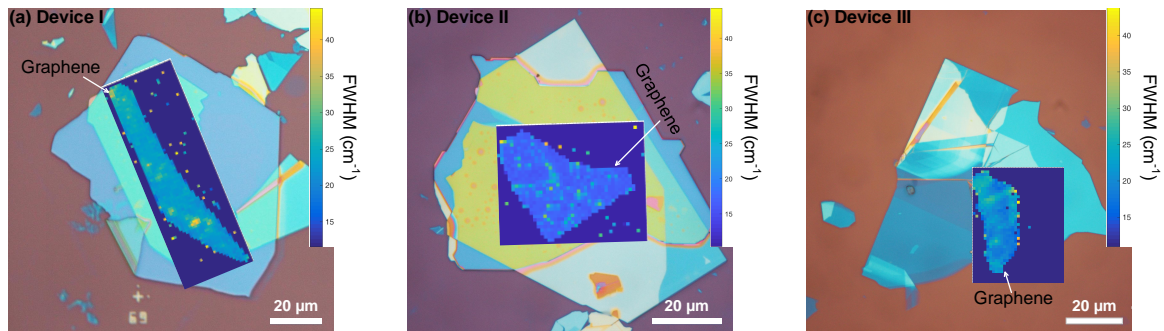


Fig. 9.4 Raman spectra maps (dark blue rectangle region) of hBN/graphene/hBN at 293 K, which are generated from FWHM ( $\text{cm}^{-1}$ ) of the 2D peaks. (a) Device I, (b) Device II and (c) Device III.

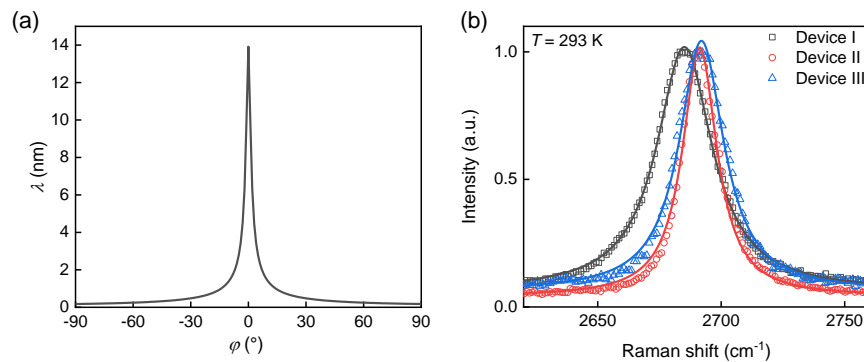


Fig. 9.5 Raman spectra in graphene superlattice. (a) Moiré wavelength as a function of the angle  $\varphi$  between the graphene and hBN lattices. (b) 2D peak positions with Lorentzian fits for Devices I, II and III.

in the range of  $10,000 - 50,000 \text{ cm}^2 \text{ V}^{-1} \text{ s}^{-1}$  at 9 K. The high mobility of devices indicates that defects and charge inhomogeneity are negligible.

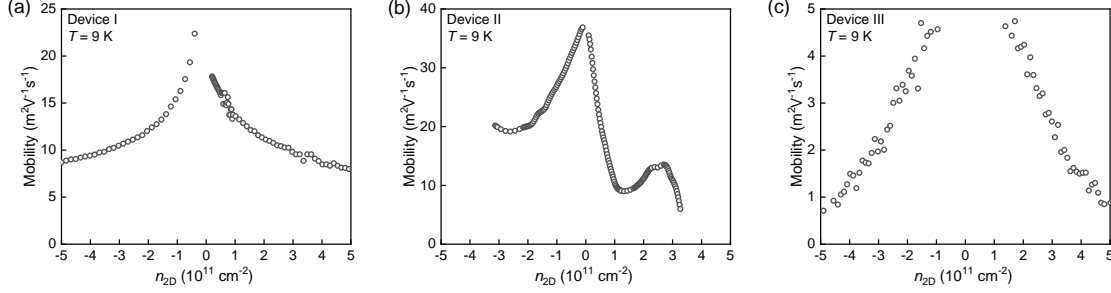


Fig. 9.6 Field-effect mobility of hBN/graphene/hBN Hall bars (labelled).

### 9.3.3 Secondary Dirac point

Graphene aligned with hBN exhibits the moiré pattern, and its density of states is strongly modified [49], which leads to moiré minibands. This spectral reconstruction occurs near the edges of the superlattice Brillouin zone, which is characterized by a SDP energy [19, 49] of

$$|E_{\text{SDP}}| = \sqrt{\pi |n_{2\text{D}}|} v_F \hbar = \frac{2\pi \hbar v_F}{\sqrt{3}\lambda}, \quad (9.2)$$

where  $n_{2\text{D}}$  is the carrier density related to the SDP,  $v_F$  is the Fermi velocity,  $e$  is the electron charge, and  $\hbar$  is Planck's constant divided by  $2\pi$  and  $\lambda$  is the moiré wavelength. To observe moiré minibands in transport measurements, graphene has to be doped so that the Fermi energy reaches the reconstructed part of the spectrum. From Equation (9.2), the position of SDP corresponds to a carrier density of  $4\pi/3\lambda^2$ , and in the case of  $\varphi = 0^\circ$ , a maximum  $\lambda$  (14 nm) yields  $n_{2\text{D}} \approx 2 \times 10^{12} \text{ cm}^{-2}$ . However, misalignment by only  $1^\circ$  decreases  $\lambda$  by a factor of two, and four times larger value of carrier density is required for the Fermi energy to reach the edge of the first superlattice Brillouin zone [49]. In practice, the observation of SDP requires alignment with less than  $1^\circ$ .

Figure 9.7 shows a pronounced peak in  $\rho_{xx}$  for Device I in zero magnetic field at 9 K. Two additional peaks are symmetrically visible on both sides of the DP in the higher carrier density regime. The secondary peak on the hole side ( $V_{\text{TG}} < V_{\text{D}}$ ) is  $\sim 10$  times stronger than that on the electron side ( $V_{\text{TG}} > V_{\text{D}}$ ) due to the p-type doping in graphene. According to Equation (9.2), the  $\lambda$  of Device I is calculated to be  $\sim 10 \text{ nm}$  ( $\varphi < 1^\circ$ ) and for Devices II and III, there are no SDPs within the gate voltage range investigated, indicating that

$\varphi \gg 1^\circ$ . Therefore Device I is in the commensurate state and the other two devices are in the incommensurate states.

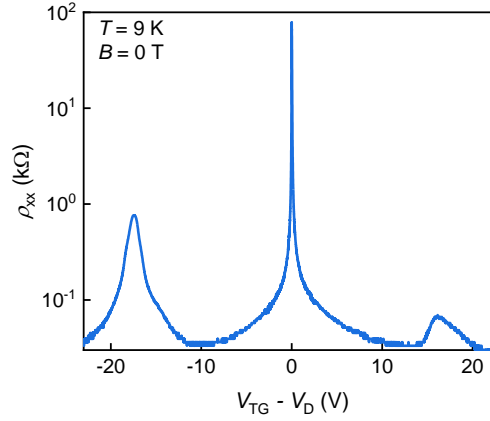


Fig. 9.7 Longitudinal resistivity  $\rho_{xx}$  as a function of gate voltage in Device I at 9 K, which shows pronounced peaks at the primary Dirac point ( $V_{TG} = V_D$ ) and the SDPs ( $V_{TG} - V_D = \pm 17$  V).

### 9.3.4 Mean free path

At all temperatures, diffusive transport occurs at very low carrier density near the DP, because the mean free path ( $L_{mfp}$ ) depends on  $n_{2D}$ , which is calculated by [215]

$$L_{mfp} = \frac{\mu h \sqrt{n_{2D}}}{2e\sqrt{\pi}}, \quad (9.3)$$

where  $h$  is Planck's constant,  $n_{2D}$  is carrier density,  $e$  is electron charge and mobility  $\mu$  can be calculated by Drude formula ( $\sigma = en_{2D}\mu$ ).

In Figure 9.8(a),  $L_{mfp}$  increases with decreasing temperature and saturates at  $2 \mu\text{m}$  below 20 K, which is comparable to the device geometry. Figure 9.8(b) shows  $R_{nl}$  of the Device I as a function of  $n_{2D}$  in zero magnetic field, and in a range of temperature between 15 K and 80 K.  $R_{nl}$  shows negative values for both electron and hole doping up to 60 K, with a distinct minimum in the hole regime near the DP. The negative  $R_{nl}$  shows a temperature dependence and becomes positive with increasing temperature, indicating a transition to the diffusive regime, dominated by electron-phonon scattering. The negative  $R_{nl}$  also indicates a ballistic overshoot of charge carriers from the current injectors into the voltage detectors [89], meaning that the mean free path exceeds the dimension of the device ( $2 \mu\text{m}$ ). All of these results confirm the ballistic character of Device I.

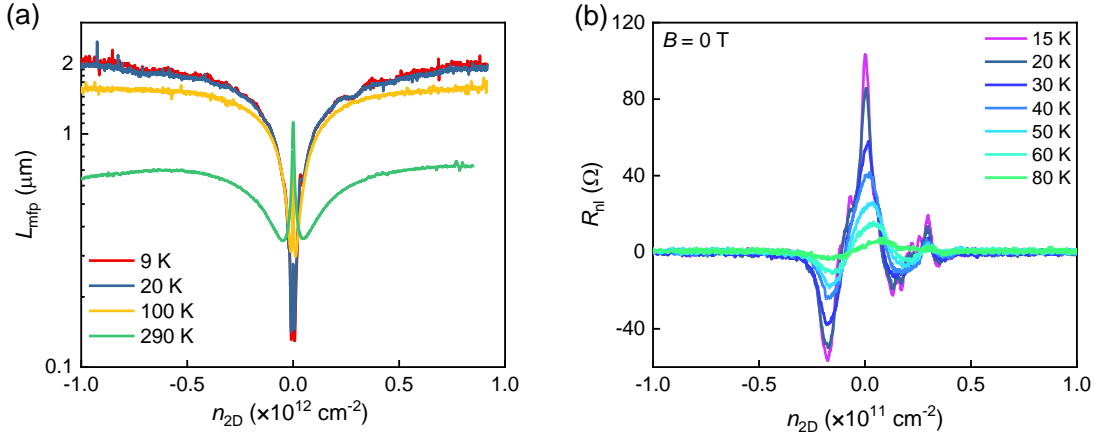


Fig. 9.8 Ballistic character of Device I. (a) Mean free path ( $L_{\text{mfp}}$ ) calculated from the diffusive regime as a function of  $n_{2\text{D}}$  for different temperatures. (b) Negative nonlocal resistance ( $R_{\text{nl}}$ ) measured from 15 K to 80 K in zero magnetic field.

## 9.4 Local transport measurements

### 9.4.1 $\nu = 0$ state in hBN/graphene/hBN

In Figure 9.9, when temperature is decreasing, a  $\nu = 0$  plateau appears in  $\sigma_{xy}$  and a double-peak structure appears in  $\sigma_{xx}$  when the gate voltage is near the DP. Two types of electronic states are observed in Figure 9.9(a): one is the insulating state meaning  $\sigma_{xx}$  decreases at lower temperatures when  $V_{\text{TG}}$  is close to the DP; the other is metallic state in which  $\sigma_{xx}$  increases at lower temperatures. The critical point separating these two regimes is the crossing point of all the curves from different temperatures, where  $\sigma_{xx}$  is independent of temperature indicating the quantum Hall effect transition. When applied magnetic field is increased,  $\sigma_{xy}$  at the DP approaches to a plateau in Figure 9.10(a). In 2.5 T,  $\rho_{xx}$  noticeably exceeds  $h/e^2$ , and a double-peak structure in  $\sigma_{xx}$  appears with  $\sigma_{xy} = 0$  near the DP [Figures 9.10(b)-(c)].

To calculate the band gap observed in the transport measurements, a detailed study of the temperature dependence of  $\rho_{xx}$  in 0 T is performed and shown in Figure 9.11. A bulk gap at the DP in hBN/graphene/hBN occurs due to the electron-electron interaction and broken sublattice symmetry [91, 216]. From the insulating behavior of  $\rho_{xx}$  at the DP, an Arrhenius function  $\sigma_{xx}(T^{-1})$  is used to estimate the band gap and shown in Figure 9.12. The thermally excited transport exhibits two distinct regimes of behavior, separated by a characteristic temperature which is defined as  $T^*$ . For  $T > T^*$ , transport is thermally activated [95] meaning that  $\sigma_{xx,\text{min}} \propto \exp(-E_a/2k_B T)$ , where  $E_a$  is the band gap energy, and  $k_B$  is Boltzmann's constant. The band gap is estimated to be  $391.2 \pm 21.8$  K ( $33.7 \pm 1.9$  meV)

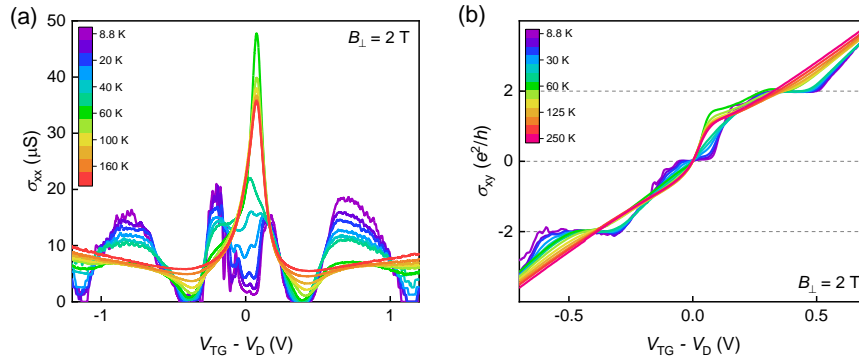


Fig. 9.9 Temperature dependence of (a)  $\sigma_{xx}$  and (b)  $\sigma_{xy}$  versus  $V_{TG} - V_D$  of Device I in 2 T.

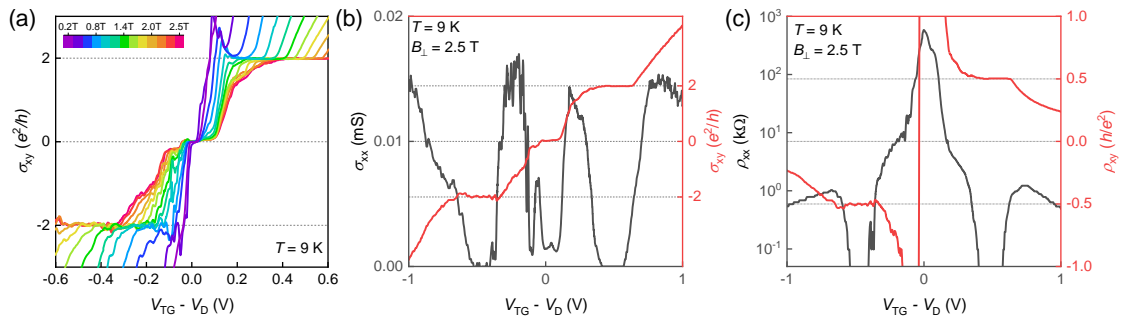


Fig. 9.10  $\nu = 0$  state in Device I. (a)  $\sigma_{xy}$  as a function of  $V_{TG} - V_D$  with an out-of-plane magnetic field from 0.2 T to 2.5 T at 9 K. (b)-(c) Transport measurements as a function of  $V_{TG} - V_D$  in 2.5 T and at 9 K. (b)  $\sigma_{xx}$  and  $\sigma_{xy}$ ; (c)  $\rho_{xx}$  and  $\rho_{xy}$ .

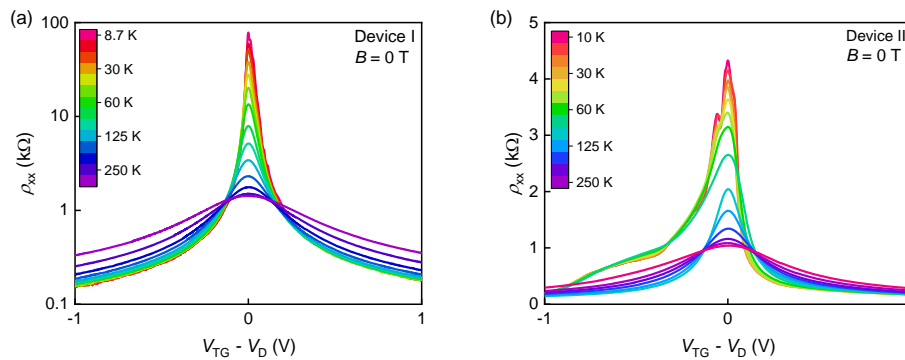


Fig. 9.11 Temperature dependence of  $\rho_{xx}$  near the DP in zero magnetic field for (a) Device I and (b) Device II.

for Device I and  $210.1 \pm 11.2$  K ( $18.1 \pm 1.0$  meV) for Device II. The larger band gap at the DP for Device I can be associated with the commensurate state, because most region of the graphene aligned to hBN would have the same crystal structure as hBN and probably enhance the global transport gap [94]. Device II has a smaller band gap due to a suppression of the commensurate state by one of the misaligned hBN layers [94].

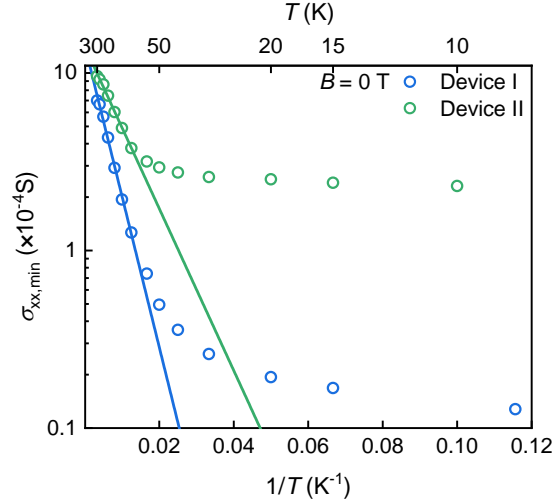


Fig. 9.12 Arrhenius plots of  $\rho_{xx}$  at the DP for Devices I and II.

#### 9.4.2 Variable range hopping

In the low temperature regime, the temperature dependence of  $\sigma_{xx,\min}$  has been analyzed with a variable range hopping (VRH) theory as originally formulated for semiconductor with localized impurity states [217–219], which is described by  $\sigma_{xx,\min} \propto \exp[-(T_0/T)^\eta]$  with  $\eta = 1/3$  ( $1/2$ ) corresponding to Mott VRH (Efros-Shklovskii VRH) in the presence of Coulomb interaction between electrons, and a characteristic temperature  $T_0$  determined by the localized states. In Figure 9.11,  $\sigma_{xx,\min}$  at  $T < 60$  K decreases slowly with lower temperature than the thermally activated regime, which indicates the onset of hopping conductivity.

Although VRH theory was not developed for graphene, the model has been successfully applied to various graphene systems with defects [220] as long as the conductance of the device is less than  $e^2/h$ . Figure 9.13 shows that  $\sigma_{xx,\min}$  can be fitted well with either Mott VRH or Efros-Shklovskii VRH model in Devices I and II.

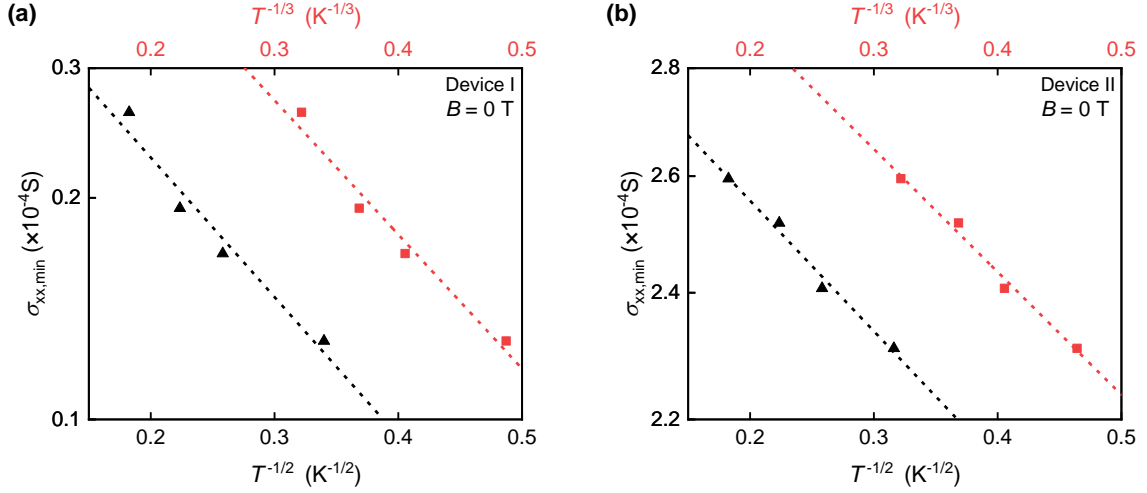


Fig. 9.13  $\sigma_{xx,\min}$  as a function of  $T^{-1/2}$  and  $T^{-1/3}$  of (a) Device I and (b) Device II on the semi-logarithmic scale. The data can be fitted with either Mott VRH or Efros-Shklovskii VRH model.

### 9.4.3 Quantum Hall effect evolution

Figure 9.14 shows the evolutions of  $\rho_{xx}$ ,  $\rho_{xy}$ ,  $\sigma_{xx}$  and  $\sigma_{xy}$  with gate voltage and increasing out-of-plane magnetic field ( $B_{\perp}$ ). Standard QHE with plateaux in  $\sigma_{xy}$  and dips in  $\sigma_{xx}$  at filling factors  $\nu = \pm 2, \pm 6, \pm 10, \dots$  are observed. A striking feature is a well-defined insulating region near the DP with increasing  $B_{\perp}$ , where  $\sigma_{xx} \rightarrow 0$  in Figure 9.14(a) and  $\rho_{xx} \geq h/2e^2$  in Figure 9.14(c).

## 9.5 Nonlocal transport measurements

### 9.5.1 Nonlocal transport in zero magnetic field

The gate voltage dependence of  $R_{nl}$  in zero magnetic field is investigated first. In Figure 9.15(a),  $R_{nl}$  for Device I shows a sharp peak (15.45 k $\Omega$ ) at the DP and  $\rho_{xx}$  has a  $1/n$  dependence which decreases at a slower rate than  $R_{nl}$  over the entire range of  $V_{TG}$  investigated. Within achievable  $V_{TG}$ , there is no detectable nonlocal resistance at the SDPs.  $R_{nl}$  for Device II (same geometry as I) is smaller (60  $\Omega$ ), consistent with a misalignment angle between graphene and hBN. In addition,  $R_{nl}$  exponentially decays as a function of nonlocal distance ( $L_n$ ) in graphene [ $R_{nl} \propto \exp(-L_n/\xi_0)$ ] with a characteristic length  $\xi_0 \approx 2.0 \mu\text{m}$  [Figure 9.15(b)]. The maxima in  $R_{nl}$  for all values of  $L_n$  investigated are an order of magnitude larger than previously reported values in equivalent devices with similar  $\mu$  [188].

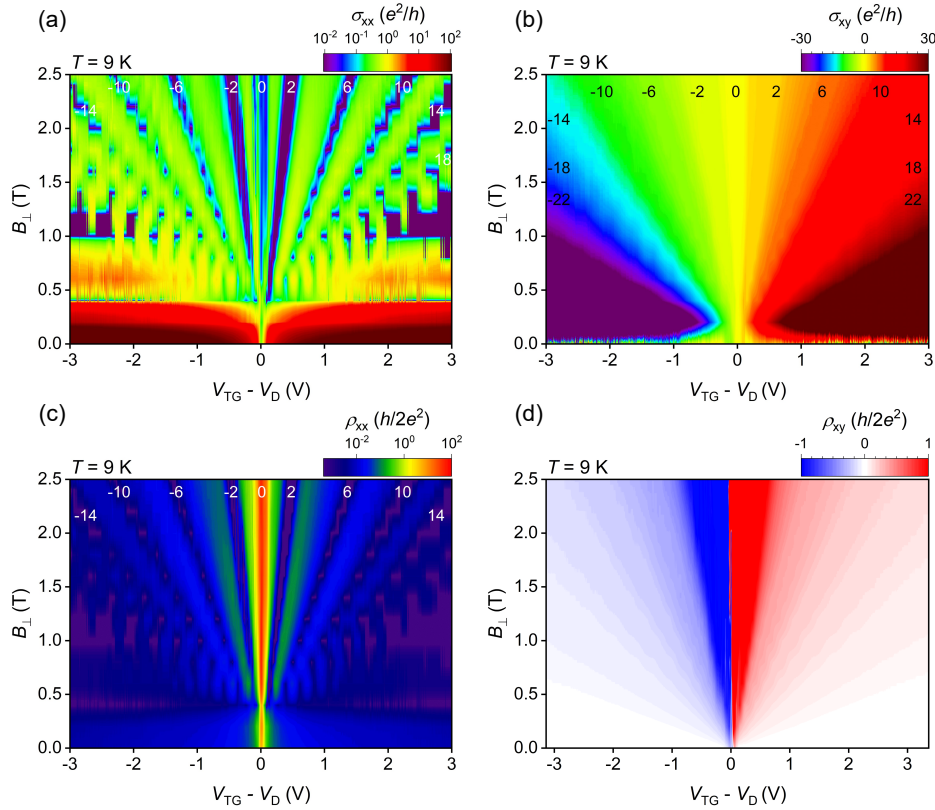


Fig. 9.14 Quantization in hBN/graphene/hBN superlattice of Device I. Logarithmic-scale plots of (a)  $\sigma_{xx}$  and (c)  $\rho_{xx}$  as a function of  $V_{TG} - V_D$  and  $B_{\perp}$  at 9 K. (b)  $\sigma_{xy}$  and (d)  $\rho_{xy}$  as a function of  $V_{TG} - V_D$  and  $B_{\perp}$  at 9 K. Numbers denote filling factors  $\nu$  for the QHE states extending from the DP.

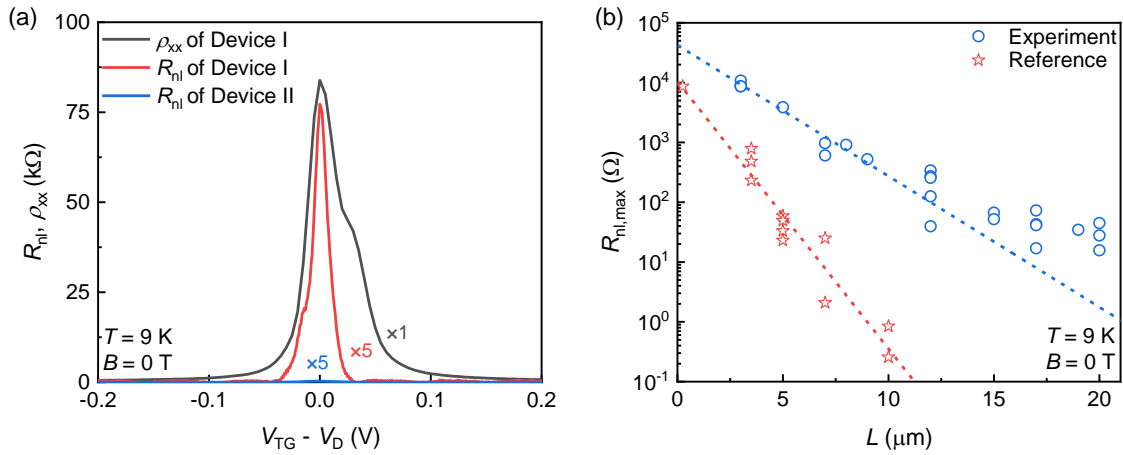


Fig. 9.15 Long-range nonlocal transport in hBN/graphene/hBN in zero magnetic field. (a)  $\rho_{xx}$  and  $R_{nl}$  versus  $V_{TG} - V_D$  in Devices I and II (labelled). (b) Distance dependence for  $R_{nl}$  in Device I. Nonlocal signal decays exponentially with increasing distance at 9 K. The nonlocal distance varies from 3  $\mu\text{m}$  to 20  $\mu\text{m}$  and device width is 2  $\mu\text{m}$ . Reference data is from [188].

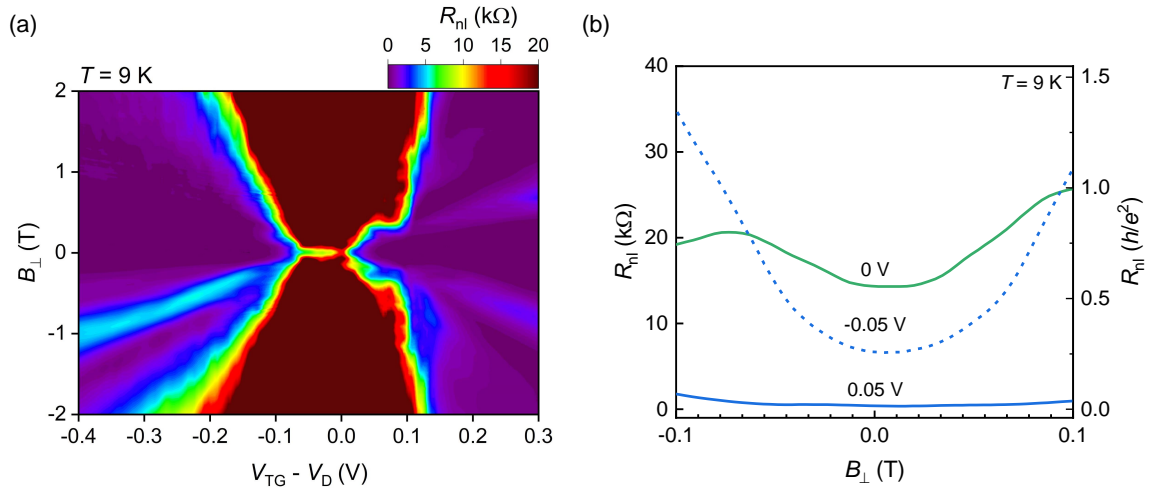


Fig. 9.16 Nonlocal magnetoresistance in Device I. (a)  $R_{nl}$  as a function of  $V_{TG} - V_D$  and  $B_{\perp}$  at 9 K. (b)  $R_{nl}$  versus  $B_{\perp}$  for different  $V_{TG}$  relative to the  $V_D$ .

### 9.5.2 Nonlocal transport under magnetic field

Figure 9.16(a) shows the  $R_{nl}$  as a function of  $V_{TG} - V_D$  and  $B_{\perp}$ . When a magnetic field is applied (above 0.1 T), a rapid broadening and increase occur in the value of  $R_{nl}$  at the DP, as contribution from charge-neutral spin currents becomes appreciable due to broken time reversal symmetry [182, 188].

### 9.5.3 Extrinsic origins of nonlocal resistance

Extrinsic origins of  $R_{nl}$  include Ohmic effect, Joule heating and Nernst-Ettingshausen effects as discussed in Chapter 8. These contributions are carefully ruled out. In Device I,  $L/W = 2$  and  $R_{xx} = 126 \text{ k}\Omega$ , from Equation (8.4), Ohmic contribution accounts for  $\sim 1\%$  of  $R_{nl}$  demonstrated in Figure 9.17. The carrier density dependence of  $\rho_{xx}$  is incompatible with the observed nonlocal response [Figure 9.18(a)]. At 9 K,  $\rho_{xx}$  remains sizable ( $> 100 \Omega$ ) over the entire range of accessible carrier density.  $R_{nl}$  decays rapidly with carrier density and completely disappears under detectable values for carrier density more than  $10^{10} \text{ cm}^{-2}$  away from the DP.

In all transport measurements, a low alternating-current excitation of  $\sim 10 \text{ nA}$  with a frequency of  $\sim 7 \text{ Hz}$  is used. The low current amplitude is chosen to minimize thermal contributions to the nonlocal transport due to Joule heating and Nernst-Ettingshausen effects [183] whilst simultaneously maximizing the signal-to-noise ratio of the measured voltages. In zero magnetic field, only Joule heating effect contributes to the second harmonic of nonlocal signal  $R_{nl,J}^{2f}$ , which is less than 1% of  $R_{nl}$  as shown in Figure 9.17.

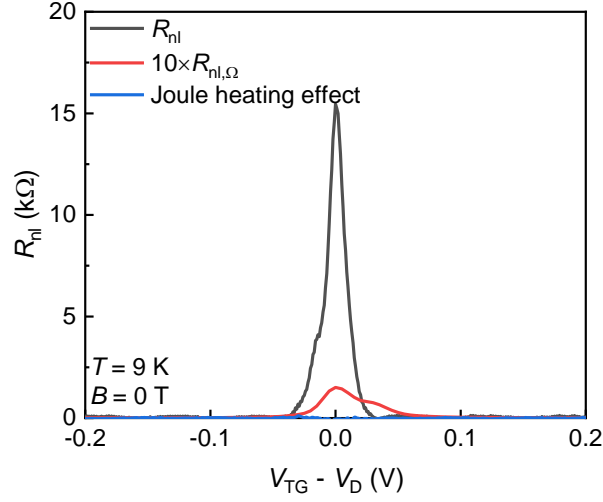


Fig. 9.17 Comparison of Ohmic and Joule heating contributions to  $R_{nl}$  in zero magnetic field at 9 K.

#### 9.5.4 Intrinsic origins of nonlocal resistance

In Figure 9.15(a), Devices I and II show different magnitudes of  $R_{nl}$  at the DP, which cannot be explained by charge-neutral spin currents, as these are indifferent to the relative alignment angle and require broken time reversal symmetry [92, 182, 183]. However, VHE is induced by the accumulated Berry curvature near hot spots and is associated with the transverse valley Hall conductivity ( $\sigma_{VH}$ ), which can be detected via  $R_{nl}$  according to  $R_{nl} \propto (\sigma_{VH})^2 \rho_{xx}^3$  (in the limit  $\sigma_{VH} \ll 1/\rho_{xx}$ ) from semiclassical transport theory [92, 188]. Figures 9.18(c)-(d) show that  $R_{nl} \propto \rho_{xx}^3$  holds at the DP for  $T \geq 60$  K, but not for  $T < 60$  K at both the hole and electron sides where  $R_{nl}$  is close to the quantum-limit value ( $h/2e^2$ ) in the insulating regime, which was observed in Ref. [95].

From the Arrhenius plot of the  $R_{nl}$  [Figure 9.18(b)], the associated band gap is estimated as  $760.4 \pm 69.9$  K ( $65.5 \pm 6.0$  meV) assuming that  $1/R_{nl} \propto \exp(-E_a/2k_B T)$  [95]. The obtained band gap is approximately 2.3 times larger than calculated from the local transport ( $330.1 \pm 18.3$  K). However, this result is considered to be reasonable in the case that  $R_{nl} \propto \rho_{xx}^3$  holds in the high temperature regime ( $T \geq 60$  K).

To confirm the origins of  $R_{nl}$  for  $T < 60$  K,  $R_{nl}$  is measured using a six-terminal configuration shown in Figure 9.19. In Ref. [95], a quantum valley Hall effect from a single pair of counter-propagating valley helical edge states was proposed in order to explain the quantum-limit values of  $R_{nl}$ , i.e. by assuming the minimal model where ballistic counter-propagating edge states connect terminals, the theoretical values for the quantized  $R_{nl}$  can

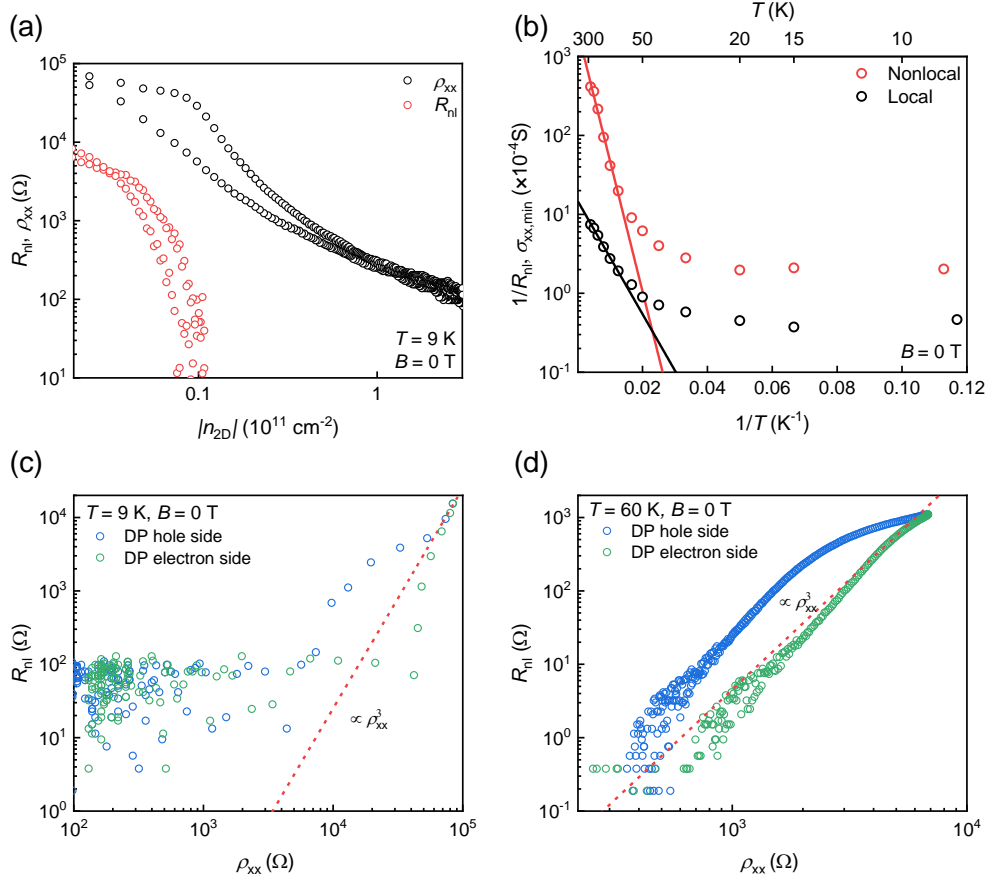


Fig. 9.18 Comparison between  $R_{nl}$  and  $\rho_{xx}$  in Device I. (a) Logarithmic scale of  $\rho_{xx}$  and  $R_{nl}$  as a function of  $n_{2D}$ . (b) Arrhenius plots of  $R_{nl}$  and  $\rho_{xx}$ . The estimated band gap is 65 meV for the  $R_{nl}$ , which is approximately two times larger than the band gap obtained from the local transport (28 meV). Scaling of  $R_{nl}$  as a function of  $\rho_{xx}$  at (c) 9 K and (d) 60 K. In the high temperature regime, the cubic scaling generally holds, which implies bulk topological currents. In contrast, in the low temperature regime, the cubic scaling doesn't hold.

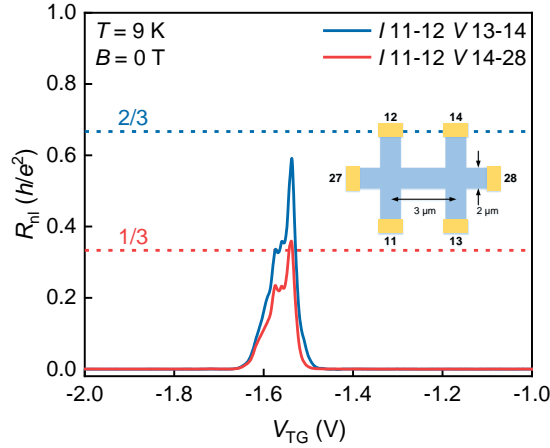


Fig. 9.19  $R_{nl}$  in a six-terminal configuration at 9 K versus  $V_{TG}$  where the horizontal (dotted) lines show theoretical values. Inset shows the measured configuration of Device I with terminal numbers.

be calculated using Landauer-Büttiker formalism [221, 222]. In Device I, theoretical values based on the minimal model [95] of  $R_{nl}$  for  $(I: 11,12, V:13,14)$  and  $(I: 11,12, V:14,28)$  are  $2h/3e^2$  and  $h/3e^2$ , respectively, are compared with the measurement results shown in Figure 9.19. The fluctuation between theoretical and measurement results may be due to charge impurities or the intervalley scattering on the disordered edge. While valley helical edge states exist for specific type of edges [203, 212, 223], they are spin-degenerate in all proposed theoretical models due to the spin-rotation symmetry, and therefore the microscopic origin of the quantum valley Hall state in Ref. [95] remains unknown.

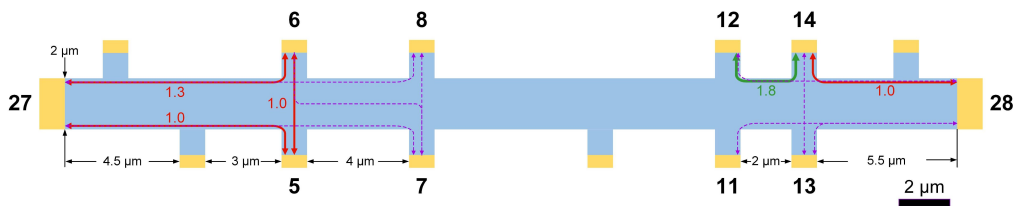


Fig. 9.20 Nonlocal transport geometry for the ten-terminal configuration including terminals 5, 6, 7, 8, 11, 12, 13, 14, 27 and 28. Arrows indicate the dominant connections between terminals.  $Tr_{ij}$  are shown with solid arrows for  $Tr_{ij} \geq 1.0$  and with dashed arrows for  $0.5 \leq Tr_{ij} < 1.0$ . The transmission probabilities approach the values expected for ballistic edge state transport.

To investigate the emergence of the quantum valley Hall state,  $R_{nl}$  is systematically measured using a ten-terminal configuration (Figure 9.20) in order to determine the conductance matrix. Device I is fabricated with 18 terminals [Figure 9.2(a)], 14 of which show low contact

Table 9.1 Maximum transmission probabilities  $Tr_{ij}$  in  $-1.7 \text{ V} \leq V_{\text{TG}} \leq -1.5 \text{ V}$  for  $R_{\text{nl}}$  in ten-terminal configuration.  $Tr_{ij}$  of terminals connected by edges are indicated with green color (shortest distance between terminals), blue color (intermediate distance between terminals) and red color (longest distance between terminals). Other pairs of terminals with  $Tr_{ij} \geq 0.5$  are indicated with orange color. The error bars for the transmission probabilities are at least 0.2.

	T27	T05	T07	T11	T13	T28	T14	T12	T08	T06
T27		1.0	0.7	0.1	0.1	0.2	0.2	0.2	0.6	1.3
T05	1.1		0.4	0.1	0.0	0.1	0.1	0.2	0.4	1.1
T07	0.7	0.5		0.1	0.1	0.3	0.2	0.4	0.8	0.6
T11	0.1	0.1	0.2		0.2	0.5	0.5	0.6	0.1	0.1
T13	0.1	0.1	0.1	0.2		0.7	0.7	0.5	0.1	0.1
T28	0.2	0.2	0.5	0.6	1.0		1.0	0.7	0.2	0.1
T14	0.1	0.1	0.3	0.3	0.6	1.3		1.8	0.2	0.1
T12	0.2	0.1	0.2	0.4	0.4	0.8	2.0		0.3	0.1
T08	0.6	0.3	0.8	0.2	0.1	0.2	0.2	0.3		0.6
T06	1.3	1.0	0.6	0.1	0.1	0.2	0.1	0.1	0.4	

resistances (Figure 9.20). In order to measure  $R_{\text{nl}}$ , 10 terminals located symmetrically are selected. The calculated transmission matrix based on the Landauer-Büttiker formalism is shown in Table 9.1 (see Appendix A for details), the dominant values of  $Tr_{ij}$  are marked with different colors (green, blue, red and orange) and plotted in Figure 9.20. Because the distance between some pairs of terminals are longer than the intervalley diffusion length,  $Tr_{ij}$  would be slightly different from ideal values. Nevertheless, if the nonlocal transport is dominated from edge states,  $Tr_{ij}$  would obey the order of green > blue > red. The calculated transmission matrix does not strictly agree with the minimal model for edge state transport proposed in Ref. [95]. However, the transmission probability is approximately 2.0 between terminals 12 and 14 in the narrow  $V_{\text{TG}}$  range near the DP, consistent with spin-degenerate ballistic counter-propagating edge states.

Moreover, the transmission probabilities reach approximately 1.0 between terminals 5 and 27, 6 and 27, 14 and 28. When the edge states enter these unused but connected terminals, they interact with a reservoir of states and equilibrate to the chemical potential determined by the voltage at each terminal. Therefore, electrons will be injected backward and forward with equal probability. These unused terminals in-between the measurement terminals effectively reduce the transmission probability by a half, consistent with the calculated values (1.0). Figure 9.20 shows that a number of pairs of terminals behave like edge state transport, but others show more complicated behaviors. It is known that commensurate stacking in aligned van der Waals heterostructures ( $\varphi < 1^\circ$ ) leads to the soliton-like narrow domain

walls [224]. One-dimensional conducting channels exist at these domain walls, which can form a conducting network to nonlocal signals when bulk graphene/hBN superlattice domains become insulating [225–229]. The transmission probabilities for terminals 5, 6, 7 and 8 are significantly smaller than expected values based on ballistic counter-propagating edge states, which perhaps are consistent with the existence of soliton-like narrow domain walls.

In addition, the obtained transmission probabilities ( $Tr_{ij}$ ) in Table 9.1 do not fully obey the time reversal symmetry ( $Tr_{ij} = Tr_{ji}$ ). It could be related to the measurement noise errors, non-ideal contacts in-between the measurement terminals or interaction-driven weakly broken time reversal symmetry.

## 9.6 Summary and future work

In summary, hBN/graphene/hBN superlattice Hall bars with a field-effect mobility of  $220,000 \text{ cm}^2 \text{ V}^{-1} \text{ s}^{-1}$  at 9 K are fabricated. Perfect alignment between hBN and graphene ( $\varphi < 1^\circ$ ) leads to a  $\sim 33.7 \text{ meV}$  band gap at the DP. At low temperature, a  $\nu = 0$  state in gapped graphene is demonstrated in  $\sigma_{xx}$  and  $\sigma_{xy}$  with large  $R_{nl}$  values close to  $h/2e^2$ .  $R_{nl}$  decays nonlocally over distances of  $15 \mu\text{m}$  with a characteristic decay constant of  $2 \mu\text{m}$ . Nonlocal measurements demonstrate that below 60 K, the most plausible explanation is the spin-degenerate ballistic counter-propagating edge state, but there is also a secondary contribution from a network of one-dimensional conducting channels appearing at the soliton-like domain walls. The spin-degenerate ballistic counter-propagating edge states offer possibilities for electronic applications beyond QSHE and QAHE since quantized resistance can be observed at high temperatures with a tunable energy gap through valley coupling.

### Microscopic mechanism of complicated nonlocal transport in graphene superlattice

In Table 9.1 and Figure 9.20, there are several pairs of terminals showing more complicated behaviors than simple edge state transport. Transmission probability between terminal 11 and 13 is very small, and terminal 11 is also connected to terminals 28, 14 and 12. A possible mechanism is one-dimensional conducting channels which can exist at soliton-like domain walls in aligned van der Waal heterostructure [224]. So terminal 11 is in a node of a network of one-dimensional conducting channels. Ju *et al.* used the near-field infrared nanometre-scale microscopy (Figure 9.21) to image *in situ* bilayer graphene domain walls and demonstrated existence of one-dimensional valley-polarized conducting channels with a ballistic length of about 400 nm at 4 K [226]. If the edge state intersects with a domain wall, the carriers can go into two different directions at the intersection, and this would lower the transmission probability for each given direction. The intersection point will also be a center

of scattering, resulting in backscattering. Alternatively, it could be that the edge between terminal 11 and 13 is armchair type which does not support edge states. It could also be terminals are not ideal contacts. So imaging domain walls in graphene superlattice can help identify the microscopic mechanism of these complicated behaviors.

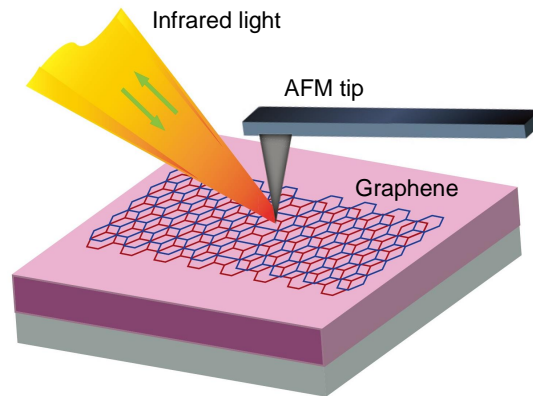


Fig. 9.21 Illustration of the near-field infrared nanoscopy measurement of graphene on  $\text{SiO}_2/\text{Si}$  substrate. Infrared light (orange) is focused onto the apex of a metal-coated AFM tip and the backscattered infrared radiation is collected and measured by an  $\text{HgCdTe}$  detector in the far field. Reprinted with permission from [226]. Copyright (2015) Springer Nature.

### Valleytronics in two-dimensional materials

The degeneracy of the valley degree of freedom related to the  $K$  and  $K'$  points in the Brillouin zone, can be used in electronic devices in a similar way as the spin of electron is used in spintronics. A valley polarization is a key element for valleytronics [17]. Graphene/hBN superlattice shows a high degree of valley polarization with valley Hall conductance reaching the theoretical maximum of  $2e^2/h$ . And valley currents can be switched off by tuning the Fermi level away from regions of the electronic spectrum with a large Berry curvature. Then it is possible to use graphene/hBN superlattice in valleytronics. Gorbachev *et al.* made a graphene valley-based transistor with a top-gate and demonstrated the possibility of switching off valley current by tuning top-gate voltage [188].

To realize practical valleytronic devices, the valley polarization lifetime must be longer than any gate operation time. Semiconducting TMDs have strong spin-orbit coupling and spin-valley coupling, which can enhance the valley polarization lifetime [230]. Valley polarization has been observed in single layer  $\text{MoS}_2$  [231, 232] and the tunable VHE has been reported in bilayer  $\text{MoS}_2$  [233]. The experimental observations of VHE in symmetry-broken graphene systems and TMDs are important steps towards valleytronic devices.



# Chapter 10

## Zeroth Landau level in magnetic graphene

Graphene is a gapless diamagnetic material, presents limited applications in spintronics on its own due to the lack of spin-filter capabilities. Advances on magnetizing graphene [234, 235] have been achieved in the last few years. Some of the most common approaches, involving the introduction of carbon vacancies [236] or the hydrogenation of the carbon sheet [237], turned out to be detrimental for graphene's unique electronic and spintronic transport performance. Magnetism can also be introduced in graphene by placing it on a magnetic substrate [23, 104] through  $\pi$  orbital coupling to the surface states of substrate without disturbing the delicate electronic properties of the graphene. This approach can theoretically result in magnetic exchange field of hundreds of Tesla [97, 149, 238, 239].

This chapter reports a proximity-induced magnetic exchange field in exfoliated single layer graphene by placing it on the insulating ferrimagnetic garnet ( $\text{Y}_3\text{Fe}_5\text{O}_{12}$  or YIG) by investigating the competition between antiferromagnetic (AF) and spin-polarized ferromagnetic (F) quantum Hall states in graphene at the zeroth Landau level. From nonlocal transport measurements in graphene Hall bar on YIG at the  $\nu = 0$  quantum Hall state, the induced magnetic exchange field in graphene lowers the magnetic field ( $> 6$  T) required to modulate the magnetic state at 2.7 K.

### 10.1 Introduction

Graphene has two inequivalent Dirac cones in the energy band dispersion, which lead to a set of Landau levels with distinct features over conventional two-dimensional electron gases. In an applied magnetic field ( $\vec{B}$ ), there are fourfold degenerate symmetry-broken zero-energy

Landau levels with filling factors  $\nu = 0, \pm 1$  in graphene [137, 139]. These are gate voltage tunable and described by spin and valley degeneracy. Electron-electron and electron-phonon interactions break valley symmetry and determine the magnetic order of the  $\nu = 0$  state.

Theory [142, 240, 241] and experiment [242–245] indicate that  $\nu = 0$  is an AF quantum Hall state [242, 245] in which the two sublattice spins of graphene align antiparallel. The Zeeman field ( $B_Z$ ) associated with an in-plane magnetic field ( $B_{||}$ ) favors a spin-polarized F state [244] (that also can be found at  $\nu = \pm 1$  [242]), but in general the AF and F states compete leading to a canted antiferromagnetic (CAF)  $\nu = 0$  state at half-filled zero-energy Landau level in which the two sublattice spins tilt out-of-plane. The spin-direction in the CAF state depends on the sum of the spin components parallel (preferred by the Zeeman field, responsible for the F state) and perpendicular (preferred by the electron-electron Coulomb interactions responsible for the valley anisotropy and leading to the AF state) to  $\vec{B}$ . In the AF state, there are gapped edge modes whilst the F state supports gapless counter-propagating ones [144, 240, 242]. Therefore, in the CAF state the energy gap of the edge modes is tunable with the direction and magnitude of  $\vec{B}$  [240].

Edge modes associated with CAF and F states have been detected in graphene Hall bars through nonlocal measurements with a transition between F and CAF states occurring around 15-30 T [244]. In the ballistic limit, the nonlocal resistance ( $R_{nl}$ ) is quantized and dependent on the Hall bar geometry [205]. In the diffusive limit,  $R_{nl}$  is not quantized but shows different behaviors with gate voltage ( $V_{TG}$ ) in the AF, CAF and F states [Figures 10.1(a)-(c)]: the AF state does not support edge modes meaning  $R_{nl} = 0$ , but the CAF (F) is gapped (gapless) and  $R_{nl}(V_{TG})$  shows a double peak (single peak) near the Dirac point ( $V_D$ ).

Transitions between CAF and F (or AF) states could be achieved at low applied magnetic fields if graphene has an intrinsic magnetic exchange field ( $\vec{M}_{ex}$ ). By placing graphene on an insulating magnetic substrate, a hybridization of the  $\pi$  orbitals in graphene with the substrate can induce a magnetic exchange field. The magnitude of the total magnetic field ( $M_T = |\vec{M}_T|$ ) applied to graphene is then related to  $\vec{M}_T = \vec{M}_{ex} + \frac{g}{2}\vec{B}$  [Figure 10.1(d)], where  $g$  is gyromagnetic ratio and  $\frac{g}{2}\vec{B}$  is the Zeeman field.  $\vec{M}_{ex}$  induced from magnetization ( $M_{sub}$ ) of the substrate is parallel to the  $\vec{B}$ . A 14 T magnetic exchange field was recently estimated in graphene on EuS [104] and an anomalous Hall effect in graphene on YIG showed evidence for an induced magnetic exchange field in graphene [23]. In Refs. [23, 104], transitions between CAF and F (or AF) states were not investigated.

Here a transition between CAF and F states in hBN covered graphene Hall bars on YIG is reported. These are investigated through gate-voltage-dependent nonlocal transport measurements below 9 K. The magnetic state and energy gap of the edge modes in graphene are found to be tunable by varying the magnitude ( $> 6$  T) and direction of an applied magnetic

field ( $\vec{B}$ ). The readily tunable energy gap is important from a fundamental physics viewpoint, as it separates quantum states with distinct magnetic ordering in graphene, and also implies potential relevance for applications requiring tunable energy gaps, such as photodetectors.

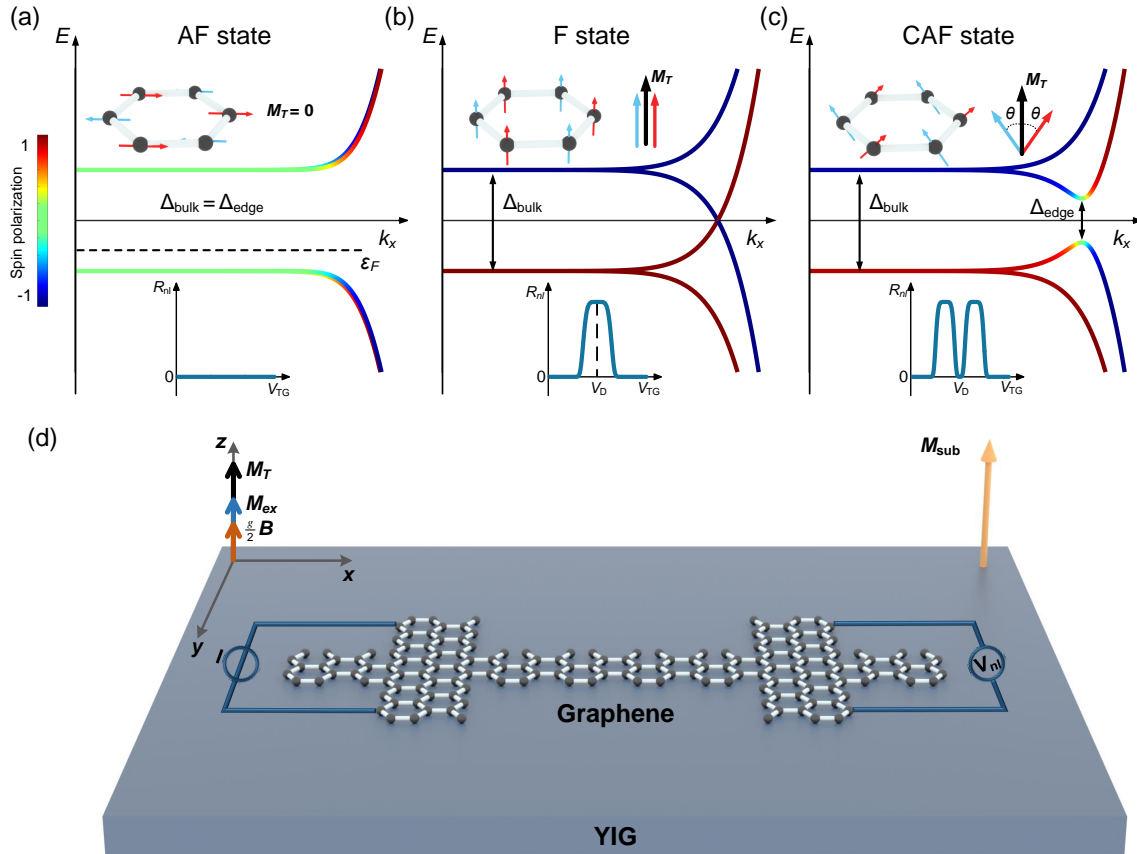


Fig. 10.1 Energy spectra of the (a) AF, (b) F, and (c) CAF states in graphene which arise depending on the magnitude of the total magnetic field ( $\vec{M}_T$ ) applied to graphene and the angle ( $\theta$ ) between  $\vec{M}_T$  and the sublattice spins. Color scale bar shows -1 (spin-direction antiparallel to  $\vec{M}_T$ ) to 1 (spin-direction parallel to  $\vec{M}_T$ ). Top insets of (a)-(c): Diagrams illustrating the sublattice spins in graphene (left) which make angle  $\theta$  with respect to  $\vec{M}_T$  (right). Bottom insets of (a)-(c):  $R_{nl}$  versus gate voltage ( $V_{TG}$ ) for AF, F, and CAF states at  $V_D$ . The AF state (a) forms when  $\vec{M}_T$  is zero (sublattice spins are antiparallel). The F state (b) forms when  $\vec{M}_T$  is larger than the critical value (determined by the Coulomb interaction) and the sublattice spins are parallel to  $\vec{M}_T$ . The CAF state (c) is a mixture of AF and F states and forms when  $\vec{M}_T$  is nonzero, but smaller than the critical value (sublattice spins are non-collinear to  $\vec{M}_T$ ). (d) Illustration of a graphene Hall bar on YIG in which magnetization ( $M_{sub}$ ) induces a nonzero  $\vec{M}_{ex}$  which adds to the Zeeman field ( $\frac{g}{2}\vec{B}$ ).

## 10.2 Device fabrication

Ferrimagnetic insulator YIG is chosen since it has a high Curie temperature of 550 K (16.5 K for EuS), a wide band gap of 2.84 eV [246] (1.65 eV for EuS) and is chemically stable in the air which minimizes surface degradation during Hall bar fabrication. Furthermore, YIG has an electrical resistivity of  $10^{12} \Omega \text{ cm}$ . Atomically flat (110) YIG is prepared by pulsed laser deposition onto single crystal GGG with a bulk magnetization of  $144 \text{ emu cm}^{-3}$  (see Chapter 7 for details).

Magneto-transport in graphene on YIG is probed using Hall bars which are fabricated in several steps involving exfoliation of graphene from graphite and dry transfer onto YIG. Electron beam lithography is used to fabricate Cr/Au side-contacts (see Chapter 6 for details). The graphene is covered with a 20 to 50-nm-thick hBN. The top hBN protects the graphene from the environment and exhibiting high mobility, low residual doping and low charge inhomogeneity [26]. A representative hBN/graphene Hall bar on YIG with a 40-nm-thick  $\text{AlO}_x$  top-gate dielectric layer is shown in Figure 10.2. Control Hall bar of hBN/graphene/ $\text{AlO}_x$ /YIG is investigated in which graphene is decoupled from YIG with a 6-nm-thick  $\text{AlO}_x$  layer.

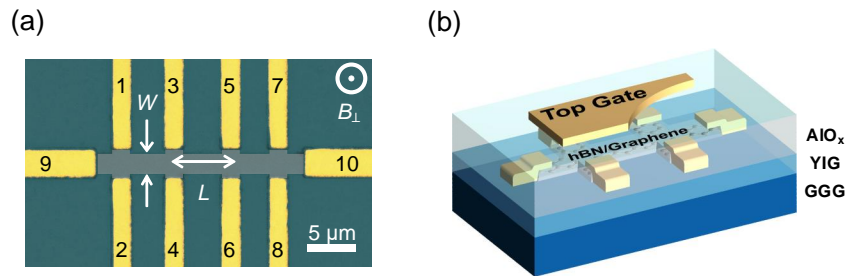


Fig. 10.2 hBN/graphene Hall bar on YIG structure. (a) Optical micrograph (false color) of a representative Hall bar prior to top-gate electrode deposition.  $B_{\perp}$  is an out-of-plane applied magnetic field. (b) Schematic illustration of a Hall bar with the top-gate.

## 10.3 Device characterization

### 10.3.1 Raman spectroscopy

Before Hall bar fabrication, Raman spectroscopy is performed on the graphene prior to and following transfer onto YIG or  $\text{AlO}_x$ . The absence of D peak ( $\sim 1345 \text{ cm}^{-1}$ ) in Figure 10.3(a) indicates there is no detectable lattice defects in graphene. The positions of G

peak ( $\sim 1580 \text{ cm}^{-1}$ ) and 2D peak ( $\sim 2700 \text{ cm}^{-1}$ ) of graphene on different substrates vary in Figure 10.3(a) due to different doping levels [247].

To investigate structural and electronic homogeneity of the graphene on YIG, Raman maps are measured at 293 K [Figures 10.3(b)-(c)]. The positions of the 2D peak [Pos(2D)] are in the range of  $2680\text{--}2700 \text{ cm}^{-1}$ , and the FWHM(2D) is in the range of  $20\text{--}30 \text{ cm}^{-1}$ . The atomically clean interface between the graphene and hBN over the entire active device area is selected by Raman maps [ $2690 \text{ cm}^{-1} \leq \text{Pos}(2\text{D}) \leq 2700 \text{ cm}^{-1}$  and  $20 \text{ cm}^{-1} \leq \text{FWHM}(2\text{D}) \leq 25 \text{ cm}^{-1}$ ].

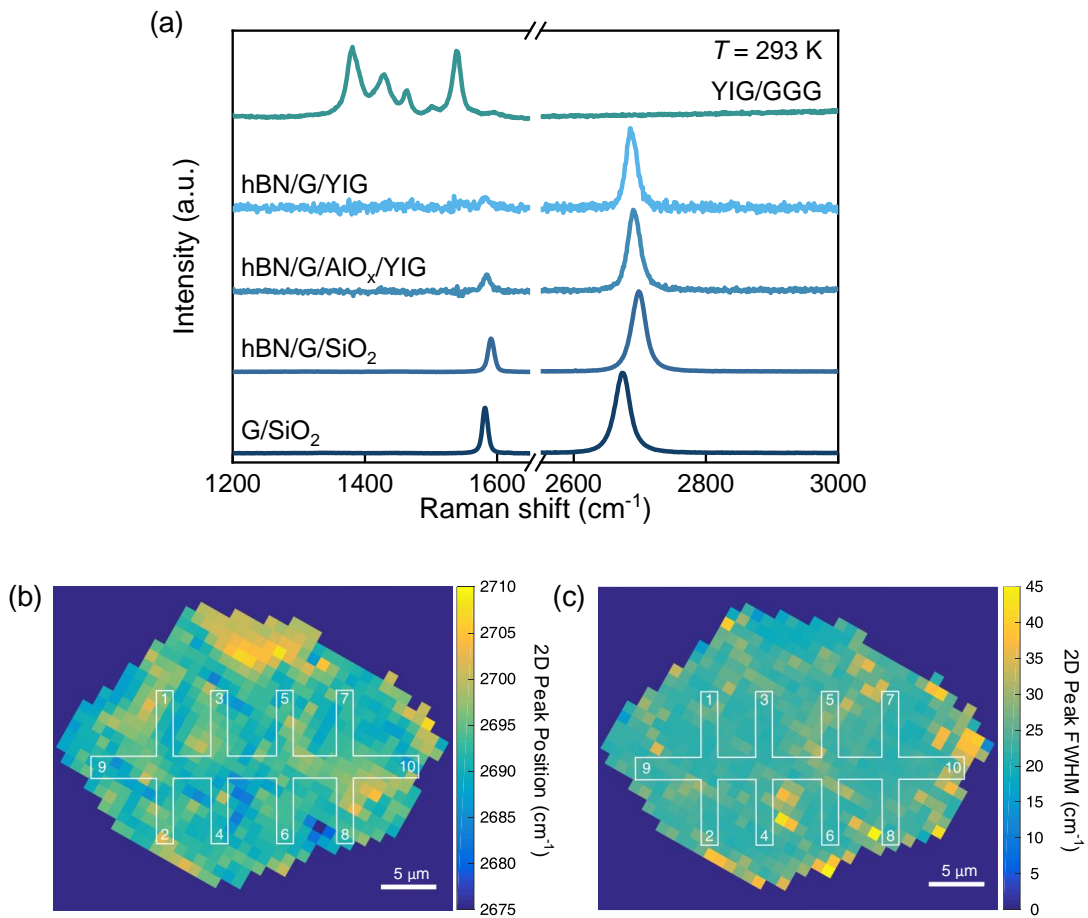


Fig. 10.3 Raman spectra of graphene on YIG. (a) Raman spectra at 293 K for different structures (labelled; G stands for graphene). The background Raman spectra from hBN and YIG/GGG are subtracted. Raman spectra maps of (b) positions and (c) FWHM of the 2D peak at 293 K, where white solid lines show the position of the Hall bar.

### 10.3.2 Hall-effect and field-effect mobility

The quality of the Hall bar devices is characterized through Hall-effect and field-effect mobility ( $\mu$ ). The Hall-effect mobility of hBN/graphene/YIG can be tuned by the top-gate voltage (from -5 V to 1 V with a leakage current of  $\sim 2 \times 10^{-11}$  A) up to  $50,000 \text{ cm}^2 \text{ V}^{-1} \text{ s}^{-1}$  with  $5 \times 10^{10} \text{ cm}^{-2}$  carrier density at 9 K [Figure 10.4(a)]. The field-effect mobility is up to  $12,000 \text{ cm}^2 \text{ V}^{-1} \text{ s}^{-1}$  at 9 K [Figures 10.4(b)-(c)] and  $40,000 \text{ cm}^2 \text{ V}^{-1} \text{ s}^{-1}$  at 2.7 K [Figure 10.4(d)] with carrier density of  $10^{11} \text{ cm}^{-2}$ .  $\mu$  of hBN/graphene/YIG is higher than previous reported on exfoliated [23] or chemical vapor deposited [24, 248, 249] graphene on YIG. Control Hall bar of hBN/graphene/ $\text{AlO}_x$ /YIG has the field-effect mobility of up to  $19,000 \text{ cm}^2 \text{ V}^{-1} \text{ s}^{-1}$  at 9 K, which is higher than hBN/graphene/YIG.

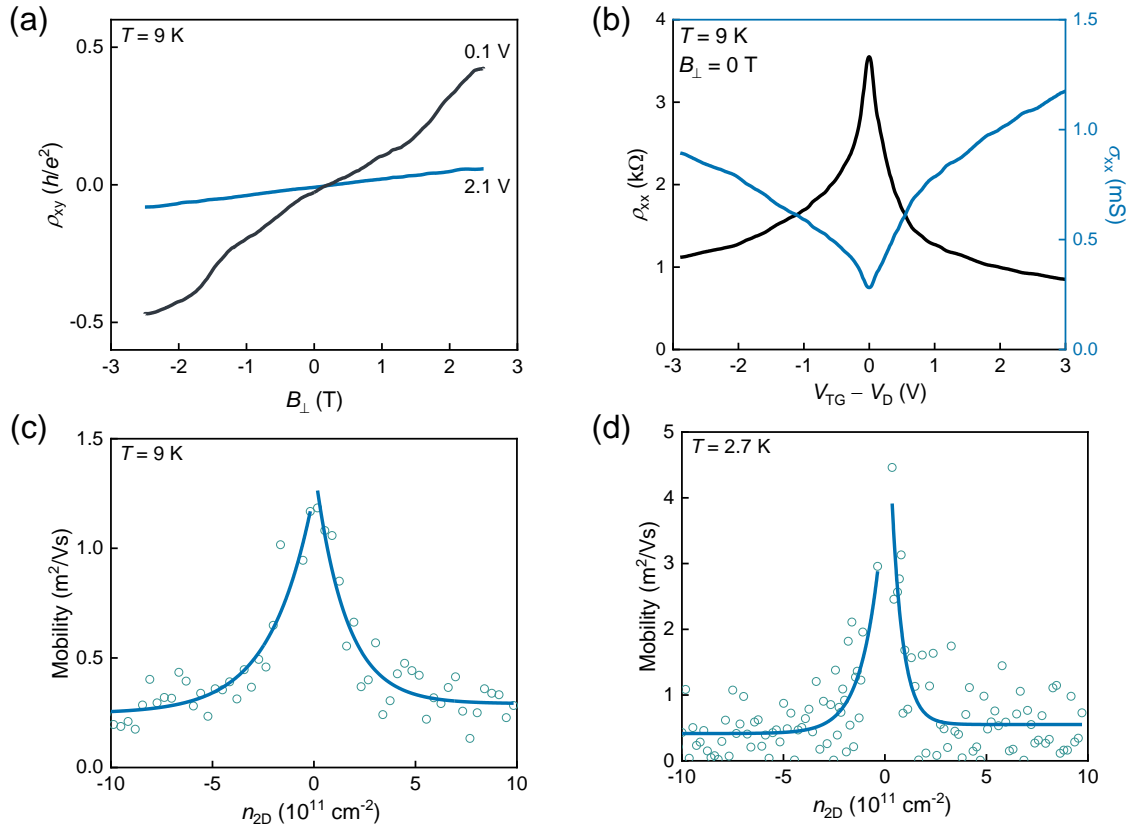


Fig. 10.4 Mobility of hBN/graphene Hall bar on YIG. (a)  $\rho_{xy}$  versus  $B_{\perp}$  at different gate voltages at 9 K. (b)  $\rho_{xx}$  and  $\sigma_{xx}$  versus  $V_{\text{TG}} - V_{\text{D}}$  in zero magnetic field at 9 K. Field-effect mobility versus  $V_{\text{TG}} - V_{\text{D}}$  at (c) 9 K and (d) 2.7 K.

## 10.4 Transport measurement

### 10.4.1 Local and nonlocal transport in zero magnetic field

The local and nonlocal transport in zero magnetic field are investigated at 9 K first. Figure 10.5(a) shows a peak in  $R_{nl}$  at the DP ( $V_D$ ). By normalizing  $R_{xx}$  and  $R_{nl}$  to their respective maximum values at  $V_D$  ( $R_{xx,D}$  or  $R_{nl,D}$ ),  $R_{nl}/R_{nl,D}$  is an order of magnitude smaller than  $R_{xx}/R_{xx,D}$  and the peak in  $R_{nl}$  is sharper than  $R_{xx}$  [right inset in Figure 10.5(a)]. The peak in  $R_{nl}$  ( $\sim 380 \Omega$ ) at  $V_D$  may indicate a contribution from the spin Hall [250] or Zeeman spin Hall effects [242]. However,  $R_{xx}$  shows a negative magnetoresistance (weak localization) (Figure 10.6) at 2.7 K suggesting that Rashba spin-orbit coupling is not strong at the graphene/YIG interface, meaning the spin Hall effect is unlikely to dominate  $R_{nl}$ . The YIG has a small remanent out-of-plane magnetic moment [24] [Figure 7.7(b)] which may support the Zeeman spin Hall effect. Ohmic and thermal contributions to  $R_{nl}$  in hBN/graphene Hall bar on YIG are negligible (see Chapter 8 for details). Equivalent measurements on the hBN/graphene/ $\text{AlO}_x$ /YIG control Hall bar in Figure 10.5(b) show a reduced  $R_{nl}$  at  $V_D$  of  $\sim 65 \Omega$  at 9 K which is dominated by the Ohmic effect. This suggests that in zero magnetic field,  $R_{nl,D}$  in hBN/graphene/YIG is due to a coupling between graphene and YIG.

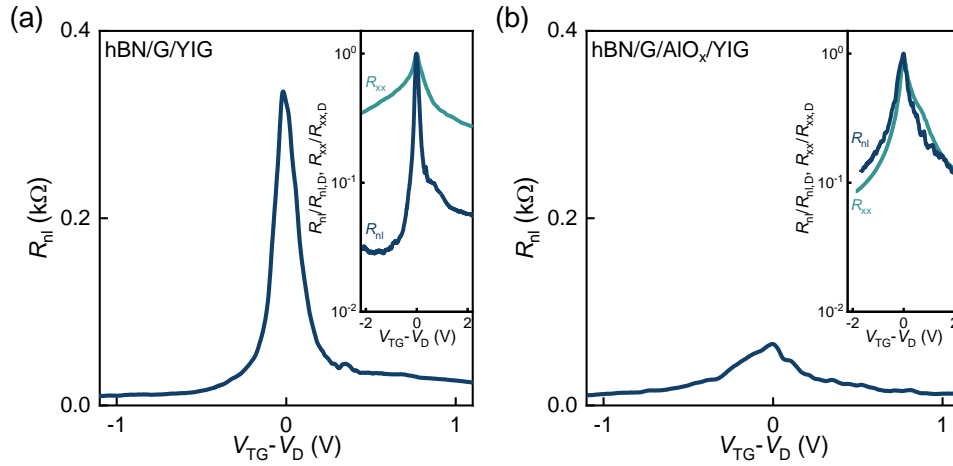


Fig. 10.5  $R_{nl}$  versus  $V_{TG} - V_D$  at 9 K for (a) an hBN/graphene Hall bar on YIG and (b) a control Hall bar (labelled) with insets (right) showing  $R_{xx}/R_{xx,D}$  and  $R_{nl}/R_{nl,D}$  versus  $V_{TG} - V_D$  for the same Hall bar in zero magnetic field.

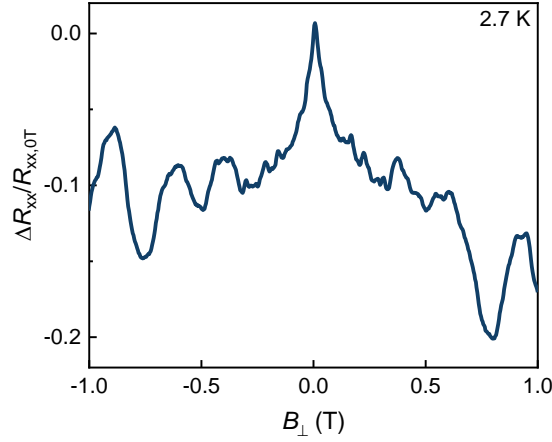


Fig. 10.6 Low field normalized magnetoresistance  $(R_{xx} - R_{xx,0T})/R_{xx,0T}$  versus  $B_{\perp}$  at 2.7 K. It shows sharp and symmetric peak around zero magnetic field, arising due to weak localization.

### 10.4.2 Local and nonlocal transport under magnetic field

Figures 10.7(a)-(c) show the gate-voltage-dependent Shubnikov-de Haas oscillations in  $R_{xx}$  and  $R_{nl}$  ( $B_{\perp} = 1$  T and 1.5 T) and their normalized values at  $V_D$  of  $B_{\perp} = 2.5$  T for hBN/graphene Hall bar on YIG. The ratios  $R_{nl}/R_{nl,D}$  and  $R_{xx}/R_{xx,D}$  show different trends with gate voltage with  $R_{nl}$  decreasing faster than  $R_{xx}$  in Figure 10.7(c). Furthermore,  $R_{nl}$  is a factor of 50 larger than in the hBN/graphene/ $\text{AlO}_x/\text{YIG}$  control Hall bar [Figure 10.7(d)]. These observations in conjunction with the fact that the Onsager relation  $R_{56,78}(B_{\perp}) = R_{78,56}(-B_{\perp}) \neq R_{78,56}(B_{\perp})$  for hBN/graphene Hall bar on YIG holds [Figure 10.7(e)], demonstrate a contribution to  $R_{nl}$  from the Zeeman spin Hall effect [104] due to an induced magnetic exchange field. Shubnikov-de Haas oscillations are observed in Figure 10.7(f) for  $B_{\perp} \geq 1$  T showing Landau levels at filling factors  $\nu = 4(N + 1/2)$ , where  $N = 0, \pm 1, \pm 2, \dots$

### 10.4.3 $\nu = 0$ state in hBN/graphene Hall bar on YIG

The energy of a Landau level ( $N$ ) is  $E_N = \pm \sqrt{2|N| \hbar v_F^2 e B_{\perp}}$ , where  $e$  is the electron charge,  $\hbar$  is the Planck's constant divided by  $2\pi$ ,  $v_F$  is the Fermi velocity, and  $N = 0, \pm 1, \pm 2, \dots$ . For large out-of-plane magnetic field ( $B_{\perp}$ ), quantum Hall plateaus at  $\nu = 0$  and  $\pm 1$  may become visible. The half-filled  $\nu = 0$  state at the zeroth Landau level should show a minimum in longitudinal conductance ( $\sigma_{xx}$ ) while the other filling factors at a quarter and three-quarter occupancy are at a maximum. Figures 10.8(a)-(d) show the gate-voltage-dependence of  $\sigma_{xx}$  for increasing values of  $B_{\perp}$ : when  $B_{\perp} = 4$  T a minimum of  $\sigma_{xx}$  is visible at  $V_D$  and approaches

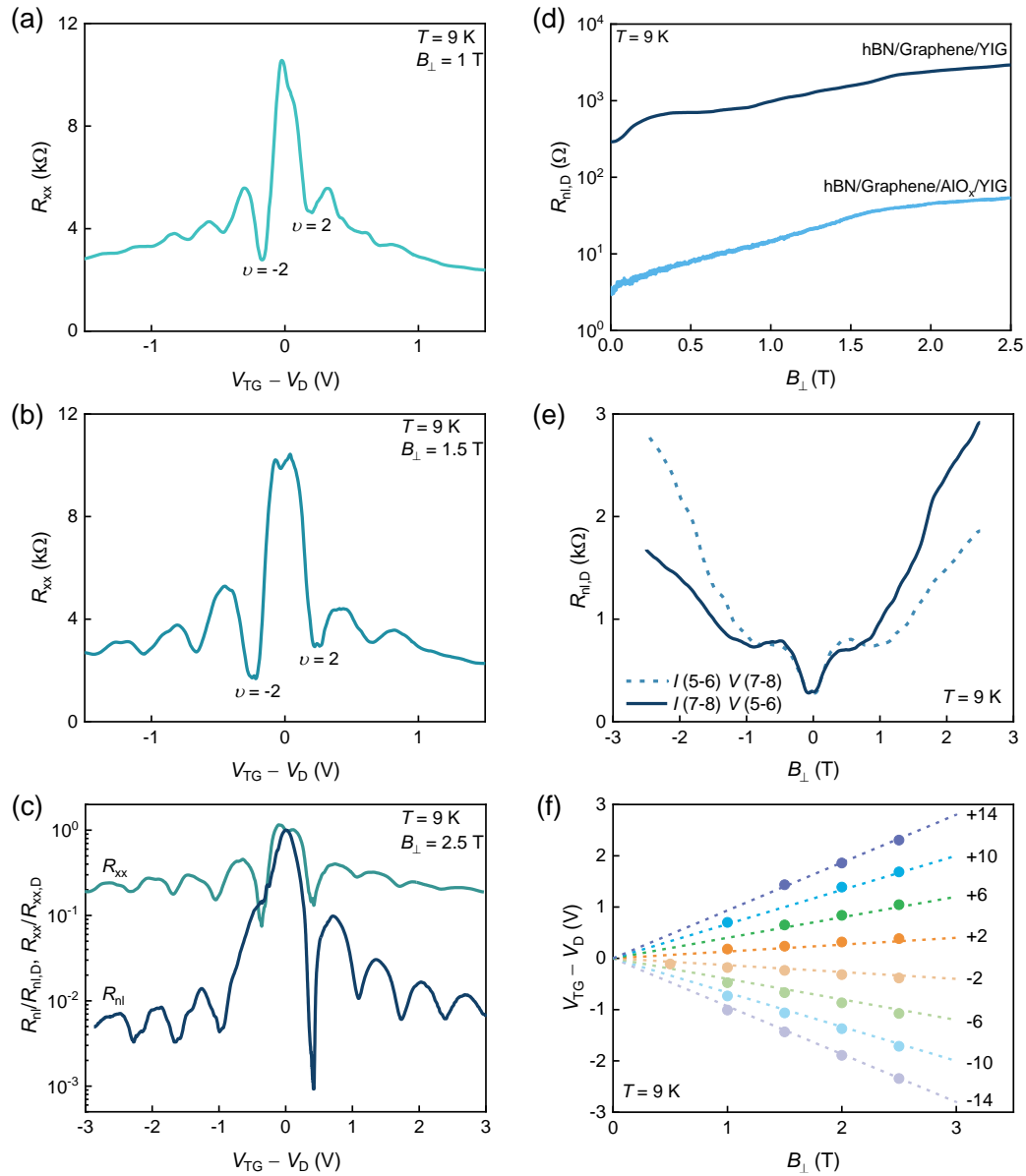


Fig. 10.7 (a) to (b)  $R_{xx}$  versus  $V_{TG} - V_D$  for  $B_{\perp}$  of 1 T and 1.5 T (labelled). (c) Gate-voltage-dependence of  $R_{xx}/R_{xx,D}$  and  $R_{nl}/R_{nl,D}$  with  $B_{\perp} = 2.5$  T. (d) Rise in  $R_{nl,D}$  with  $B_{\perp}$  for hBN/graphene Hall bar on YIG compared to the hBN/graphene/AIO<sub>x</sub>/YIG control Hall bar at 9 K. (e)  $R_{nl,D}$  versus  $B_{\perp}$  for reverse electrical connections showing that the Onsager relation is obeyed in hBN/graphene/YIG. (f) Landau level fan diagram where the dashed lines are calculated results. All data is at 9 K.

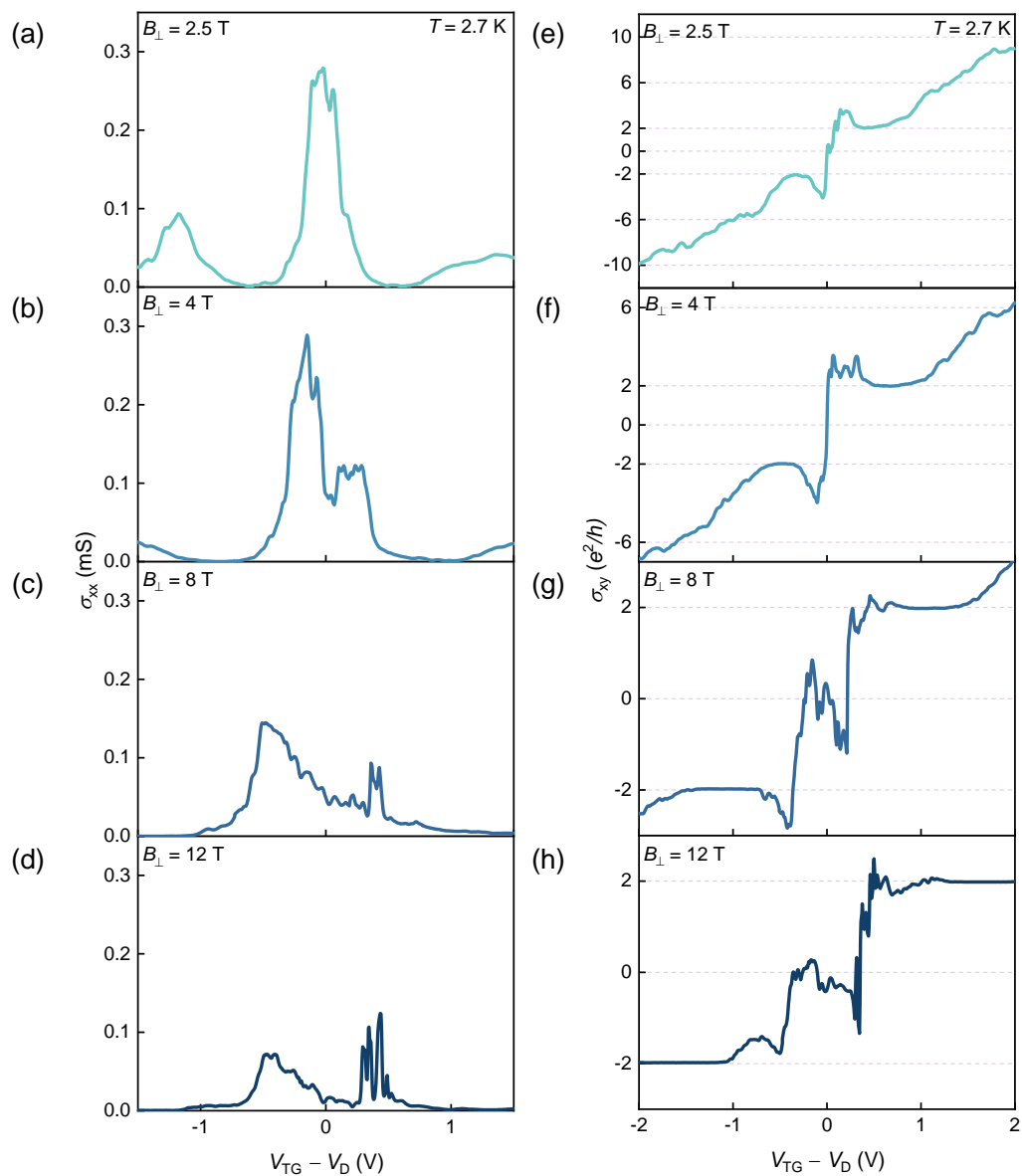


Fig. 10.8 (a)-(d) The gate-voltage-dependence of the longitudinal conductance ( $\sigma_{xx}$ ) for increasing values of  $B_{\perp}$  (labelled) and (e)-(h) the corresponding Hall conductance ( $\sigma_{xy}$ ) over the same magnetic field range at 2.7 K.

zero in 12 T. Over the same magnetic field range at  $V_D$ ,  $R_{xx}$  rapidly increases [Figure 10.9] indicating a transition to a gapped bulk state. Simultaneously the Hall conductance  $\sigma_{xy}$  tends to a plateau establishing the  $\nu = 0$  state [Figures 10.8(e)-(h)].

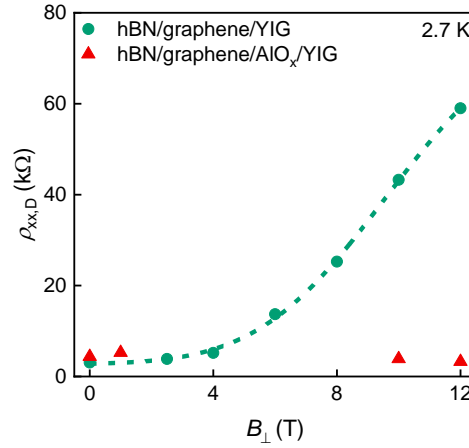


Fig. 10.9 Longitudinal resistivity at the Dirac point ( $\rho_{xx,D}$ ) versus  $B_{\perp}$  for hBN/graphene Hall bar on YIG and the hBN/graphene/ $\text{AlO}_x$ /YIG control Hall bar at 2.7 K. The green dashed curve is a guide to the eye.

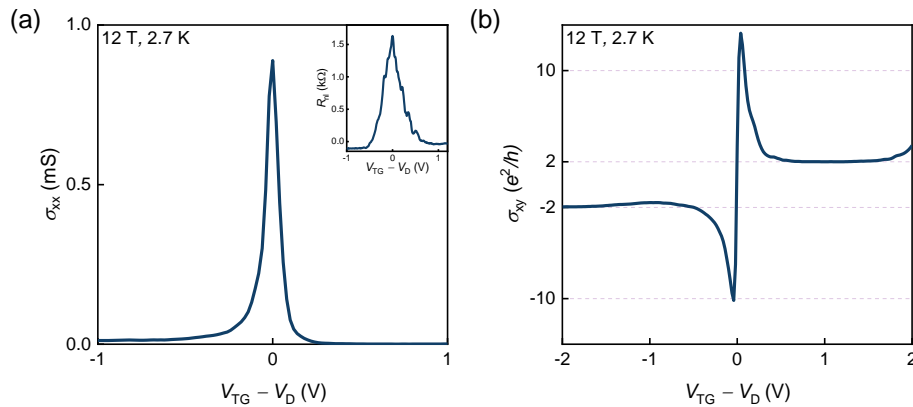


Fig. 10.10 Nonlocal and local measurements in hBN/graphene/ $\text{AlO}_x$ /YIG control Hall bar. (a)  $\sigma_{xx}$  versus  $V_{\text{TG}} - V_D$  in  $B_{\perp} = 12$  T. The inset shows  $R_{\text{nl}}$  versus  $V_{\text{TG}} - V_D$ . (b)  $\sigma_{xy}$  versus  $V_{\text{TG}} - V_D$  in  $B_{\perp} = 12$  T, which shows the plateaus of conductance corresponding to  $\nu = \pm 2$ .

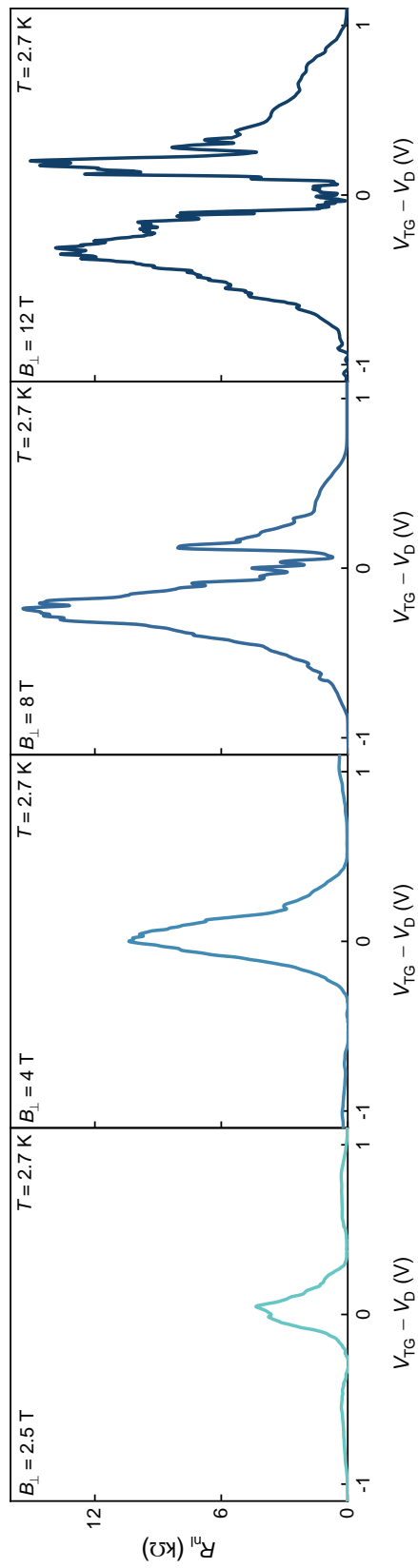


Fig. 10.11 Gate-voltage-dependence of  $R_{nl}$  for  $B_{\perp} = 2.5$  T to 12 T (labelled) in hBN/graphene/YIG at 2.7 K.

Equivalent measurements on the hBN/graphene/ $\text{AlO}_x$ /YIG control Hall bar are shown in Figure 10.10. In  $B_\perp = 12$  T, both  $\sigma_{xx}$  and  $R_{nl}$  show a single peak at  $V_D$  [Figure 10.10(a)], and the  $\sigma_{xy}$  versus  $V_{TG} - V_D$  only shows plateaus corresponding to  $\nu = \pm 2$  [Figure 10.10(b)], but the  $\nu = 0$  plateau and a splitting in  $\sigma_{xx}$  do not appear. Also control Hall bar does not show a transition to an insulating state in Figure 10.9. These results indicate that a coupling between graphene and YIG reduces the values of  $B_\perp$  required to achieve the  $\nu = 0$  state.

The  $\nu = 0$  state in Figure 10.8 could be a F or a CAF state. These are distinguishable from the gate-voltage-dependence of  $R_{nl}$  with  $B_\perp$  as shown in Figure 10.11. The transition from a single to a double peak in  $R_{nl}$  with gate voltage suggests that the  $\nu = 0$  state is associated with a transition from F to CAF state. Although consistent with theory [240], the transition occurs in graphene at lower values of  $B_\perp$  than without YIG ( $> 15$  T in Ref. [244]). Furthermore, the decrease in  $R_{nl}$  at  $V_D$  with increasing  $B_\perp$  suggests an increase in the edge gap and the angle between  $\vec{M}_T$  and the sublattice spins. This angle increases with  $B_\perp$  because the valley anisotropy energy (resulted from electron-electron Coulomb interactions which lead to an AF state) increases faster than the Zeeman energy as discussed in Appendix B.

#### 10.4.4 Nonlocal transports with rotating magnetic field

In order to confirm the magnetic states at  $\nu = 0$ , nonlocal measurements with rotating magnetic field ( $\vec{B}$ ,  $B = |\vec{B}|$ ) from  $B_\perp$  ( $\alpha = 90^\circ$ ) to  $B_\parallel$  ( $\alpha = 0^\circ$ ) are performed on an equivalent hBN/graphene Hall bar on YIG ( $\mu \sim 10,000 \text{ cm}^2 \text{ V}^{-1} \text{ s}^{-1}$  at 9 K) (Figure 10.12). The rotating magnetic field partially ( $6 \text{ T} < B < 12 \text{ T}$ ) or fully ( $B = 12 \text{ T}$ ) transforms the CAF to F state. When a fixed magnitude of  $\vec{B}$  rotates from out-of-plane to in-plane direction,  $B_\perp$  decreases and the sublattice spins align to  $\vec{M}_T$  reducing the size of edge gap and increasing  $R_{nl,D}$ . A maximum in  $R_{nl,D}$  reaches at the phase transition from CAF to F state where the edge gap vanishes. When  $\vec{B}$  is close to in-plane direction,  $B_\perp$  is too small to achieve the quantum Hall regime in the Hall bar.

Transitions between CAF and fully spin-polarized F states were investigated in Ref. [244] using hBN/graphene Hall bars with a rotating  $\vec{B}$  of up to 35 T at 300 mK. In that work the graphene was not in contact with a magnetic substrate meaning  $\vec{M}_{ex} = 0$  and thus  $\vec{M}_T = \vec{B}_Z$ . By extracting the values of  $M_T = |\vec{M}_T|$  reported in Ref. [244] versus  $B_\perp$ , a phase transition line of  $M_T \approx 9.9B_\perp + 4.9$  (see Appendix B for details) between the CAF and F states are shown in Figure 10.13. For hBN/graphene Hall bar on YIG (Figure 10.12), a transition between the CAF and F states occurs from  $B_\perp > 6$  T. By comparing with Ref. [244] and using  $\vec{M}_T = \vec{M}_{ex} + \frac{g}{2}\vec{B}$ ,  $|M_{ex}|$  induced by YIG in graphene is estimated to be of the order of

60 T due to the magnetic proximity effect. This estimate assumes that  $|M_{ex}|$  is independent of  $\vec{B}$  as long as  $|\vec{B}|$  is enough to fully magnetize YIG.

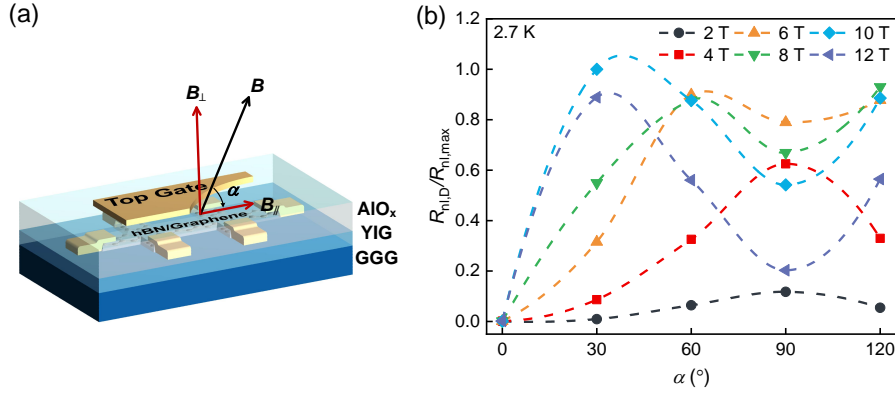


Fig. 10.12 Nonlocal measurements with rotating magnetic fields. (a) Schematic illustration of the hBN/graphene Hall bar on YIG, where  $|\vec{B}| = \sqrt{B_{\perp}^2 + B_{\parallel}^2}$  and  $\alpha$  is the angle between  $\vec{B}$  and the graphene surface. (b)  $R_{nl,D}/R_{nl,max}$  versus  $\alpha$  for  $\vec{B}$  from 2 to 12 T. Dashed lines are a guide to the eye. A  $\pm 5^\circ$  operational error due to manual rotation of the sample holder leads to the small asymmetry in  $R_{nl,D}$  at  $60^\circ$  and  $120^\circ$ .

A phase diagram schematically illustrated in Figure 10.14, where magnetic fields cause a phase transition between F and CAF state. For small  $B_{\perp}$ , the quantum Hall state is not well-developed. By increasing  $B_{\perp}$ , there exists a competition between F and CAF state. For reasonably small  $B_{\perp}$  and large  $M_T$ , the F state is realized, whereas by increasing the ratio of  $(B_{\perp}/M_T)$ , the CAF state becomes energetically favoured. The magnetic order and the energy gap of the edge modes in graphene can be controlled by the magnitude ( $> 6$  T) and the direction of  $\vec{B}$ . The required magnitude of  $\vec{B}$  is smaller than that in the absence of magnetic exchange field ( $> 15$  T) [244].

The polar angle ( $\theta$ ) can be varied by rotating the direction of  $\vec{B}$ . Figure 10.15 plots  $\theta$  as a function of  $B$  and  $\alpha$  (the angle between the applied magnetic field and sample surface,  $B_{\perp} = B\sin\alpha$  and  $B_{\parallel} = B\cos\alpha$ ). In the presence of proximity-induced magnetic exchange field [Figure 10.15(a)], if  $B$  is constant, varying the  $\alpha$  from  $\pi/2$  to 0 firstly causes a transition from CAF to F state, then by further decreasing  $\alpha$  the system is driven away from the quantum Hall regime because  $B_{\perp}$  decreases. But in the absence of magnetic exchange field [Figure 10.15(b)], it needs a very large magnitude of  $\vec{B}$  or a very small  $\alpha$  in order to access the regime where  $\theta$  can be changed substantially. Magnetic exchange field lowers the energy of both CAF and F states. In the CAF state, magnetic exchange field decreases the energy as  $-\delta E \propto M_T^2/u(B_{\perp})$  and in the F state as  $-\delta E \propto M_T$ .

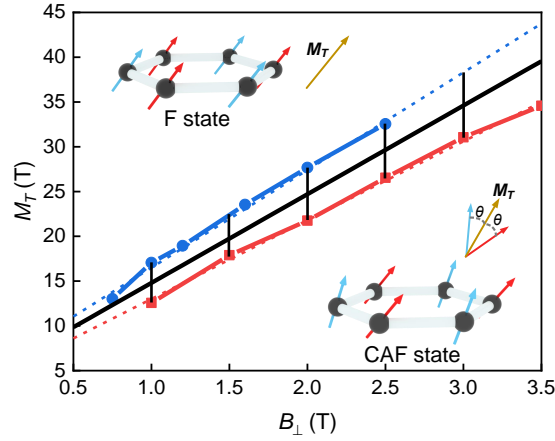


Fig. 10.13 Phase transition line between F and CAF states as a function of  $B_{\perp}$  in hBN/graphene Hall bar at 300 mK. Blue line for  $M_T \approx 10.9B_{\perp} + 5.6$  and red line for  $M_T \approx 8.8B_{\perp} + 4.2$ , which are calculated from the Ref. [244] experiment results. Black line for  $M_T \approx 9.9B_{\perp} + 4.9$  is an estimation for the phase transition in graphene on YIG, which is the average of the blue and red lines.

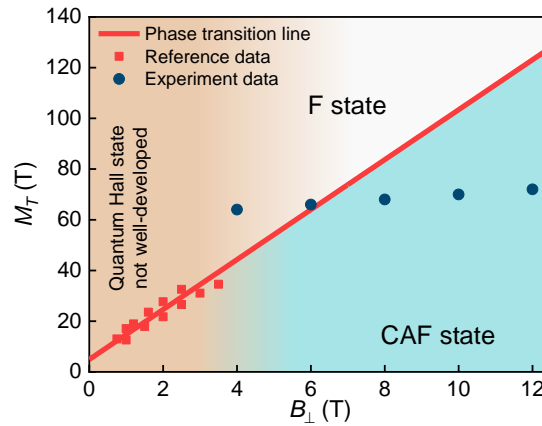


Fig. 10.14 Magnetic phase diagram in ( $M_T$  versus  $B_{\perp}$ ) for hBN/graphene Hall bar on YIG. The solid (red) line  $M_T \approx 9.9B_{\perp} + 4.9$  is calculated from Ref. [244] using the extracted data in red. The blue data represent the estimated  $M_T$  for hBN/graphene Hall bar on YIG with  $B_{\perp}$  only. All data is at 2.7 K except the data from Ref. [244] which is at 300 mK.

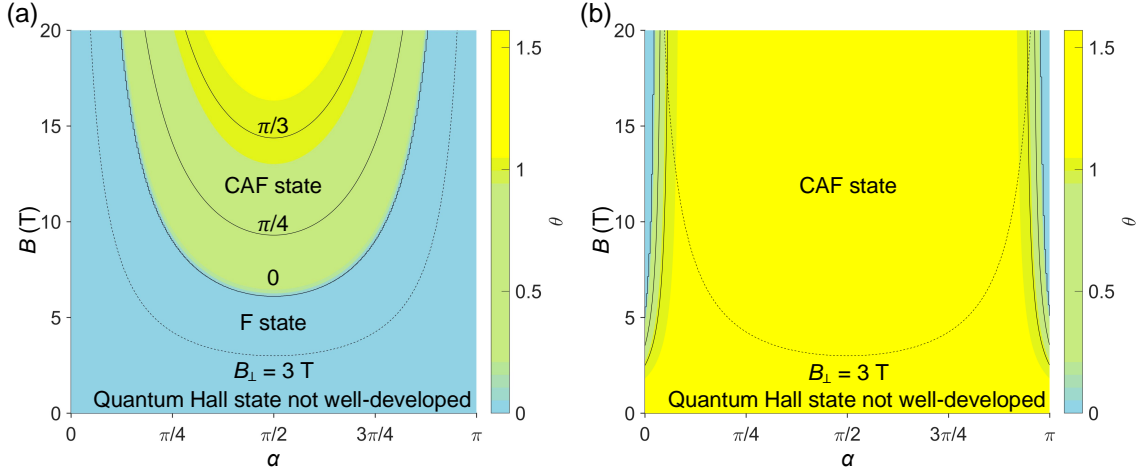


Fig. 10.15 The polar angle  $\theta$  as a function of  $B$  and  $\alpha$  in graphene for (a)  $M_{ex} = 60$  T and (b)  $M_{ex} = 0$ . The dashed line indicates  $B_{\perp} = 3$  T. Below this line, the quantum Hall state is not well-developed in the Hall bar.

## 10.5 Energy gap of the edge modes

The low-energy edge excitations in this type of quantum Hall systems are collective [145, 251, 252]. The properties of these collective excitations are different from the single-particle excitations. An estimation of the energy gap of the edge modes can be obtained using a simplified mean-field single-particle approach proposed in Ref. [240].

In the AF state the bulk and edge modes are gapped, whereas in the F state the bulk mode is gapped but gapless counter-propagating edge mode (protected by spin-rotation symmetry) appears at the edge. As the CAF state is a mixture of the AF state ( $\theta = \pi/2$ ) and F state ( $\theta = 0$ ), the edge gap has to gradually decrease when  $\theta$  decreases from  $\pi/2$  to 0. This behavior is described by the mean-field Hamiltonian [240],

$$\mathcal{H} = -\xi(k_x)\tau_x\sigma_0 - (\mu_B M_T + \Delta_z)\tau_0\sigma_z - \Delta_x\tau_z\sigma_x, \quad (10.1)$$

where Pauli matrices  $\tau_i$  and  $\sigma_i$  operate on the valley and spin degrees of freedom, respectively, and the spin quantization axis ( $z$ -direction in the spin space) has been chosen to be along the direction of the applied magnetic field.  $\Delta_x$  and  $\Delta_z$  are the Hartree-Fock mean field potentials due to electron-electron interactions. Here  $M_T = |\vec{M}_T|$ ,  $\xi(k_x)$  describes the dispersion of the Landau levels and  $k_x$  is the momentum along the  $x$ -direction of the edge, which is related to the position  $y_{k_x} = k_x l_B^2$  perpendicular to the edge in Landau gauge. When  $y_{k_x}$  is deep inside the bulk,  $\xi(k_x) = 0$ . When  $y_{k_x}$  approaches the edge,  $\xi(k_x)$  increases. In addition, the

mean-field potential is obtained by decoupling the interactions,

$$\Delta_z = 2V_z(B_\perp)\cos\theta, \Delta_x = 2V_x(B_\perp)\sin\theta, \quad (10.2)$$

where  $\Delta_z$  and  $\Delta_x$  are the mean-field potentials,  $V_z$  and  $V_x$  are the effective interaction strengths.  $\Delta_z$  arises due to the spin-component of the electrons parallel to  $\vec{M}_T$ , and  $\Delta_x$  is due to spin-component perpendicular to  $\vec{M}_T$  pointing in opposite directions. The spatial dependence of the  $\Delta_z$  and  $\Delta_x$  are neglected.  $V_z(B_\perp)$  and  $V_x(B_\perp)$  increase with increasing  $B_\perp$  and the related anisotropy energy is

$$u(B_\perp) = V_x(B_\perp) - V_z(B_\perp). \quad (10.3)$$

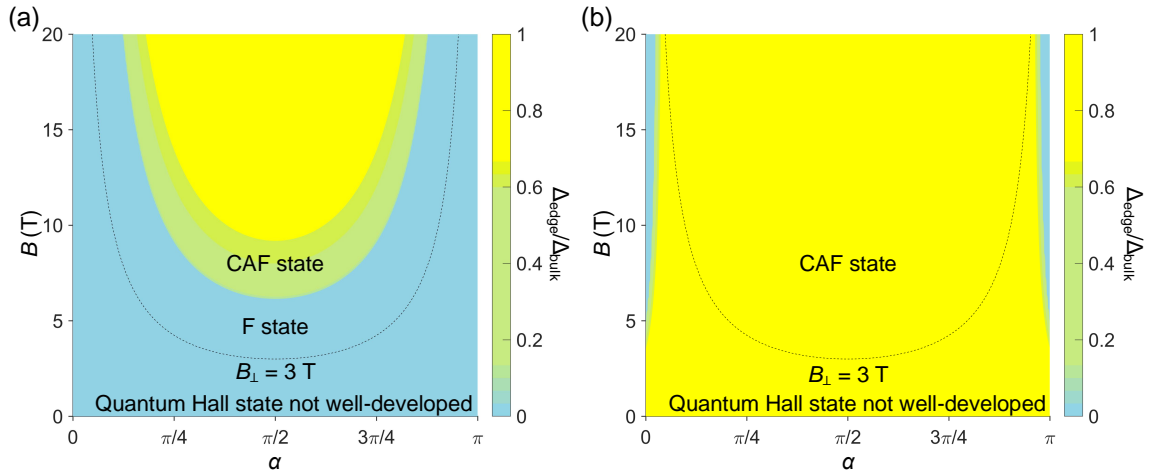


Fig. 10.16 The energy gap of the edge modes ( $\Delta_{\text{edge}}$ ) as a function of  $B$  and  $\alpha$  in graphene for (a)  $M_{ex} = 60$  T and (b)  $M_{ex} = 0$ . The dashed line indicates  $B_\perp = 3$  T. Below this line, the quantum Hall state is not well-developed in the Hall bar.

Moreover,  $V_x(B_\perp)$  is directly related to the bulk gap ( $\Delta_{\text{bulk}}$ ) in the AF and CAF states, i.e.  $\Delta_{\text{bulk}} = 4V_x(B_\perp)$ . Therefore  $V_x(B_\perp)$  could be estimated using the thermal activation gap measured in the experiments, and  $V_z(B_\perp)$  could be determined using Equations (B.4) and (10.3). In Ref. [243], the thermal activation gap increases approximately linearly with  $B_\perp$ , so that  $V_z(B_\perp)$ ,  $V_x(B_\perp)$  and  $u(B_\perp)$  all linearly depend on  $B_\perp$  in the applied range of magnetic fields. The edge gap ( $\Delta_{\text{edge}}$ ) can be described in the units of  $\Delta_{\text{bulk}}$ , so the exact values of  $V_z(B_\perp)$  and  $V_x(B_\perp)$  are not required.

According to the energy spectrum from the Hamiltonian in Equation (10.1),  $\Delta_{\text{edge}}$  is given by

$$\Delta_{\text{edge}} = \begin{cases} 0, & \mu_B M_T > 2u(B_\perp) \quad (\text{F state}) \\ \Delta_{\text{bulk}} \sin\theta, & \mu_B M_T < 2u(B_\perp) \quad (\text{CAF state}) \end{cases}. \quad (10.4)$$

In the AF state,  $\Delta_{\text{edge}} = \Delta_{\text{bulk}}$  ( $\theta = \pi/2$ ).  $\Delta_{\text{edge}} \rightarrow 0$  when it is F state ( $\theta \rightarrow 0$ ). Furthermore, in the presence of magnetic exchange field [Figure 10.16(a)], it is able to control  $\Delta_{\text{edge}}$  with the direction and relatively small magnitude of  $\vec{B}$ . In the absence of magnetic exchange field [Figure 10.16(b)], the edge gap satisfies  $\Delta_{\text{edge}} \approx \Delta_{\text{bulk}}$  unless very large magnetic field is applied.

## 10.6 Summary and future work

In summary, an intrinsic magnetic exchange field in hBN covered graphene on YIG of the order 60 T is demonstrated experimentally and theoretically. The magnetic order and the energy gap of the edge modes in graphene can be tuned more efficiently than in the absence of YIG by varying the magnitude ( $> 6$  T) and direction of magnetic field at 2.7 K. In particular, out-of-plane magnetic field induces a transition between F and CAF  $\nu = 0$  quantum Hall states in graphene on YIG. This achievement is important for the development two-dimensional materials with magnetic field tunable ordered states of matter.

### Quantum anomalous Hall effect in graphene

The development of spintronic devices relies on efficient generation of spin-polarized currents and their electric-field-controlled manipulation. While observation of exceptionally long spin relaxation length of  $24 \mu\text{m}$  [253] makes graphene a promising material for spintronics, electric-field-modulation of spin currents is almost impossible due to the weak spin-orbit coupling. The presence of strong spin-orbit coupling along with broken time reversal symmetry is a necessary condition for achieving quantum anomalous Hall effect in graphene [23, 254]. However, semiconducting transition metal dichalcogenides (TMDs) exhibit strong spin-orbit coupling [255]. It was demonstrated that spin-orbit coupling in graphene can be enhanced by the proximity effect from  $\text{WS}_2$  (5-17 meV) [127, 192] and  $\text{WSe}_2$  (0.2-1.0 meV) [256, 257]. A heterostructure of hBN/TMD/graphene/YIG will be investigated by local and nonlocal transport measurements to demonstrate the possibility of realizing quantum anomalous Hall effect in graphene.

### Graphene on alternative ferromagnetic insulator garnet

The shape anisotropy in YIG favours in-plane direction and the out-of-plane anisotropy is quite weak. Out-of-plane magnetic anisotropy is essential for graphene to realize quantum anomalous Hall effect [258]. Thulium iron garnet (TmIG) has an out-of-plane easy axis [259], which is an alternative choice to induce a magnetic exchange field in graphene by proximity

---

effect. The growth of TmIG thin films is similar to YIG on GGG by pulsed laser deposition. A heterostructure of hBN/graphene/TmIG will be investigated.



# Chapter 11

## Thesis summary

This thesis has introduced and investigated two graphene-based hybrid systems, focusing on the transport properties of graphene/hBN superlattice and graphene on insulating ferrimagnetic substrates Hall bars.

1. Graphene-based device fabrication and characterization methods have been investigated. Thin flake transfer techniques including wet and dry methods have been optimized and adapted on the transparent substrates like YIG and GGG. Raman spectroscopy is used to investigate electronic and structural properties of graphene. All samples do not show structural defects and exhibit low charge impurities with the help of top hBN layer encapsulation. Hall bar fabrication techniques, including thermal deposition, electron beam lithography, reactive ion etcher, electron beam deposition and atomic layer deposition, have been optimized. Hall bar shaping with metal mask and side-contacts deposition methods have been developed. Aligned hBN/graphene/hBN superlattice and hBN/graphene/YIG Hall bars with top-gate are fabricated with field-effect mobility of up to  $220,000 \text{ cm}^2 \text{ V}^{-1} \text{ s}^{-1}$  and  $12,000 \text{ cm}^2 \text{ V}^{-1} \text{ s}^{-1}$  at 9 K, respectively. An electrical transport measurement setup, including lock-in amplifiers and LabVIEW interface, is developed, which can simultaneously measure up to five input signals with the dependence of temperature and magnetic field.
2. The growth parameters of YIG thin films in a pulsed laser deposition system are investigated. Both atomic force microscopy and room temperature vibrating sample magnetometer measurements are performed to confirm the surface roughness and magnetism of YIG thin films. High quality 50-80 nm YIG thin films with less than 0.2 nm roughness, in-plane anisotropy and bulk-like magnetic properties have been epitaxially layer-by-layer grown on both (110) and (111)-oriented GGG substrates.

3. Nonlocal transport measurement shows its advantage in detecting subtle non-trivial electronic interactions. Extrinsic contributions to nonlocal resistance may come from Ohmic effect, Joule effect, and Nernst-Ettingshausen effect. Ohmic contribution can be calculated by van der Pauw formula. Thermal contributions can be ruled out by measuring both first and second harmonic nonlocal signals. Intrinsic origins of nonlocal resistance include spin Hall effect, Zeeman spin Hall effect, valley Hall effect and edge state transport. Spin Hall effect requires spin-orbit coupling. Zeeman spin Hall effect depends on both orbital effect and Zeeman effect. Valley Hall effect arises from nonzero Berry curvature which requires graphene inversion symmetry is broken. Landauer-Büttiker formalism is used to calculate transmission probability in edge state transport.
4. Hall bar devices are employed to study the properties of hBN/graphene/hBN superlattice. Aligned hBN/graphene/hBN Hall bar is fabricated by van der Waals assembly with side-contacts. Graphene Raman 2D peak is sensitive to the alignment angle ( $\varphi$ ) between graphene and hBN. A 33.7 meV band gap at the primary Dirac point and secondary Dirac points are observed in hBN/graphene/hBN Hall bar with  $\varphi < 1^\circ$ . The carrier density dependence of nonlocal resistance shows negative values, which indicates a ballistic character of device. A  $\nu = 0$  state appears in longitudinal and Hall conductances when the gate voltage is near the Dirac point. The temperature dependence of longitudinal resistance is studied to estimate the band gap. The band gap in graphene superlattice at commensurate state is larger than at incommensurate state. In zero magnetic field, a nonlocal resistance close to  $h/2e^2$  is observed at the Dirac point and decays nonlocally over distance of 15  $\mu\text{m}$ . At high temperature ( $T > 60$  K), nonlocal resistance originates from bulk valley current due to graphene's nonzero Berry curvature, meaning that the inversion symmetry in graphene is broken. At low temperature ( $T < 60$  K), a spin-degenerate ballistic counter-propagating edge state is dominant in nonlocal signal. But there may be a secondary contribution from a network of one-dimensional conducting channels at the narrow soliton-like domain walls.
5. hBN/graphene Hall bars on the ferrimagnetic insulator YIG are characterized with Raman spectroscopy before and after transfer process. No observable D peak is present in the Raman spectra, which indicates that the transfer process does not induce defects in graphene. The Hall bar device is fabricated in the region which is clean selected by Raman spectra maps. At low temperature, a substantial nonlocal resistance peak is observed in zero magnetic field, which indicates the Zeeman spin Hall effect

contribution. The out-of-plane magnetic field dependence of the local and nonlocal resistances are studied. The observations of Shubnikov-de Haas oscillations, ultra sharp nonlocal peak and Onsager relation for nonlocal resistance demonstrate that a proximity-induced magnetic exchange field in graphene on YIG. In high magnetic fields, a metal to insulator transition occurs, which is consistent with appearance of the  $\nu = 0$  plateau. At the same time, a double-peak structure with increasing out-of-plane magnetic field occurs in nonlocal resistance, which indicates a transition from a ferromagnetic to a canted antiferromagnetic state. Compared with earlier reported results, the value of magnetic exchange field in graphene on YIG is estimated to be the order of 60 T. From measurement results, the magnetic order and the energy gap of the edge modes in graphene on YIG can be controlled by lower magnitude of magnetic field ( $> 6$  T) than in the absence of YIG ( $> 15$  T), also can be tuned by rotating the direction of magnetic field.



# References

- [1] G. E. Moore. Cramming more components onto integrated circuits. *Electronics* **38**, 114 (1965).
- [2] B. Prince. *Vertical 3D memory technologies* (John Wiley & Sons, 2014).
- [3] E. Sicard. Introducing 7-nm FinFET technology in Microwind (2017).
- [4] F. Schwierz. Graphene transistors. *Nat. Nanotechnol.* **5**, 487–496 (2010).
- [5] P. Avouris, Z. Chen & V. Perebeinos. Carbon-based electronics. *Nat. Nanotechnol.* **2**, 605–615 (2007).
- [6] D. G. Purdie, N. M. Pugno, T. Taniguchi, K. Watanabe, A. C. Ferrari & A. Lombardo. Cleaning interfaces in layered materials heterostructures. *Nat. Commun.* **9**, 5387 (2018).
- [7] K. S. Novoselov, A. K. Geim, S. V. Morozov, D. Jiang, Y. Zhang, S. V. Dubonos, I. V. Grigorieva & A. A. Firsov. Electric field effect in atomically thin carbon films. *Science* **306**, 666–669 (2004).
- [8] J. B. Oostinga, H. B. Heersche, X. Liu, A. F. Morpurgo & L. M. K. Vandersypen. Gate-induced insulating state in bilayer graphene devices. *Nat. Mater.* **7**, 151–157 (2008).
- [9] F. Xia, D. B. Farmer, Y. Lin & P. Avouris. Graphene field-effect transistors with high on/off current ratio and large transport band gap at room temperature. *Nano Lett.* **10**, 715–718 (2010).
- [10] Y. Zhang, T. Tang, C. Girit, Z. Hao, M. C. Martin, A. Zettl, M. F. Crommie, Y. R. Shen & F. Wang. Direct observation of a widely tunable bandgap in bilayer graphene. *Nature* **459**, 820–823 (2009).
- [11] Y. Son, M. L. Cohen & S. G. Louie. Energy gaps in graphene nanoribbons. *Phys. Rev. Lett.* **97**, 216803 (2006).
- [12] M. Y. Han, B. Özyilmaz, Y. Zhang & P. Kim. Energy band-gap engineering of graphene nanoribbons. *Phys. Rev. Lett.* **98**, 206805 (2007).
- [13] L. Yang, C. Park, Y. Son, M. L. Cohen & S. G. Louie. Quasiparticle energies and band gaps in graphene nanoribbons. *Phys. Rev. Lett.* **99**, 186801 (2007).

- [14] J. J. Baldoví, S. Cardona-Serra, A. Gaita-Ariño & E. Coronado. *Design of magnetic polyoxometalates for molecular spintronics and as spin qubits*, vol. 69 of *Advances in Inorganic Chemistry*, 213–249 (Elsevier, 2017).
- [15] S. Roche, J. Åkerman, B. Beschoten, J. Charlier, M. Chshiev, S. Prasad Dash, B. Dlubak, J. Fabian, A. Fert, M. Guimarães, F. Guinea, I. Grigorieva, C. Schönenberger, P. Seneor, C. Stampfer, S. O. Valenzuela, X. Waintal & B. van Wees. Graphene spintronics: the European Flagship perspective. *2D Mater.* **2**, 030202 (2015).
- [16] D. Xiao, G.-B. Liu, W. Feng, X. Xu & W. Yao. Coupled spin and valley physics in monolayers of MoS<sub>2</sub> and other group-VI dichalcogenides. *Phys. Rev. Lett.* **108**, 196802 (2012).
- [17] A. Rycerz, J. Tworzydło & C. W. J. Beenakker. Valley filter and valley valve in graphene. *Nat. Phys.* **3**, 172–175 (2007).
- [18] D. Xiao, W. Yao & Q. Niu. Valley-contrasting physics in graphene: Magnetic moment and topological transport. *Phys. Rev. Lett.* **99**, 236809 (2007).
- [19] L. A. Ponomarenko, R. V. Gorbachev, G. L. Yu, D. C. Elias, R. Jalil, A. A. Patel, A. Mishchenko, A. S. Mayorov, C. R. Woods, J. R. Wallbank, M. Mucha-Kruczynski, B. A. Piot, M. Potemski, I. V. Grigorieva, K. S. Novoselov, F. Guinea, V. I. Fal'ko & A. K. Geim. Cloning of Dirac fermions in graphene superlattices. *Nature* **497**, 594–597 (2013).
- [20] B. Hunt, J. D. Sanchez-Yamagishi, A. F. Young, M. Yankowitz, B. J. LeRoy, K. Watanabe, T. Taniguchi, P. Moon, M. Koshino, P. Jarillo-Herrero & R. C. Ashoori. Massive Dirac fermions and Hofstadter butterfly in a van der Waals heterostructure. *Science* **340**, 1427–1430 (2013).
- [21] C. R. Dean, L. Wang, P. Maher, C. Forsythe, F. Ghahari, Y. Gao, J. Katoch, M. Ishigami, P. Moon, M. Koshino, T. Taniguchi, K. Watanabe, K. L. Shepard, J. Hone & P. Kim. Hofstadter's butterfly and the fractal quantum Hall effect in moiré superlattices. *Nature* **497**, 598–602 (2013).
- [22] M. Lee, J. R. Wallbank, P. Gallagher, K. Watanabe, T. Taniguchi, V. I. Falko & D. Goldhaber-Gordon. Ballistic miniband conduction in a graphene superlattice. *Science* **353**, 1526–1529 (2016).
- [23] Z. Wang, C. Tang, R. Sachs, Y. Barlas & J. Shi. Proximity-induced ferromagnetism in graphene revealed by the anomalous Hall effect. *Phys. Rev. Lett.* **114**, 016603 (2015).
- [24] J. C. Leutenantsmeyer, A. A. Kaverzin, M. Wojtaszek & B. J. van Wees. Proximity induced room temperature ferromagnetism in graphene probed with spin currents. *2D Mater.* **4**, 014001 (2016).
- [25] A. A. Balandin, S. Ghosh, W. Bao, I. Calizo, D. Teweldebrhan, F. Miao & C. N. Lau. Superior thermal conductivity of single-layer graphene. *Nano Lett.* **8**, 902–907 (2008).

- [26] A. S. Mayorov, R. V. Gorbachev, S. V. Morozov, L. Britnell, R. Jalil, L. A. Ponomarenko, P. Blake, K. S. Novoselov, K. Watanabe, T. Taniguchi & A. K. Geim. Micrometer-scale ballistic transport in encapsulated graphene at room temperature. *Nano Lett.* **11**, 2396–2399 (2011).
- [27] K. Zhang, Y. Feng, F. Wang, Z. Yang & J. Wang. Two dimensional hexagonal boron nitride (2D-hBN): synthesis, properties and applications. *J. Mater. Chem. C* **5**, 11992–12022 (2017).
- [28] R. Saito, G. Dresselhaus & M. S. Dresselhaus. *Physical properties of carbon nanotubes* (Imperial College Press, London, 1998).
- [29] P. R. Wallace. The band theory of graphite. *Phys. Rev.* **71**, 622–634 (1947).
- [30] V. N. Kotov, B. Uchoa, V. M. Pereira, F. Guinea & A. H. Castro Neto. Electron-electron interactions in graphene: Current status and perspectives. *Rev. Mod. Phys.* **84**, 1067–1125 (2012).
- [31] A. H. Castro Neto, F. Guinea, N. M. R. Peres, K. S. Novoselov & A. K. Geim. The electronic properties of graphene. *Rev. Mod. Phys.* **81**, 109–162 (2009).
- [32] T. Ando, T. Nakanishi & R. Saito. Berry's phase and absence of back scattering in carbon nanotubes. *J. Phys. Soc. Japan* **67**, 2857–2862 (1998).
- [33] S. V. Morozov, K. S. Novoselov, M. I. Katsnelson, F. Schedin, D. C. Elias, J. A. Jaszczak & A. K. Geim. Giant intrinsic carrier mobilities in graphene and its bilayer. *Phys. Rev. Lett.* **100**, 016602 (2008).
- [34] G. Bergman. Weak localization in thin films. *Physics Rep.* **107**, 1–58 (1984).
- [35] S. Chakravarty & A. Schmid. Weak localization: The quasiclassical theory of electrons in a random potential. *Physics Reports* **140**, 193–236 (1986).
- [36] A. C. Ferrari & D. M. Basko. Raman spectroscopy as a versatile tool for studying the properties of graphene. *Nat. Nanotechnol.* **8**, 235–246 (2013).
- [37] A. C. Ferrari, J. C. Meyer, V. Scardaci, C. Casiraghi, M. Lazzeri, F. Mauri, S. Piscanec, D. Jiang, K. S. Novoselov, S. Roth & A. K. Geim. Raman spectrum of graphene and graphene layers. *Phys. Rev. Lett.* **97**, 187401 (2006).
- [38] A. C. Ferrari. Raman spectroscopy of graphene and graphite: Disorder, electron-phonon coupling, doping and nonadiabatic effects. *Solid State Commun.* **143**, 47–57 (2007).
- [39] P. May, M. Lazzeri, P. Venezuela, F. Herziger, G. Callsen, J. S. Reparaz, A. Hoffmann, F. Mauri & J. Maultzsch. Signature of the two-dimensional phonon dispersion in graphene probed by double-resonant Raman scattering. *Phys. Rev. B* **87**, 075402 (2013).
- [40] F. Bonaccorso, P.-H. Tan & A. C. Ferrari. Multiwall nanotubes, multilayers, and hybrid nanostructures: New frontiers for technology and Raman spectroscopy. *ACS Nano* **7**, 1838–1844 (2013).

- [41] M. Bruna, A. K. Ott, M. Ijäs, D. Yoon, U. Sassi & A. C. Ferrari. Doping dependence of the Raman spectrum of defected graphene. *ACS Nano* **8**, 7432–7441 (2014).
- [42] A. Das, S. Pisana, B. Chakraborty, S. Piscanec, S. K. Saha, U. V. Waghmare, K. S. Novoselov, H. R. Krishnamurthy, A. K. Geim, A. C. Ferrari & A. K. Sood. Monitoring dopants by Raman scattering in an electrochemically top-gated graphene transistor. *Nat. Nanotechnol.* **3**, 210–215 (2008).
- [43] D. M. Basko, S. Piscanec & A. C. Ferrari. Electron-electron interactions and doping dependence of the two-phonon Raman intensity in graphene. *Phys. Rev. B* **80**, 165413 (2009).
- [44] A. Das, B. Chakraborty, S. Piscanec, S. Pisana, A. K. Sood & A. C. Ferrari. Phonon renormalization in doped bilayer graphene. *Phys. Rev. B* **79**, 155417 (2009).
- [45] S. Pisana, M. Lazzeri, C. Casiraghi, K. S. Novoselov, A. K. Geim, A. C. Ferrari & F. Mauri. Breakdown of the adiabatic Born–Oppenheimer approximation in graphene. *Nat. Mater.* **6**, 198–201 (2007).
- [46] J. Yan, Y. Zhang, P. Kim & A. Pinczuk. Electric field effect tuning of electron-phonon coupling in graphene. *Phys. Rev. Lett.* **98**, 166802 (2007).
- [47] T. M. G. Mohiuddin, A. Lombardo, R. R. Nair, A. Bonetti, G. Savini, R. Jalil, N. Bonini, D. M. Basko, C. Galotisi, N. Marzari, K. S. Novoselov, A. K. Geim & A. C. Ferrari. Uniaxial strain in graphene by Raman spectroscopy: G peak splitting, Grüneisen parameters, and sample orientation. *Phys. Rev. B* **79**, 205433 (2009).
- [48] K. Watanabe, T. Taniguchi & H. Kanda. Direct-bandgap properties and evidence for ultraviolet lasing of hexagonal boron nitride single crystal. *Nat. Mater.* **3**, 404–409 (2004).
- [49] M. Yankowitz, J. Xue, D. Cormode, J. D. Sanchez-Yamagishi, K. Watanabe, T. Taniguchi, P. Jarillo-Herrero, P. Jacquod & B. J. LeRoy. Emergence of superlattice Dirac points in graphene on hexagonal boron nitride. *Nat. Phys.* **8**, 382–386 (2012).
- [50] M. Ishigami, J. H. Chen, W. G. Cullen, M. S. Fuhrer & E. D. Williams. Atomic structure of graphene on SiO<sub>2</sub>. *Nano Lett.* **7**, 1643–1648 (2007).
- [51] C. H. Lui, L. Liu, K. F. Mak, G. W. Flynn & T. F. Heinz. Ultraflat graphene. *Nature* **462**, 339–341 (2009).
- [52] T. Kuzuba, K. Era, T. Ishii & T. Sato. A low frequency Raman-active vibration of hexagonal boron nitride. *Solid State Commun.* **25**, 863–865 (1978).
- [53] I. Stenger, L. Schué, M. Boukhicha, B. Berini, B. Plaçais, A. Loiseau & J. Barjon. Low frequency Raman spectroscopy of few-atomic-layer thick hBN crystals. *2D Mater.* **4**, 031003 (2017).
- [54] L. Schué, I. Stenger, F. Fossard, A. Loiseau & J. Barjon. Characterization methods dedicated to nanometer-thick hBN layers. *2D Mater.* **4**, 015028 (2016).

- [55] R. Arenal, A. C. Ferrari, S. Reich, L. Wirtz, J.-Y. Mevellec, S. Lefrant, A. Rubio & A. Loiseau. Raman spectroscopy of single-wall boron nitride nanotubes. *Nano Lett.* **6**, 1812–1816 (2006).
- [56] R. J. Nemanich, S. A. Solin & R. M. Martin. Light scattering study of boron nitride microcrystals. *Phys. Rev. B* **23**, 6348–6356 (1981).
- [57] S. Reich, A. C. Ferrari, R. Arenal, A. Loiseau, I. Bello & J. Robertson. Resonant Raman scattering in cubic and hexagonal boron nitride. *Phys. Rev. B* **71**, 205201 (2005).
- [58] R. V. Gorbachev, I. Riaz, R. R. Nair, R. Jalil, L. Britnell, B. D. Belle, E. W. Hill, K. S. Novoselov, K. Watanabe, T. Taniguchi, A. K. Geim & P. Blake. Hunting for monolayer boron nitride: Optical and Raman signatures. *Small* **7**, 465–468 (2011).
- [59] W. Heisenberg. Mehrkörperproblem und resonanz in der quantenmechanik. *Zeitschrift für Phys.* **38**, 411–426 (1926).
- [60] H. C. Siegmann & J. Stöhr. *Magnetism: From fundamentals to nanoscale dynamics* (Springer, Berlin, Germany, 2006).
- [61] S. Blundell. Magnetism in condensed matter: Oxford master series. *Condensed Matter Physics* (2001).
- [62] C. Tannous & J. Gieraltowski. *Magnetic properties: From traditional to spintronic*, vol. 10 (Springer, Cham, 2017).
- [63] W. Han, R. K. Kawakami, M. Gmitra & J. Fabian. Graphene spintronics. *Nat. Nanotechnol.* **9**, 794–807 (2014).
- [64] J. P. Jakubovics. *Magnetism and magnetic materials* (Institute of Materials, 1994).
- [65] W. Sucksmith, R. R. Pearce & A. M. Tyndall. The paramagnetism of the ferromagnetic elements. *Proc. R. Soc. London. Ser. A. Math. Phys. Sci.* **167**, 189–204 (1938).
- [66] C. Kittel. *Introduction to solid state physics* (Wiley, New York, 2004).
- [67] D. Jiles. *Introduction to magnetism and magnetic materials* (CRC press, 2015).
- [68] S. O. Kasap. *Principles of electronic materials and devices* (McGraw-Hill Education, 2005).
- [69] P. Wigen. Microwave properties of magnetic garnet thin films. *Thin Solid Films* **114**, 135–186 (1984).
- [70] F. Bertaut & F. Forrat. Structure des ferrites ferrimagnétiques des terres rares. *Comptes rendus hebdomadaires des seances de l'academie des sciences* **242**, 382–384 (1956).
- [71] S. Geller & M. A. Gilleo. Structure and ferrimagnetism of yttrium and rare-earth–iron garnets. *Acta Crystallogr.* **10**, 239–239 (1957).
- [72] Y. Sun. *Yttrium iron garnet nano films: Epitaxial growth, damping, spin pumping, and magnetic proximity effect*. Ph.D. thesis.

- [73] B. Lax & K. J. Button. *Microwave ferrites and ferrimagnetics* (McGraw-Hill, New York, 1962).
- [74] Y. Kajiwara, K. Harii, S. Takahashi, J. Ohe, K. Uchida, M. Mizuguchi, H. Umezawa, H. Kawai, K. Ando, K. Takanashi, S. Maekawa & E. Saitoh. Transmission of electrical signals by spin-wave interconversion in a magnetic insulator. *Nature* **464**, 262–266 (2010).
- [75] L. A. Ponomarenko, A. K. Geim, A. A. Zhukov, R. Jalil, S. V. Morozov, K. S. Novoselov, I. V. Grigorieva, E. H. Hill, V. V. Cheianov, V. I. Fal'ko, K. Watanabe, T. Taniguchi & R. V. Gorbachev. Tunable metal–insulator transition in double-layer graphene heterostructures. *Nat. Phys.* **7**, 958–961 (2011).
- [76] K. S. Novoselov, D. Jiang, F. Schedin, T. J. Booth, V. V. Khotkevich, S. V. Morozov & A. K. Geim. Two-dimensional atomic crystals. *Proc. Natl. Acad. Sci.* **102**, 10451–10453 (2005).
- [77] T. Ando. Screening effect and impurity scattering in monolayer graphene. *J. Phys. Soc. Japan* **75**, 074716 (2006).
- [78] E. H. Hwang, S. Adam & S. D. Sarma. Carrier transport in two-dimensional graphene layers. *Phys. Rev. Lett.* **98**, 186806 (2007).
- [79] J.-H. Chen, C. Jang, S. Xiao, M. Ishigami & M. S. Fuhrer. Intrinsic and extrinsic performance limits of graphene devices on SiO<sub>2</sub>. *Nat. Nanotechnol.* **3**, 206–209 (2008).
- [80] S. Fratini & F. Guinea. Substrate-limited electron dynamics in graphene. *Phys. Rev. B* **77**, 195415 (2008).
- [81] J. Martin, N. Akerman, G. Ulbricht, T. Lohmann, J. H. Smet, K. von Klitzing & A. Yacoby. Observation of electron–hole puddles in graphene using a scanning single-electron transistor. *Nat. Phys.* **4**, 144–148 (2008).
- [82] S. V. Morozov, K. S. Novoselov, M. I. Katsnelson, F. Schedin, L. A. Ponomarenko, D. Jiang & A. K. Geim. Strong suppression of weak localization in graphene. *Phys. Rev. Lett.* **97**, 016801 (2006).
- [83] X. Du, I. Skachko, A. Barker & E. Y. Andrei. Approaching ballistic transport in suspended graphene. *Nat. Nanotechnol.* **3**, 491–495 (2008).
- [84] K. I. Bolotin, K. J. Sikes, J. Hone, H. L. Stormer & P. Kim. Temperature-dependent transport in suspended graphene. *Phys. Rev. Lett.* **101**, 096802 (2008).
- [85] E. V. Castro, H. Ochoa, M. I. Katsnelson, R. V. Gorbachev, D. C. Elias, K. S. Novoselov, A. K. Geim & F. Guinea. Limits on charge carrier mobility in suspended graphene due to flexural phonons. *Phys. Rev. Lett.* **105**, 266601 (2010).
- [86] C. R. Dean, a. F. Young, I. Meric, C. Lee, L. Wang, S. Sorgenfrei, K. Watanabe, T. Taniguchi, P. Kim, K. L. Shepard & J. Hone. Boron nitride substrates for high-quality graphene electronics. *Nat. Nanotechnol.* **5**, 722–726 (2010).

- [87] J. Xue, J. Sanchez-Yamagishi, D. Bulmash, P. Jacquod, A. Deshpande, K. Watanabe, T. Taniguchi, P. Jarillo-Herrero & B. J. LeRoy. Scanning tunnelling microscopy and spectroscopy of ultra-flat graphene on hexagonal boron nitride. *Nat. Mater.* **10**, 282–285 (2011).
- [88] E. H. Hwang, S. Adam & S. Das Sarma. Transport in chemically doped graphene in the presence of adsorbed molecules. *Phys. Rev. B* **76**, 195421 (2007).
- [89] L. Banszerus, M. Schmitz, S. Engels, M. Goldsche, K. Watanabe, T. Taniguchi, B. Beschoten & C. Stampfer. Ballistic transport exceeding 28  $\mu\text{m}$  in CVD grown graphene. *Nano Lett.* **16**, 1387–1391 (2016).
- [90] S. Y. Zhou, G.-H. Gweon, A. V. Fedorov, P. N. First, W. A. de Heer, D.-H. Lee, F. Guinea, A. H. Castro Neto & A. Lanzara. Substrate-induced bandgap opening in epitaxial graphene. *Nat. Mater.* **6**, 770–775 (2007).
- [91] E. Wang, X. Lu, S. Ding, W. Yao, M. Yan, G. Wan, K. Deng, S. Wang, G. Chen, L. Ma, J. Jung, A. V. Fedorov, Y. Zhang, G. Zhang & S. Zhou. Gaps induced by inversion symmetry breaking and second-generation Dirac cones in graphene/hexagonal boron nitride. *Nat. Phys.* **12**, 1111–1115 (2016).
- [92] J. C. W. Song, P. Samutpraphoot & L. S. Levitov. Topological Bloch bands in graphene superlattices. *Proc. Natl. Acad. Sci.* **112**, 10879–10883 (2015).
- [93] J. Jung, A. M. DaSilva, A. H. MacDonald & S. Adam. Origin of band gaps in graphene on hexagonal boron nitride. *Nat. Commun.* **6**, 6308 (2015).
- [94] C. R. Woods, L. Britnell, A. Eckmann, R. S. Ma, J. C. Lu, H. M. Guo, X. Lin, G. L. Yu, Y. Cao, R. V. Gorbachev, A. V. Kretinin, J. Park, L. A. Ponomarenko, M. I. Katsnelson, Y. N. Gornostyrev, K. Watanabe, T. Taniguchi, C. Casiraghi, H.-J. Gao, A. K. Geim & K. S. Novoselov. Commensurate–incommensurate transition in graphene on hexagonal boron nitride. *Nat. Phys.* **10**, 451–456 (2014).
- [95] K. Komatsu, Y. Morita, E. Watanabe, D. Tsuya, K. Watanabe, T. Taniguchi & S. Moriyama. Observation of the quantum valley Hall state in ballistic graphene superlattices. *Sci. Adv.* **4** (2018).
- [96] G. M. Rutter, S. Jung, N. N. Klimov, D. B. Newell, N. B. Zhitenev & J. A. Stroscio. Microscopic polarization in bilayer graphene. *Nat. Phys.* **7**, 649–655 (2011).
- [97] A. Hallal, F. Ibrahim, H. Yang, S. Roche & M. Chshiev. Tailoring magnetic insulator proximity effects in graphene: First-principles calculations. *2D Mater.* **4**, 025074 (2017).
- [98] O. V. Yazyev. Emergence of magnetism in graphene materials and nanostructures. *Reports Prog. Phys.* **73**, 056501 (2010).
- [99] P. O. Lehtinen, A. S. Foster, A. Ayuela, A. Krasheninnikov, K. Nordlund & R. M. Nieminen. Magnetic properties and diffusion of adatoms on a graphene sheet. *Phys. Rev. Lett.* **91**, 017202 (2003).

- [100] J. Dai & J. Yuan. Adsorption of molecular oxygen on doped graphene: Atomic, electronic, and magnetic properties. *Phys. Rev. B* **81**, 165414 (2010).
- [101] F. Schedin, A. K. Geim, S. V. Morozov, E. W. Hill, P. Blake, M. I. Katsnelson & K. S. Novoselov. Detection of individual gas molecules adsorbed on graphene. *Nat. Mater.* **6**, 652–655 (2007).
- [102] H. Haugen, D. Huertas-Hernando & A. Brataas. Spin transport in proximity-induced ferromagnetic graphene. *Phys. Rev. B* **77**, 115406 (2008).
- [103] A. G. Swartz, P. M. Odenthal, Y. Hao, R. S. Ruoff & R. K. Kawakami. Integration of the ferromagnetic insulator EuO onto graphene. *ACS Nano* **6**, 10063–10069 (2012).
- [104] P. Wei, S. Lee, F. Lemaitre, L. Pinel, D. Cutaia, W. Cha, F. Katmis, Y. Zhu, D. Heiman, J. Hone, J. S. Moodera & C.-T. Chen. Strong interfacial exchange field in the graphene/EuS heterostructure. *Nat. Mater.* **15**, 711–716 (2016).
- [105] Z. Liu, L. Song, S. Zhao, J. Huang, L. Ma, J. Zhang, J. Lou & P. M. Ajayan. Direct growth of graphene/hexagonal boron nitride stacked layers. *Nano Lett.* **11**, 2032–2037 (2011).
- [106] Y. Shi, W. Zhou, A.-Y. Lu, W. Fang, Y.-H. Lee, A. L. Hsu, S. M. Kim, K. K. Kim, H. Y. Yang, L.-J. Li, J.-C. Idrobo & J. Kong. van der Waals epitaxy of MoS<sub>2</sub> layers using graphene as growth templates. *Nano Lett.* **12**, 2784–2791 (2012).
- [107] K. Ariga, Q. Ji, J. P. Hill, Y. Bando & M. Aono. Forming nanomaterials as layered functional structures toward materials nanoarchitectonics. *NPG Asia Mater.* **4**, e17 (2012).
- [108] A. K. Geim & K. S. Novoselov. The rise of graphene. *Nat. Mater.* **6**, 183–191 (2007).
- [109] E. H. Hall. On a new action of the magnet on electric currents. *Am. J. Math.* **2**, 287 (1879).
- [110] K. V. Klitzing, G. Dorda & M. Pepper. New method for high-accuracy determination of the fine-structure constant based on quantized Hall resistance. *Phys. Rev. Lett.* **45**, 494–497 (1980).
- [111] S. Das Sarma & A. Pinczuk. *Perspectives in quantum Hall effects: Novel quantum liquids in low-dimensional semiconductor structures* (Wiley, 2008).
- [112] S. G. Sharapov, V. P. Gusynin & H. Beck. Magnetic oscillations in planar systems with the Dirac-like spectrum of quasiparticle excitations. *Phys. Rev. B* **69**, 075104 (2004).
- [113] K. S. Novoselov, Z. Jiang, Y. Zhang, S. V. Morozov, H. L. Stormer, U. Zeitler, J. C. Maan, G. S. Boebinger, P. Kim & A. K. Geim. Room-temperature quantum Hall effect in graphene. *Science* **315**, 1379–1379 (2007).
- [114] Y. Zhang, Y. Tan, H. L. Stormer & P. Kim. Experimental observation of the quantum Hall effect and Berry's phase in graphene. *Nature* **438**, 201–204 (2005).

- [115] Y. Zhang, Z. Jiang, J. P. Small, M. S. Purewal, Y.-W. Tan, M. Fazlollahi, J. D. Chudow, J. A. Jaszczak, H. L. Stormer & P. Kim. Landau-level splitting in graphene in high magnetic fields. *Phys. Rev. Lett.* **96**, 136806 (2006).
- [116] D. A. Abanin, K. S. Novoselov, U. Zeitler, P. A. Lee, A. K. Geim & L. S. Levitov. Dissipative quantum Hall effect in graphene near the Dirac point. *Phys. Rev. Lett.* **98**, 196806 (2007).
- [117] A. J. M. Giesbers, U. Zeitler, M. I. Katsnelson, L. A. Ponomarenko, T. M. Mohiuddin & J. C. Maan. Quantum-Hall activation gaps in graphene. *Phys. Rev. Lett.* **99**, 206803 (2007).
- [118] Z. Jiang, Y. Zhang, H. L. Stormer & P. Kim. Quantum Hall states near the charge-neutral Dirac point in graphene. *Phys. Rev. Lett.* **99**, 106802 (2007).
- [119] D. A. Abanin, P. A. Lee & L. S. Levitov. Charge and spin transport at the quantum Hall edge of graphene. *Solid State Commun.* **143**, 77–85 (2007).
- [120] J.-N. Fuchs & P. Lederer. Spontaneous parity breaking of graphene in the quantum Hall regime. *Phys. Rev. Lett.* **98**, 016803 (2007).
- [121] M. Dyakonov & V. Perel. Current-induced spin orientation of electrons in semiconductors. *Phys. Lett. A* **35**, 459–460 (1971).
- [122] C. L. Kane & E. J. Mele. Quantum spin Hall effect in graphene. *Phys. Rev. Lett.* **95**, 226801 (2005).
- [123] C. Weeks, J. Hu, J. Alicea, M. Franz & R. Wu. Engineering a robust quantum spin Hall State in graphene via adatom deposition. *Phys. Rev. X* **1**, 021001 (2011).
- [124] H. Min, J. E. Hill, N. A. Sinitsyn, B. R. Sahu, L. Kleinman & A. H. MacDonald. Intrinsic and Rashba spin-orbit interactions in graphene sheets. *Phys. Rev. B* **74**, 165310 (2006).
- [125] Y. Yao, F. Ye, X.-L. Qi, S.-C. Zhang & Z. Fang. Spin-orbit gap of graphene: First-principles calculations. *Phys. Rev. B* **75**, 041401 (2007).
- [126] M. Gmitra & J. Fabian. Graphene on transition-metal dichalcogenides: A platform for proximity spin-orbit physics and optospintronics. *Phys. Rev. B* **92**, 155403 (2015).
- [127] Z. Wang, D.-K. Ki, H. Chen, H. Berger, A. H. MacDonald & A. F. Morpurgo. Strong interface-induced spin-orbit interaction in graphene on WS<sub>2</sub>. *Nat. Commun.* **6**, 8339 (2015).
- [128] B. A. Bernevig, T. L. Hughes & S.-C. Zhang. Quantum spin Hall effect and topological phase transition in HgTe quantum wells. *Science* **314**, 1757–1761 (2006).
- [129] M. König, S. Wiedmann, C. Brune, A. Roth, H. Buhmann, L. W. Molenkamp, X.-L. Qi & S.-C. Zhang. Quantum spin Hall insulator state in HgTe quantum wells. *Science* **318**, 766–770 (2007).
- [130] L. Fu, C. L. Kane & E. J. Mele. Topological insulators in three dimensions. *Phys. Rev. Lett.* **98**, 106803 (2007).

- [131] D. Hsieh, D. Qian, L. Wray, Y. Xia, Y. S. Hor, R. J. Cava & M. Z. Hasan. A topological Dirac insulator in a quantum spin Hall phase. *Nature* **452**, 970–974 (2008).
- [132] H. Zhang, C.-X. Liu, X.-L. Qi, X. Dai, Z. Fang & S.-C. Zhang. Topological insulators in  $\text{Bi}_2\text{Se}_3$ ,  $\text{Bi}_2\text{Te}_3$  and  $\text{Sb}_2\text{Te}_3$  with a single Dirac cone on the surface. *Nat. Phys.* **5**, 438–442 (2009).
- [133] Y. Xia, D. Qian, D. Hsieh, L. Wray, A. Pal, H. Lin, A. Bansil, D. Grauer, Y. S. Hor, R. J. Cava & M. Z. Hasan. Observation of a large-gap topological-insulator class with a single Dirac cone on the surface. *Nat. Phys.* **5**, 398–402 (2009).
- [134] D. Hsieh, Y. Xia, L. Wray, D. Qian, A. Pal, J. H. Dil, J. Osterwalder, F. Meier, G. Bihlmayer, C. L. Kane, Y. S. Hor, R. J. Cava & M. Z. Hasan. Observation of unconventional quantum spin textures in topological insulators. *Science* **323**, 919–922 (2009).
- [135] Y. L. Chen, J. G. Analytis, J.-H. Chu, Z. K. Liu, S.-K. Mo, X. L. Qi, H. J. Zhang, D. H. Lu, X. Dai, Z. Fang, S. C. Zhang, I. R. Fisher, Z. Hussain & Z.-X. Shen. Experimental realization of a three-dimensional topological insulator,  $\text{Bi}_2\text{Te}_3$ . *Science* **325**, 178–181 (2009).
- [136] A. P. Protogenov, V. A. Verbus & E. V. Chulkov. Nonlocal edge state transport in topological insulators. *Phys. Rev. B* **88**, 195431 (2013).
- [137] K. Nomura & A. H. MacDonald. Quantum Hall ferromagnetism in graphene. *Phys. Rev. Lett.* **96**, 256602 (2006).
- [138] J. Alicea & M. P. A. Fisher. Graphene integer quantum Hall effect in the ferromagnetic and paramagnetic regimes. *Phys. Rev. B* **74**, 075422 (2006).
- [139] K. Yang, S. Das Sarma & A. H. MacDonald. Collective modes and skyrmion excitations in graphene  $\text{SU}(4)$  quantum Hall ferromagnets. *Phys. Rev. B* **74**, 075423 (2006).
- [140] M. O. Goerbig, R. Moessner & B. Douçot. Electron interactions in graphene in a strong magnetic field. *Phys. Rev. B* **74**, 161407 (2006).
- [141] J. G. Checkelsky, L. Li & N. P. Ong. Zero-energy state in graphene in a high magnetic field. *Phys. Rev. Lett.* **100**, 206801 (2008).
- [142] M. Kharitonov. Phase diagram for the  $\nu = 0$  quantum Hall state in monolayer graphene. *Phys. Rev. B* **85**, 155439 (2012).
- [143] K. Nomura, S. Ryu & D.-H. Lee. Field-induced Kosterlitz-Thouless transition in the  $N = 0$  Landau level of graphene. *Phys. Rev. Lett.* **103**, 216801 (2009).
- [144] D. A. Abanin, P. A. Lee & L. S. Levitov. Spin-filtered edge states and quantum Hall effect in graphene. *Phys. Rev. Lett.* **96**, 176803 (2006).
- [145] H. A. Fertig & L. Brey. Luttinger liquid at the edge of undoped graphene in a strong magnetic field. *Phys. Rev. Lett.* **97**, 116805 (2006).

- [146] C.-Z. Chang, W. Zhao, D. Y. Kim, H. Zhang, B. A. Assaf, D. Heiman, S.-C. Zhang, C. Liu, M. H. W. Chan & J. S. Moodera. High-precision realization of robust quantum anomalous Hall state in a hard ferromagnetic topological insulator. *Nat. Mater.* **14**, 473–477 (2015).
- [147] F. D. M. Haldane. Model for a quantum Hall effect without Landau levels: Condensed-matter realization of the "parity anomaly". *Phys. Rev. Lett.* **61**, 2015–2018 (1988).
- [148] C.-Z. Chang, J. Zhang, X. Feng, J. Shen, Z. Zhang, M. Guo, K. Li, Y. Ou, P. Wei, L.-L. Wang, Z.-Q. Ji, Y. Feng, S. Ji, X. Chen, J. Jia, X. Dai, Z. Fang, S.-C. Zhang, K. He, Y. Wang, L. Lu, X.-C. Ma & Q.-K. Xue. Experimental observation of the quantum anomalous Hall effect in a magnetic topological insulator. *Science* **340**, 167–170 (2013).
- [149] H. X. Yang, A. Hallal, D. Terrade, X. Waintal, S. Roche & M. Chshiev. Proximity effects induced in graphene by magnetic insulators: First-principles calculations on spin filtering and exchange-splitting gaps. *Phys. Rev. Lett.* **110**, 046603 (2013).
- [150] C. W. J. Beenakker. Colloquium : Andreev reflection and Klein tunneling in graphene. *Rev. Mod. Phys.* **80**, 1337–1354 (2008).
- [151] M. Cardona. *Light scattering in solids I*, vol. 8 of *Topics in applied physics* (Springer-Verlag Berlin Heidelberg, 1983).
- [152] P. Eaton & P. West. *Atomic force microscopy* (Oxford University Press, 2010).
- [153] B. Voigtländer. *Scanning probe microscopy: Atomic force microscopy and scanning tunneling microscopy* (Springer, 2015).
- [154] X.-Y. Wang, A. Narita & K. Müllen. Precision synthesis versus bulk-scale fabrication of graphenes. *Nat. Rev. Chem.* **2**, 0100 (2018).
- [155] M. Bruna & S. Borini. Optical constants of graphene layers in the visible range. *Appl. Phys. Lett.* **94**, 031901 (2009).
- [156] K. S. Novoselov & A. H. Castro Neto. Two-dimensional crystals-based heterostructures: materials with tailored properties. *Phys. Scr.* **T146**, 014006 (2012).
- [157] F. Bonaccorso, A. Lombardo, T. Hasan, Z. Sun, L. Colombo & A. C. Ferrari. Production and processing of graphene and 2d crystals. *Mater. Today* **15**, 564–589 (2012).
- [158] F. Pizzocchero, L. Gammelgaard, B. S. Jessen, J. M. Caridad, L. Wang, J. Hone, P. Bøggild & T. J. Booth. The hot pick-up technique for batch assembly of van der Waals heterostructures. *Nat. Commun.* **7**, 11894 (2016).
- [159] C. F. Fan, T. Çagin, W. Shi & K. A. Smith. Local chain dynamics of a model polycarbonate near glass transition temperature: A molecular dynamics simulation. *Macromol. Theory Simulations* **6**, 83–102 (1997).

- [160] S. J. Haigh, A. Gholinia, R. Jalil, S. Romani, L. Britnell, D. C. Elias, K. S. Novoselov, L. A. Ponomarenko, A. K. Geim & R. Gorbachev. Cross-sectional imaging of individual layers and buried interfaces of graphene-based heterostructures and superlattices. *Nat. Mater.* **11**, 764–767 (2012).
- [161] M. Shone. The technology of YIG film growth. *Circuits, Syst. Signal Process.* **4**, 89–103 (1985).
- [162] R. Karim, S. Oliver & C. Vittoria. Laser ablation deposition of YIG films on semiconductor and amorphous substrates. *IEEE Trans. Magn.* **31**, 3485–3487 (1995).
- [163] W. J. Pyung & Y. K. Ji. New growth method of solid phase epitaxy in sputtered YIG films. *IEEE Trans. Magn.* **37**, 2438–2440 (2001).
- [164] Y. Sun, Y.-Y. Song, H. Chang, M. Kabatek, M. Jantz, W. Schneider, M. Wu, H. Schultheiss & A. Hoffmann. Growth and ferromagnetic resonance properties of nanometer-thick yttrium iron garnet films. *Appl. Phys. Lett.* **101**, 152405 (2012).
- [165] R. C. LeCraw, E. G. Spencer & C. S. Porter. Ferromagnetic resonance line width in yttrium iron garnet single crystals. *Phys. Rev.* **110**, 1311–1313 (1958).
- [166] R. C. Linares, R. B. McGraw & J. B. Schroeder. Growth and properties of yttrium iron garnet single-crystal films. *J. Appl. Phys.* **36**, 2884–2886 (1965).
- [167] Y. Krockenberger, K.-S. Yun, T. Hatano, S. Arisawa, M. Kawasaki & Y. Tokura. Layer-by-layer growth and magnetic properties of  $\text{Y}_3\text{Fe}_5\text{O}_{12}$  thin films on  $\text{Gd}_3\text{Ga}_5\text{O}_{12}$ . *J. Appl. Phys.* **106**, 123911 (2009).
- [168] F. J. Bruni. *Gadolinium gallium garnet*, 53–70 (Springer Berlin Heidelberg, 1978).
- [169] D. F. O’Kane, V. Sadagopan, E. A. Giess & E. Mendel. Crystal growth and characterization of gadolinium gallium garnet. *J. Electrochem. Soc.* **120**, 1272 (1973).
- [170] M. Pardavi-Horváth, I. Földvári, I. Fellegvári, L. Gosztonyi & J. Paitz. Spectroscopic properties of  $\text{Ca}^{2+}$ -doped GGG. *Phys. Status Solidi* **84**, 547–553 (1984).
- [171] E. Hartmann, L. Kovács & J. Paitz. Electrical conductivity of gadolinium–gallium garnet (GGG) crystals. *Phys. Status Solidi* **86**, 401–405 (1984).
- [172] X. Liu. *Experimental studies of oxide magnetic tunnel junctions and graphene*. Ph.D. thesis, University of California Riverside (2014).
- [173] W. H. Bragg & W. L. Bragg. The reflection of X-rays by crystals. *Proceedings of the Royal Society of London. Series A, Containing Papers of a Mathematical and Physical Character* **88**, 428–438 (1913).
- [174] U. König, R. S. Angélica, N. Norberg & L. Gobbo. Rapid X-ray diffraction (XRD) for grade control of bauxites. *ICSOBA Proceedings* **19** (2012).
- [175] M. R. Sardela. *X-ray diffraction and reflectivity*, 1–41 (Springer, 2014).
- [176] B. D. Cullity & S. R. Stock. *Elements of X-ray diffraction* (Pearson, New Jersey, 2001).

- [177] J. Daillant & A. Gibaud. *X-ray and neutron reflectivity: Principles and applications* (Springer, 2008).
- [178] P. L. McEuen, A. Szafer, C. A. Richter, B. W. Alphenaar, J. K. Jain, A. D. Stone, R. G. Wheeler & R. N. Sacks. New resistivity for high-mobility quantum Hall conductors. *Phys. Rev. Lett.* **64**, 2062–2065 (1990).
- [179] R. J. Haug. Edge-state transport and its experimental consequences in high magnetic fields. *Semicond. Sci. Technol.* **8**, 131–153 (1993).
- [180] Y. Tserkovnyak, A. Brataas, G. E. W. Bauer & B. I. Halperin. Nonlocal magnetization dynamics in ferromagnetic heterostructures. *Rev. Mod. Phys.* **77**, 1375–1421 (2005).
- [181] F. J. Jedema, M. S. Nijboer, A. T. Filip & B. J. van Wees. Spin injection and spin accumulation in all-metal mesoscopic spin valves. *Phys. Rev. B* **67**, 085319 (2003).
- [182] D. A. Abanin, S. V. Morozov, L. A. Ponomarenko, R. V. Gorbachev, A. S. Mayorov, M. I. Katsnelson, K. Watanabe, T. Taniguchi, K. S. Novoselov, L. S. Levitov & A. K. Geim. Giant nonlocality near the Dirac point in graphene. *Science* **332**, 328–330 (2011).
- [183] J. Renard, M. Studer & J. A. Folk. Origins of nonlocality near the neutrality point in graphene. *Phys. Rev. Lett.* **112**, 116601 (2014).
- [184] Y. M. Zuev, W. Chang & P. Kim. Thermoelectric and magnetothermoelectric transport measurements of graphene. *Phys. Rev. Lett.* **102**, 096807 (2009).
- [185] F. L. Bakker, A. Slachter, J.-P. Adam & B. J. van Wees. Interplay of Peltier and Seebeck effects in nanoscale nonlocal spin valves. *Phys. Rev. Lett.* **105**, 136601 (2010).
- [186] M. Johnson & R. H. Silsbee. Interfacial charge-spin coupling: Injection and detection of spin magnetization in metals. *Phys. Rev. Lett.* **55**, 1790–1793 (1985).
- [187] D. A. Abanin, R. V. Gorbachev, K. S. Novoselov, A. K. Geim & L. S. Levitov. Giant spin-Hall effect induced by the Zeeman interaction in graphene. *Phys. Rev. Lett.* **107**, 096601 (2011).
- [188] R. V. Gorbachev, J. C. W. Song, G. L. Yu, A. V. Kretinin, F. Withers, Y. Cao, A. Mishchenko, I. V. Grigorieva, K. S. Novoselov, L. S. Levitov & A. K. Geim. Detecting topological currents in graphene superlattices. *Science* **346**, 448–451 (2014).
- [189] Y. Sun & M. Wu. *Yttrium iron garnet nano films: Epitaxial growth, spin-pumping efficiency, and Pt-capping-caused damping*, vol. 64 of *Solid State Physics*, 157 – 191 (Academic Press, 2013).
- [190] H. Zhang, C. Lazo, S. Blügel, S. Heinze & Y. Mokrousov. Electrically tunable quantum anomalous Hall effect in graphene decorated by 5d transition-metal adatoms. *Phys. Rev. Lett.* **108**, 056802 (2012).
- [191] S. Konschuh, M. Gmitra & J. Fabian. Tight-binding theory of the spin-orbit coupling in graphene. *Phys. Rev. B* **82**, 245412 (2010).

- [192] A. Avsar, J. Y. Tan, T. Taychatanapat, J. Balakrishnan, G. Koon, Y. Yeo, J. Lahiri, A. Carvalho, A. S. Rodin, E. O'Farrell, G. Eda, A. H. Castro Neto & B. Özyilmaz. Spin-orbit proximity effect in graphene. *Nat. Commun.* **5**, 4875 (2014).
- [193] Y. S. Dedkov, M. Fonin, U. Rüdiger & C. Laubschat. Rashba effect in the graphene/Ni(111) system. *Phys. Rev. Lett.* **100**, 107602 (2008).
- [194] D. A. Abanin, A. V. Shytov, L. S. Levitov & B. I. Halperin. Nonlocal charge transport mediated by spin diffusion in the spin Hall effect regime. *Phys. Rev. B* **79**, 035304 (2009).
- [195] F. D. M. Haldane. Berry curvature on the Fermi surface: Anomalous Hall effect as a topological Fermi-liquid property. *Phys. Rev. Lett.* **93**, 206602 (2004).
- [196] M. Sui, G. Chen, L. Ma, W. Y. Shan, D. Tian, K. Watanabe, T. Taniguchi, X. Jin, W. Yao, D. Xiao & Y. Zhang. Gate-tunable topological valley transport in bilayer graphene. *Nat. Phys.* **11**, 1027–1031 (2015).
- [197] Y. Shimazaki, M. Yamamoto, I. V. Borzenets, K. Watanabe, T. Taniguchi & S. Tarucha. Generation and detection of pure valley current by electrically induced Berry curvature in bilayer graphene. *Nat. Phys.* **11**, 1032–1036 (2015).
- [198] M. Yamamoto, Y. Shimazaki, I. V. Borzenets & S. Tarucha. Valley Hall effect in two-dimensional hexagonal lattices. *J. Phys. Soc. Japan* **84**, 121006 (2015).
- [199] L. Brey & H. A. Fertig. Edge states and the quantized Hall effect in graphene. *Phys. Rev. B* **73**, 195408 (2006).
- [200] K. Nakada, M. Fujita, G. Dresselhaus & M. S. Dresselhaus. Edge state in graphene ribbons: Nanometer size effect and edge shape dependence. *Phys. Rev. B* **54**, 17954–17961 (1996).
- [201] P. A. Maksimov, A. V. Rozhkov & A. O. Sboychakov. Localized electron states near the armchair edge of graphene. *Phys. Rev. B* **88**, 245421 (2013).
- [202] N. M. R. Peres, F. Guinea & A. H. Castro Neto. Electronic properties of disordered two-dimensional carbon. *Phys. Rev. B* **73**, 125411 (2006).
- [203] W. Yao, S. A. Yang & Q. Niu. Edge states in graphene: From gapped flat-band to gapless chiral modes. *Phys. Rev. Lett.* **102**, 096801 (2009).
- [204] M. Büttiker. Absence of backscattering in the quantum Hall effect in multiprobe conductors. *Phys. Rev. B* **38**, 9375–9389 (1988).
- [205] A. Roth, C. Brune, H. Buhmann, L. W. Molenkamp, J. Maciejko, X.-L. Qi & S.-C. Zhang. Nonlocal transport in the quantum spin Hall state. *Science* **325**, 294–297 (2009).
- [206] J. G. Checkelsky & N. P. Ong. Thermopower and Nernst effect in graphene in a magnetic field. *Phys. Rev. B* **80**, 081413 (2009).
- [207] X. Liu, D. Wang, P. Wei, L. Zhu & J. Shi. Effect of carrier mobility on magnetothermoelectric transport properties of graphene. *Phys. Rev. B* **86**, 155414 (2012).

- [208] R. T. Delves. Thermomagnetic effects in semiconductors and semimetals. *Reports Prog. Phys.* **28**, 308 (1965).
- [209] C. H. Park, L. Yang, Y. W. Son, M. L. Cohen & S. G. Louie. Anisotropic behaviours of massless Dirac fermions in graphene under periodic potentials. *Nat. Phys.* **4**, 213–217 (2008).
- [210] C. H. Park, L. Yang, Y. W. Son, M. L. Cohen & S. G. Louie. New generation of massless Dirac fermions in graphene under external periodic potentials. *Phys. Rev. Lett.* **101**, 126804 (2008).
- [211] G. L. Yu, R. V. Gorbachev, J. S. Tu, A. V. Kretinin, Y. Cao, R. Jalil, F. Withers, L. A. Ponomarenko, B. A. Piot, M. Potemski, D. C. Elias, X. Chen, K. Watanabe, T. Taniguchi, I. V. Grigorieva, K. S. Novoselov, V. I. Fal'ko, A. K. Geim & A. Mishchenko. Hierarchy of Hofstadter states and replica quantum Hall ferromagnetism in graphene superlattices. *Nat. Phys.* **10**, 525–529 (2014).
- [212] J. M. Marmolejo-Tejada, J. H. García, M. D. Petrović, P.-H. Chang, X.-L. Sheng, A. Cresti, P. Plecháč, S. Roche & B. K. Nikolić. Deciphering the origin of nonlocal resistance in multiterminal graphene on hexagonal-boron-nitride with ab initio quantum transport: Fermi surface edge currents rather than Fermi sea topological valley currents. *J. Phys. Mater.* **1**, 015006 (2018).
- [213] J. E. Lee, G. Ahn, J. Shim, Y. S. Lee & S. Ryu. Optical separation of mechanical strain from charge doping in graphene. *Nat. Commun.* **3**, 1024 (2012).
- [214] A. Eckmann, J. Park, H. Yang, D. Elias, A. S. Mayorov, G. Yu, R. Jalil, K. S. Novoselov, R. V. Gorbachev, M. Lazzeri, A. K. Geim & C. Casiraghi. Raman fingerprint of aligned graphene/h-BN superlattices. *Nano Lett.* **13**, 5242–5246 (2013).
- [215] K. Bolotin, K. Sikes, Z. Jiang, M. Klima, G. Fudenberg, J. Hone, P. Kim & H. Stormer. Ultrahigh electron mobility in suspended graphene. *Solid State Commun.* **146**, 351–355 (2008).
- [216] J. C. Song, A. V. Shytov & L. S. Levitov. Electron interactions and gap opening in graphene superlattices. *Phys. Rev. Lett.* **111**, 266801 (2013).
- [217] N. F. Mott. Conduction in non-crystalline materials. *Philos. Mag.* **19**, 835–852 (1969).
- [218] S. N. Mott. Metal–insulator transitions. *Phys. Today* **31**, 42–47 (1978).
- [219] A. L. Efros & B. I. Shklovskii. Coulomb gap and low temperature conductivity of disordered systems. *J. Phys. C Solid State Phys.* **8**, L49–L51 (1975).
- [220] Y.-F. Lu, S.-T. Lo, J.-C. Lin, W. Zhang, J.-Y. Lu, F.-H. Liu, C.-M. Tseng, Y.-H. Lee, C.-T. Liang & L.-J. Li. Nitrogen-doped graphene sheets grown by chemical vapor deposition: Synthesis and influence of nitrogen impurities on carrier transport. *ACS Nano* **7**, 6522–6532 (2013).
- [221] M. Büttiker. Four-terminal phase-coherent conductance. *Phys. Rev. Lett.* **57**, 1761–1764 (1986).

- [222] H. U. Baranger & A. D. Stone. Electrical linear-response theory in an arbitrary magnetic field: A new Fermi-surface formation. *Phys. Rev. B* **40**, 8169–8193 (1989).
- [223] J. Li, I. Martin, M. Büttiker & A. F. Morpurgo. Topological origin of subgap conductance in insulating bilayer graphene. *Nat. Phys.* **7**, 38–42 (2011).
- [224] J. S. Alden, A. W. Tsen, P. Y. Huang, R. Hovden, L. Brown, J. Park, D. A. Muller & P. L. McEuen. Strain solitons and topological defects in bilayer graphene. *Proc. Natl. Acad. Sci.* **110**, 11256–11260 (2013).
- [225] P. San-Jose & E. Prada. Helical networks in twisted bilayer graphene under interlayer bias. *Phys. Rev. B* **88**, 121408 (2013).
- [226] L. Ju, Z. Shi, N. Nair, Y. Lv, C. Jin, J. Velasco, C. Ojeda-Aristizabal, H. A. Bechtel, M. C. Martin, A. Zettl, J. Analytis & F. Wang. Topological valley transport at bilayer graphene domain walls. *Nature* **520**, 650–655 (2015).
- [227] S. Huang, K. Kim, D. K. Efimkin, T. Lovorn, T. Taniguchi, K. Watanabe, A. H. MacDonald, E. Tutuc & B. J. LeRoy. Topologically protected helical states in minimally twisted bilayer graphene. *Phys. Rev. Lett.* **121**, 037702 (2018).
- [228] P. Rickhaus, J. Wallbank, S. Slizovskiy, R. Pisoni, H. Overweg, Y. Lee, M. Eich, M.-H. Liu, K. Watanabe, T. Taniguchi, T. Ihn & K. Ensslin. Transport through a network of topological channels in twisted bilayer graphene. *Nano Lett.* **18**, 6725–6730 (2018).
- [229] H. Yoo, R. Engelke, S. Carr, S. Fang, K. Zhang, P. Cazeaux, S. H. Sung, R. Hovden, A. W. Tsen, T. Taniguchi, K. Watanabe, G.-C. Yi, M. Kim, M. Luskin, E. B. Tadmor, E. Kaxiras & P. Kim. Atomic and electronic reconstruction at the van der Waals interface in twisted bilayer graphene. *Nat. Mater.* **18**, 448–453 (2019).
- [230] X. Xu, W. Yao, D. Xiao & T. F. Heinz. Spin and pseudospins in layered transition metal dichalcogenides. *Nat. Phys.* **10**, 343–350 (2014).
- [231] K. F. Mak, K. He, J. Shan & T. F. Heinz. Control of valley polarization in monolayer MoS<sub>2</sub> by optical helicity. *Nat. Nanotechnol.* **7**, 494–498 (2012).
- [232] H. Zeng, J. Dai, W. Yao, D. Xiao & X. Cui. Valley polarization in MoS<sub>2</sub> monolayers by optical pumping. *Nat. Nanotechnol.* **7**, 490–493 (2012).
- [233] J. Lee, K. F. Mak & J. Shan. Electrical control of the valley Hall effect in bilayer MoS<sub>2</sub> transistors. *Nat. Nanotechnol.* **11**, 421–425 (2016).
- [234] M. A. H. Vozmediano, M. P. López-Sancho, T. Stauber & F. Guinea. Local defects and ferromagnetism in graphene layers. *Phys. Rev. B* **72**, 155121 (2005).
- [235] D. Kochan, M. Gmitra & J. Fabian. Spin relaxation mechanism in graphene: Resonant scattering by magnetic impurities. *Phys. Rev. Lett.* **112**, 116602 (2014).
- [236] R. R. Nair, M. Sepioni, I.-L. Tsai, O. Lehtinen, J. Keinonen, A. V. Krasheninnikov, T. Thomson, A. K. Geim & I. V. Grigorieva. Spin-half paramagnetism in graphene induced by point defects. *Nat. Phys.* **8**, 199–202 (2012).

- [237] L. Xie, X. Wang, J. Lu, Z. Ni, Z. Luo, H. Mao, R. Wang, Y. Wang, H. Huang, D. Qi, R. Liu, T. Yu, Z. Shen, T. Wu, H. Peng, B. Özyilmaz, K. Loh, A. T. S. Wee, Ariando & W. Chen. Room temperature ferromagnetism in partially hydrogenated epitaxial graphene. *Appl. Phys. Lett.* **98**, 193113 (2011).
- [238] Z. Qiao, W. Ren, H. Chen, L. Bellaiche, Z. Zhang, A. H. MacDonald & Q. Niu. Quantum anomalous Hall effect in graphene proximity coupled to an antiferromagnetic insulator. *Phys. Rev. Lett.* **112**, 116404 (2014).
- [239] J. Lee & J. Fabian. Magnetotransport signatures of the proximity exchange and spin-orbit couplings in graphene. *Phys. Rev. B* **94**, 195401 (2016).
- [240] M. Kharitonov. Edge excitations of the canted antiferromagnetic phase of the  $\nu = 0$  quantum Hall state in graphene: A simplified analysis. *Phys. Rev. B* **86**, 075450 (2012).
- [241] B. Feshami & H. A. Fertig. Hartree-Fock study of the  $\nu = 0$  quantum Hall state of monolayer graphene with short-range interactions. *Phys. Rev. B* **94**, 245435 (2016).
- [242] D. S. Wei, T. van der Sar, S. H. Lee, K. Watanabe, T. Taniguchi, B. I. Halperin & A. Yacoby. Electrical generation and detection of spin waves in a quantum Hall ferromagnet. *Science* **362**, 229–233 (2018).
- [243] A. F. Young, C. R. Dean, L. Wang, H. Ren, P. Cadden-Zimansky, K. Watanabe, T. Taniguchi, J. Hone, K. L. Shepard & P. Kim. Spin and valley quantum Hall ferromagnetism in graphene. *Nat. Phys.* **8**, 550–556 (2012).
- [244] A. F. Young, J. D. Sanchez-Yamagishi, B. Hunt, S. H. Choi, K. Watanabe, T. Taniguchi, R. C. Ashoori & P. Jarillo-Herrero. Tunable symmetry breaking and helical edge transport in a graphene quantum spin Hall state. *Nature* **505**, 528–532 (2014).
- [245] P. Stepanov, S. Che, D. Shcherbakov, J. Yang, R. Chen, K. Thilagar, G. Voigt, M. W. Bockrath, D. Smirnov, K. Watanabe, T. Taniguchi, R. K. Lake, Y. Barlas, A. H. MacDonald & C. N. Lau. Long-distance spin transport through a graphene quantum Hall antiferromagnet. *Nat. Phys.* **14**, 907–911 (2018).
- [246] R. Metselaar & P. K. Larsen. High-temperature electrical properties of yttrium iron garnet under varying oxygen pressures. *Solid State Commun.* **15**, 291–294 (1974).
- [247] N. G. Kovalchuk, K. A. Nigirish, M. M. Mikhailik, N. I. Kargin, I. V. Komissarov & S. L. Prischepa. Possibility of determining the graphene doping level using Raman spectra. *J. Appl. Spectrosc.* **84**, 995–998 (2018).
- [248] L. Pietrobon, L. Fallarino, A. Berger, A. Chuvilin, F. Casanova & L. E. Hueso. Weak delocalization in graphene on a ferromagnetic insulating film. *Small* **11**, 6295–6301 (2015).
- [249] M. Evelt, H. Ochoa, O. Dzyapko, V. E. Demidov, A. Yurgens, J. Sun, Y. Tserkovnyak, V. Bessonov, A. B. Rinkevich & S. O. Demokritov. Chiral charge pumping in graphene deposited on a magnetic insulator. *Phys. Rev. B* **95**, 024408 (2017).

- [250] V. T. Phong, N. R. Walet & F. Guinea. Effective interactions in a graphene layer induced by the proximity to a ferromagnet. *2D Mater.* **5**, 014004 (2017).
- [251] G. Murthy, E. Shimshoni & H. A. Fertig. Collective edge modes near the onset of a graphene quantum spin Hall state. *Phys. Rev. B* **90**, 241410 (2014).
- [252] D. I. Pikulin, P. G. Silvestrov & T. Hyart. Confinement-deconfinement transition due to spontaneous symmetry breaking in quantum Hall bilayers. *Nat. Commun.* **7**, 10462 (2016).
- [253] J. Ingla-Aynés, M. H. D. Guimarães, R. J. Meijerink, P. J. Zomer & B. J. van Wees. 24- $\mu\text{m}$  spin relaxation length in boron nitride encapsulated bilayer graphene. *Phys. Rev. B* **92**, 201410 (2015).
- [254] N. Nagaosa, J. Sinova, S. Onoda, A. H. MacDonald & N. P. Ong. Anomalous Hall effect. *Rev. Mod. Phys.* **82**, 1539–1592 (2010).
- [255] Z. Y. Zhu, Y. C. Cheng & U. Schwingenschlögl. Giant spin-orbit-induced spin splitting in two-dimensional transition-metal dichalcogenide semiconductors. *Phys. Rev. B* **84**, 153402 (2011).
- [256] S. Zihlmann, A. W. Cummings, J. H. Garcia, M. Kedves, K. Watanabe, T. Taniguchi, C. Schönenberger & P. Makk. Large spin relaxation anisotropy and valley-Zeeman spin-orbit coupling in  $\text{WSe}_2/\text{graphene}/\text{h-BN}$  heterostructures. *Phys. Rev. B* **97**, 075434 (2018).
- [257] T. Völkl, T. Rockinger, M. Drienovsky, K. Watanabe, T. Taniguchi, D. Weiss & J. Eroms. Magnetotransport in heterostructures of transition metal dichalcogenides and graphene. *Phys. Rev. B* **96**, 125405 (2017).
- [258] X. Kou, Y. Fan, M. Lang, P. Upadhyaya & K. L. Wang. Magnetic topological insulators and quantum anomalous hall effect. *Solid State Commun.* **215-216**, 34–53 (2015).
- [259] R. E. Bornfreund, D. C. Khan, P. E. Wigen, M. Pardavi-Horvath, J. Ings & R. Belt. Spin reorientation in  $\text{Tm}_{2.14}\text{Bi}_{0.80}\text{Pb}_{0.06}\text{Fe}_{3.1}\text{Ga}_{1.9}\text{O}_{12}$  thin films. *IEEE Trans. Magn.* **28**, 2991–2993 (1992).
- [260] X. Du, I. Skachko, F. Duerr, A. Luican & E. Y. Andrei. Fractional quantum Hall effect and insulating phase of Dirac electrons in graphene. *Nature* **462**, 192–195 (2009).

# Appendix A

## Calculation of the transmission probability

According to the Landauer-Büttiker formalism, the current from terminal  $p$  towards the sample is given by

$$I_p = G_0 \sum_q Tr_{p,q}(V_p - V_q), \quad (\text{A.1})$$

where conductance  $G_0 = e^2/h$ ,  $Tr_{p,q} = Tr_{p \leftarrow q}$  is the transmission probability from terminal  $q$  to terminal  $p$ ,  $V$  is the voltage. Equation (A.1) can be expressed in the matrix form as

$$I = GV, \quad (\text{A.2})$$

where the conductance matrix is given by

$$G = G_0 \begin{bmatrix} \sum_q Tr_{1,q} & -Tr_{1,2} & -Tr_{1,3} & \cdots & -Tr_{1,10} \\ -Tr_{2,1} & \sum_q Tr_{2,q} & -Tr_{2,3} & \cdots & -Tr_{2,10} \\ -Tr_{3,1} & -Tr_{3,2} & \sum_q Tr_{3,q} & \cdots & -Tr_{3,10} \\ \vdots & \vdots & \vdots & \vdots & \vdots \\ -Tr_{10,1} & -Tr_{10,2} & -Tr_{10,3} & \cdots & \sum_q Tr_{10,q} \end{bmatrix}, \quad (\text{A.3})$$

and  $I$  is the matrix where column describes a given current configuration (currents inject from terminals to the sample) and  $V$  is a matrix where each column describes the corresponding voltage configuration (voltage of different terminals).

These equations can be solved in following ways:

1. If the voltage configuration ( $V$ ) and  $Tr_{p,q}$  are known, one can straightforwardly determine the corresponding current ( $I$ ) from Equations (A.2) and (A.3).

2. If the current configuration ( $I$ ) and  $Tr_{p,q}$  are known, one can determine the corresponding voltage ( $V$ ) at different terminals.
3. If one has measured ten independent current configurations ( $I$ ) with corresponding voltage configurations ( $V$ ), the conductance matrix ( $G$ ) can be determined from

$$G = IV^{-1}. \quad (\text{A.4})$$

After determining  $G$ , the transmission matrix can be obtained from Equation (A.3). One way of obtaining ten independent current configurations with corresponding voltage is to apply current between terminals  $p-1$  and  $p$ , then cyclically shift the source and drain terminals so that one gets a  $10 \times 10$  current configurations,

$$I = I_0 \begin{bmatrix} -1 & 1 & 0 & \cdots & 0 \\ 0 & -1 & 1 & \cdots & 0 \\ \vdots & \ddots & -1 & \ddots & \vdots \\ \vdots & \ddots & \ddots & \ddots & 1 \\ 1 & 0 & 0 & \cdots & -1 \end{bmatrix}, \quad (\text{A.5})$$

where  $I_0$  is the amplitude of the current. For each current configuration, one measures the corresponding voltages at different terminals and gets voltage matrix ( $V$ ).

In the edge state transport model proposed [95] for quantum valley Hall effect, a single ballistic channel connects terminals along the edge. Assuming that all terminals are ordered along the edge so that terminal  $i$  is connected to terminals  $i-1$  and  $i+1$ , then  $Tr_{ij}$  is given by

$$Tr = \begin{bmatrix} 0 & 1 & 0 & \cdots & 1 \\ 1 & 0 & 1 & \cdots & 0 \\ 0 & 1 & \ddots & \ddots & \vdots \\ \vdots & \ddots & \ddots & \ddots & 1 \\ 1 & 0 & \cdots & 1 & 0 \end{bmatrix}. \quad (\text{A.6})$$

For the current configuration given by Equation (A.5), the edge state transport model predicts voltage matrix as

$$V = \frac{I_0}{G_0} \begin{bmatrix} 0 & 0.9 & 0.8 & \cdots & 0.1 \\ 0.1 & 0 & 0.9 & \cdots & 0.2 \\ 0.2 & 0.1 & 0 & \ddots & \vdots \\ \vdots & \ddots & \ddots & \ddots & 0.9 \\ 0.9 & 0.8 & \cdots & 0.1 & 0 \end{bmatrix}. \quad (\text{A.7})$$

Moreover, if the current configuration in Equation (A.5) and voltage configuration in Equation (A.7) are measured, the conductance matrix can be determined from Equation (A.4) and then the transmission probabilities can be calculated from Equation (A.3).



# Appendix B

## Calculation of transition between ferromagnetic and canted antiferromagnetic states

The phase transition between the fully spin-polarized ferromagnetic (F) state and the canted antiferromagnetic (CAF) state is consistent with theory [142, 240] and the previous experiment [244]. The dependence of the sublattice spin tilting angle in the CAF state on the applied magnetic field ( $\vec{B}$ ) and induced magnetic exchange field ( $\vec{M}_{ex}$ ) is estimated.

In the non-interacting limit (when the Zeeman field and spin-orbit interaction are neglected), graphene supports four zero-energy Landau levels and has spin degeneracy as well as valley (K, K') degeneracy. In each valley the wave-functions reside on one of the sublattices (A, B), the valley index is directly related to the degree of freedom of sublattice (K  $\leftrightarrow$  A, K'  $\leftrightarrow$  B). The electron-electron and electron-phonon interactions break the valley symmetry on the lattice scale and the generated valley anisotropy determines the magnetic order of the  $\nu = 0$  state in graphene. In a systematic theoretical study of the possible anisotropy, there are a number of different possible symmetry-broken states [142], but from the experiment in Refs. [242, 244, 245], it indicates that the interactions lead to an AF state (both bulk and edge modes are gapped) with opposite spin-polarization on the two sublattices. Moreover, the applied magnetic field and magnetic proximity effect of YIG lead to the breaking SU(4) symmetry. The Hamiltonian of total magnetic field ( $\vec{M}_T$ , sum of the Zeeman field  $\vec{B}_Z$  and  $\vec{M}_{ex}$  induced by the YIG) is described as

$$\mathcal{H}_{\vec{M}_T} = -\mu_B \vec{M}_T \cdot \vec{\sigma}, \vec{M}_T = \vec{B}_Z + \vec{M}_{ex} = \frac{g}{2} \vec{B} + \vec{M}_{ex}. \quad (\text{B.1})$$

The sublattice spins tend to be parallel to the  $\vec{M}_T$ . All  $\vec{M}_T, \vec{B}$  and  $\vec{M}_{ex}$  are in units of Tesla.  $\mu_B$  is Bohr magneton,  $g$  is gyromagnetic ratio and  $\vec{\sigma}$  are the Pauli matrices.

For the calculation, several assumptions are made.

1.  $g = 2$ .
2.  $\vec{M}_T$  is spatially uniform, and  $\vec{M}_{ex}$  is considered as a spatial average of the magnetic exchange field in graphene induced by the YIG.
3. There is a disordered interface between graphene and YIG, so that the sublattice (valley) symmetry is not broken on average.
4.  $\vec{M}_{ex} = M_{ex} \frac{\vec{B}}{|\vec{B}|}$ , in the absence of spin-orbit coupling effect,  $\vec{M}_{ex}$  is parallel or antiparallel to  $\vec{B}$ , but due to the ferrimagnetic nature of YIG, the magnitude of  $\vec{M}_{ex}$  could depend on the direction of  $\vec{B}$ . However, if the locations of the oppositely polarized magnetic moments do not depend on the direction of  $\vec{B}$ , this dependence is expected to be weak. Therefore the magnitude of the  $\vec{M}_{ex}$  is independent of the direction of  $\vec{B}$ .
5. The magnitude of the  $\vec{M}_{ex}$  does not depend on  $|\vec{B}|$ , when  $\vec{B}$  is sufficiently large so that the magnetization of YIG is saturated. In addition, in-plane and out-of-plane anisotropy of YIG are not important.

The competition between the antiferromagnetic (AF) and F states leads to the CAF state where spins in the two sublattices are tilted along the direction of the  $\vec{M}_T$ , but also they have components perpendicular to  $\vec{M}_T$  which point in opposite directions (preferred by the electron-electron interactions leading to an AF state). The spin directions in the two sublattices can be calculated by minimizing the energy [142, 240]

$$E(\theta) = E_0 + \frac{A_s}{\pi l_B^2} [-\mu_B M_T(B) \cos\theta + u(B_\perp) \cos^2\theta], \quad (\text{B.2})$$

where  $E_0$  is a constant,  $A_s$  is the area of the sample and  $l_B$  is the magnetic length. The anisotropy energy  $u$  depends on the microscopic interactions that break the valley symmetry on the lattice scale, and on the Landau level wave-functions, therefore  $u$  can be controlled with out-of-plane magnetic field ( $B_\perp$ ).

On the basis of the assumptions,  $M_T(B) = |\vec{M}_T|$  depends on the magnitude of the applied magnetic field ( $B = |\vec{B}|$ ). The spin directions relative to the direction of  $\vec{M}_T$  are described by the polar angle ( $\theta$ ), and the azimuthal angles ( $\psi, \psi + \pi$ ) in the two sublattices. The energy  $E(\theta)$  does not depend on the azimuthal angle, so  $\psi$  describes spontaneously broken U(1)-symmetry in the CAF state. The AF state is achieved when  $\vec{M}_T = 0$  and in this case

$\theta = \pi/2$ , indicating that the spins in the two sublattices point in opposite directions. When  $\vec{M}_T = 0$ ,  $\theta$  can be any directions and the AF state is described by the spontaneously broken SU(2)-symmetry. In the F state, the magnitude of  $\vec{M}_T$  is so large that spins are fully polarized along the direction of  $\vec{M}_T$ , then there is no spontaneously broken symmetry in this case (paramagnetic phase). The angle  $\theta$  is calculated by

$$\cos\theta = \begin{cases} 1, & \mu_B M_T > 2u(B_\perp) \\ \mu_B M_T / 2u(B_\perp), & \mu_B M_T < 2u(B_\perp) \end{cases}, \quad (\text{B.3})$$

so that the transition from F to CAF state occurs at  $\mu_B M_c = 2u(B_\perp)$ , where  $M_c$  is the critical transition magnetic field.

The anisotropy energy has not been described as an equation theoretically, therefore it is estimated by utilizing earlier experimental results [244]. In Ref. [244] the edge mode conductance is measured as a function of  $B$  for various values of  $B_\perp$ . In the CAF state, the edge mode is gapped at the Dirac point giving a zero conductance, while F state supports counter-propagating edge modes. If it is ballistic (i.e. the length of the system is shorter than the mean free path), the conductance in a simple two-terminal geometry is given by  $G_2 = 2e^2/h$ . Indeed, experimentally  $G_2(B, B_\perp)$  shows a sharp crossover from 0 to  $2e^2/h$ . Then the critical applied magnetic field  $B_c$  can be estimated by requiring  $G_2(B_c, B_\perp) = e^2/h$ . Magnetic exchange field is zero in Ref. [244], then  $M_c = B_c$ . The phase transition lines in the  $(M_T, B_\perp)$ -plane for samples reported in Ref. [244] are shown in Figure 10.13 and the average result of these two lines is

$$u(B_\perp) = 5\mu_B(B_\perp + 0.5), \quad (\text{B.4})$$

which is a reasonable estimation in the light of Refs. [142, 240]. But the shift of 0.5 T indicates that a nonlinear function is approximately linearized. In Ref. [243], the thermal activation gap increases approximately linearly with  $B_\perp$  of up to 30 T, so the assumption of linear dependence is acceptable.

The spin direction is described by  $\theta$ , which is the polar angle of the sublattice spin relative to the direction of  $\vec{M}_T$ . According to the estimation for  $u(B_\perp)$  and Equation (B.3),  $2\theta = 0.93\pi$  is valid for extremely large  $B_\perp$  or in the absence of magnetic exchange field (Figure B.1). It demonstrates that the spins point in opposite directions, leading to an AF state, which is consistent with the experiment results: the  $\nu = 0$  state in graphene is approximately spin-unpolarized [243] as well as both bulk and edge modes are gapped [243, 260]. In the case of tilted magnetic field, it leads to a CAF state and  $\theta$  decreases with increasing applied

magnetic field when  $B_{\perp}$  is constant. To achieve a transition from F to CAF state, it needs a very large magnetic field ( $> 15$  T) [244].

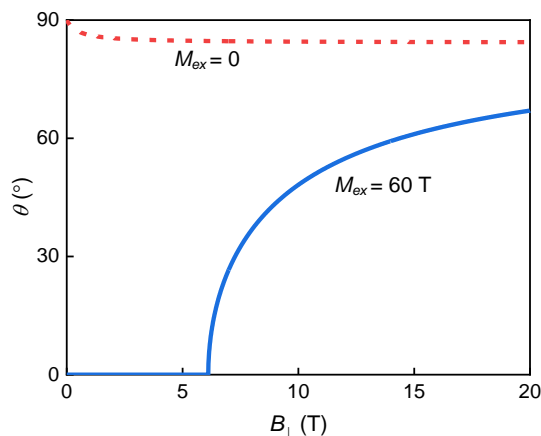


Fig. B.1 The polar angle  $\theta$  as a function of  $B_{\perp}$ . The solid blue (dashed red) line corresponds to  $M_{ex} = 60$  T ( $M_{ex} = 0$ ). In the presence of proximity-induced magnetic exchange field, it is able to control  $\theta$  with  $B_{\perp}$ . But in the absence of magnetic exchange field,  $\theta \approx \pi/2$  approximately corresponding to an AF state.

From nonlocal measurements, the magnetic proximity effect from YIG does not lead to strong orbital effects in graphene, therefore the estimation for the anisotropy energy in Equation (B.4) is valid for hBN/graphene Hall bar on YIG. In Figure 10.11 and Figure 10.12(b), the transition from a F to a CAF state occurs in  $B_{\perp} \approx 6$  T. So  $M_{ex}$  induced by YIG is estimated to be the order of 60 T according to Equation (B.4) and  $M_T \approx 9.9B_{\perp} + 4.9$ . Moreover, in the present of magnetic exchange field,  $\theta$  can be modulated over a wide range starting with relatively low applied magnetic fields ( $> 6$  T) in Figure B.1.